



Review

Towards Polycaprolactone-Based Scaffolds for Alveolar Bone Tissue Engineering: A Biomimetic Approach in a 3D Printing Technique

Krzysztof Stafin ^{1,2}, Paweł Śliwa ¹ and Marek Piątkowski ^{2,*}

¹ Department of Organic Chemistry and Technology, Faculty of Chemical Engineering and Technology, Cracow University of Technology, ul. Warszawska 24, PL 31-155 Kraków, Poland; krzysztof.stafin@jezuici.pl (K.S.); pawel.sliwa@pk.edu.pl (P.Ś.)

² Department of Biotechnology and Physical Chemistry, Faculty of Chemical Engineering and Technology, Cracow University of Technology, ul. Warszawska 24, PL 31-155 Kraków, Poland

* Correspondence: marek.piatkowski@pk.edu.pl

Abstract: The alveolar bone is a unique type of bone, and the goal of bone tissue engineering (BTE) is to develop methods to facilitate its regeneration. Currently, an emerging trend involves the fabrication of polycaprolactone (PCL)-based scaffolds using a three-dimensional (3D) printing technique to enhance an osteoconductive architecture. These scaffolds are further modified with hydroxyapatite (HA), type I collagen (CGI), or chitosan (CS) to impart high osteoinductive potential. In conjunction with cell therapy, these scaffolds may serve as an appealing alternative to bone autografts. This review discusses research gaps in the designing of 3D-printed PCL-based scaffolds from a biomimetic perspective. The article begins with a systematic analysis of biological mineralisation (biomineralisation) and ossification to optimise the scaffold's structural, mechanical, degradation, and surface properties. This scaffold-designing strategy lays the groundwork for developing a research pathway that spans fundamental principles such as molecular dynamics (MD) simulations and fabrication techniques. Ultimately, this paves the way for systematic *in vitro* and *in vivo* studies, leading to potential clinical applications.



Citation: Stafin, K.; Śliwa, P.; Piątkowski, M. Towards Polycaprolactone-Based Scaffolds for Alveolar Bone Tissue Engineering: A Biomimetic Approach in a 3D Printing Technique. *Int. J. Mol. Sci.* **2023**, *24*, 16180. <https://doi.org/10.3390/ijms242216180>

Academic Editors: Dario Pasini, Giuseppe Zanotti and Yuri V. Mironov

Received: 20 October 2023

Revised: 5 November 2023

Accepted: 7 November 2023

Published: 10 November 2023



Copyright: © 2023 by the authors. Licensee MDPI, Basel, Switzerland. This article is an open access article distributed under the terms and conditions of the Creative Commons Attribution (CC BY) license (<https://creativecommons.org/licenses/by/4.0/>).

1. Introduction

1.1. Bone Tissue Engineering (BTE)

The alveolar bone, which secures teeth in the jaw, can undergo resorption following tooth extraction due to the lack of mechanical load [1,2]. The regeneration of alveolar bone, as opposed to skeletal bone, poses unique clinical challenges. While autologous bone grafts are considered the “gold standard” for significant alveolar bone defects [3], they come with drawbacks such as donor site morbidity, deformity, potential infection, and the risk of graft rejection. Consequently, research in material science and tissue engineering is focused on finding suitable materials and their fabrication for the replacement and reconstruction of alveolar bone [4]. BTE focuses on crucial processes involving cell growth and the complex structure of human bone at both microscopic (biomineralisation) and macroscopic (ossification) scales [5].

Numerous methods have been explored to halt the resorption of the alveolar process [6], and research on various strategies for reconstructing alveolar bone defects is rapidly expanding. However, the included studies exhibit a high degree of heterogeneity [7], necessitating the establishment of a unified standard for bone regeneration in the alveolar process [8]. The advancement of medical science, particularly in implantology, relies on the development of a robust research methodology that enables a legitimate

transition from correlational conclusions to causative ones, thereby minimising potential errors before clinical trials. As an interdisciplinary field, BTE combines osteoconductive scaffolds, osteogenic cells, growth factors, and their interrelationships within the natural microenvironment [9]. An integrated methodological approach is proposed to optimise scaffold characteristics, grounded in interdisciplinary research encompassing regenerative medicine, materials, tissue, and dental engineering. Although many phenomena in nature are exceptionally complicated and challenging to replicate, BTE employs a biomimetic approach. This approach provides unique and innovative solutions, offering one strategy to individual fields [10].

1.2. Fused Filament Fabrication (FFF) vs. Other Three-Dimensional (3D) Printing Techniques

Among the promising strategies in this area, the employment of scaffolds fabricated via 3D printing techniques stands out. One such technique is FFF, also known as fused deposition modelling (FDM) [11,12]. Other methods include PolyJet, selective laser sintering (SLS), digital light processing (DLP), stereolithography (SLA), and bioprinting [13]. In comparing FFF with these alternatives, it is valuable to consider various aspects such as cost, materials employed, adaptability of the technique to the structure of the model produced, and the safety associated with the technique's use [14–16].

The PolyJet 3D printing technique [13] utilises photopolymerisation, utilising resin streams for construction. In contrast, SLS [17,18] uses a laser to sinter polymer powders, which facilitates the production of complex geometries that may be more difficult to realise with other methods. DLP [19] cures resins using light and can deliver rapid printing times. SLA [20] is distinguished by its high resolution and ability to fabricate intricate structures precisely. Bioprinting, a specialised subset of 3D printing technology, is engineered to construct biological structures encompassing tissues and organs [21].

While each technique mentioned above possesses distinct advantages, FFF is particularly notable for its cost-effectiveness—it is comparatively economical, enhancing its accessibility [22]. It also supports a wide selection of biocompatible materials, including various biodegradable polymers, which are increasingly relevant in BTE. Furthermore, FFF offers versatility to accommodate specific user needs, allowing for the straightforward customisation of designs without significantly impacting production costs [23]. FFF printers are generally simpler to construct than their counterparts in the 3D printing domain. For instance, the absence of laser radiation or ultraviolet (UV) light in FFF enhances user safety, positioning this technology as a viable option for industrial upscaling within BTE contexts. The inherent simplicity and flexibility of FFF technology make it an exemplary candidate for manufacturing processes aligned with the principles of lean manufacturing and rapid prototyping.

The FFF technology involves the layer-by-layer deposition of fused material to construct a 3D object. This process initiates with the generation of a 3D computer model, which is subsequently 'sliced' into thin cross-sections utilising specialised slicing software. This software delineates the pathways for the print head to follow and sets various printing parameters, including temperatures, speeds, and infill patterns. The print head, or extruder, is heated to a predetermined temperature, facilitating the melting of the filament. This filament, a strand of thermoplastic material typically measuring 1.75 ± 0.15 mm in diameter, is directed into the heated extruder [16]. Within the extruder, the material liquefies and is extruded through a narrow nozzle, generally 0.4 mm in diameter [24], onto the build platform. The extruder traverses the preordained paths, laying the material in successive layers. Upon completion of a layer, the build platform descends (or the extruder ascends, contingent upon the printer design), and the process iterates for the subsequent layer. The newly deposited material cools and solidifies, bonding with the layer beneath it. After the printing concludes, the final object is meticulously detached from the build platform [13].

Currently, two significant bottlenecks are identifiable within the context of BTE concerning FFF. The first involves the processing of the filament to ensure it satisfies the requisite material specifications. The second entails the fine-tuning of printing parameters to achieve a scaffold with properties that are appropriately tailored for BTE.

1.3. Polycaprolactone (PCL) vs. Other Polyesters

A scaffold, which imitates the bone tissue structure, can minimise the risk of rejection by the body and foster bone regeneration [25]. Three-dimensional printing enables the precise and controlled fabrication of personalised spatial structures with complex geometries, adaptable to the anatomical shapes of the alveolar bone [26,27]. One of the most promising materials is PCL [28], mainly due to a suite of properties that set it apart from other synthetic polyesters, such as polyglycolic acid (PGA), polylactic acid (PLA), and poly(lactic-co-glycolic acid) (PLGA) [29].

PGA is a bioresorbable, aliphatic polyester frequently utilised in the medical domain, especially for surgical sutures, owing to its high tensile strength and degradability [30]. PGA scaffolds have been employed in BTE on account of their mechanical attributes. Nevertheless, PGA undergoes rapid degradation and generates acidic by-products, which could affect the local cellular milieu and impede tissue regeneration.

PLA is another aliphatic polyester derived from renewable resources like cornstarch or sugarcane. Besides its widespread use in biodegradable packaging, PLA is employed in the medical field for sutures, drug delivery systems, and tissue engineering scaffolds [31]. However, similar to PGA, the degradation of PLA can lead to acidic by-products, potentially affecting the cellular environment.

PLGA is a copolymer of PLA and PGA that combines the properties of both polymers. Its versatility, evidenced by its tunable degradation rates and mechanical properties, makes it a preferred choice for drug delivery and tissue engineering. PLGA scaffolds can offer intermediate degradation rates between PLA and PGA while maintaining sufficient mechanical strength [32]. However, as with its parent polymers, the degradation by-products can influence the pH of the local environment, which might necessitate careful consideration during scaffold design and application.

In the realm of BTE, the choice between PGA, PLA, and PLGA often hinges on the specific requirements of the application, including the desired degradation rate, mechanical properties, and biological response of the surrounding tissue. PCL offers advantages that address some of the limitations inherent in the polymers mentioned above.

In BTE, one pivotal consideration is the processing properties of PCL, which include a low melting point (approx. 60 °C) [33]. Additionally, PCL's flexibility, attributable to its low glass transition temperature (approx. –60 °C) [34], along with its thermoplasticity, renders it more amenable to being shaped into various forms when compared to the relatively more brittle PLA. Moreover, the balance between stiffness and flexibility in PCL can be modulated [10,28], enhancing its versatility. It readily blends with other polymers or ceramics to form copolymers or composites, thereby facilitating the fabrication of scaffolds with properties that are optimally tailored for bone tissue regeneration.

The second pivotal consideration is scaffold longevity within the body, referring to structural and mechanical integrity. While PGA, PLA, and PLGA present distinct advantages, they typically degrade more rapidly than PCL. The slower degradation rate of PCL [28] is particularly advantageous in BTE, as it ensures the scaffold remains intact, providing consistent mechanical support throughout the development and maturation of bone tissue.

Currently, two limitations of PCL scaffolds are noted. One involves carrying out an appropriate compatibilisation strategy to strengthen the surface to hydrophilic properties. Hydrophilisation is correlated with facilitating cell anchoring and adhering. The second involves the adaptation of the degradation rate of material to the remodelling of bone tissue. However, due to PCL's degradation rate and surface properties, its sole use might not adequately stimulate regenerative processes in bone tissue. Therefore, the introduction of ceramics and natural polymers [35] into the 3D scaffold presents a solution since these materials have high bioactive potential.

1.4. Hydroxyapatite (HA), Type I Collagen (CGI), and Chitosan (CS)

The incorporation of ceramic materials into the PCL matrix permits the regulation of both degradation and resorption rates. Their bioactivity is unmatched, enhancing the

interaction with bone cells. In accordance with the biomimetic approach, HA is identified as a promising material owing to its structural congruence with bone tissue. Other materials, such as β -tricalcium phosphate (β -TCP) [36], bioactive glass, and silica-based ceramics, also promote the formation of bone tissue; however, their bioactivity is somewhat inferior compared to HA. Furthermore, their biodegradation rates and biocompatibility are less optimally adaptable to specific requirements than those of HA.

In the biomimetic approach to BTE, CGI and CS are deemed appropriate materials. CGI, in conjunction with HA—the quintessential organic and inorganic components of bone tissue—plays a pivotal role in biomimetic mineralisation [37]. Together, they replicate the natural microstructural matrix, providing an optimal environment for tissue regeneration. CS, a natural polysaccharide within the glycosaminoglycans (GAGs) family, also demonstrates significant bioactive potential [38–40]. Renowned for its biocompatibility, capacity to promote cell growth, and ability to inhibit bacterial proliferation, CS facilitates the biomimetic mineralisation process, which involves the synthesis of mineral substances similar to those in natural bone tissue [41]. Compared to other natural polymers, CS has distinct advantages:

- It exhibits superior mechanical properties and a more streamlined purification process than silk fibroin [42].
- Its production is less costly and arises from more diverse sources than hyaluronic acid [43].
- CS surpasses bacterial cellulose in biodegradation within physiological environments and demonstrates enhanced osseointegration [44].

Utilising a 3D scaffold comprising PCL, HA, CGI, and CS can establish a biomimetic environment that triggers regenerative processes at the alveolar bone defect site [45,46]. The scaffold's structure allows the adhesion of bone cells, providing mechanical support, while CGI and CS act as active ingredients stimulating osteoblasts' anchoring, proliferation, and differentiation [47,48]. Through the synergy of these components, the PCL-based 3D scaffold can accelerate the regeneration process, leading to bone mineralisation at the defect site. This approach paves the way for practical BTE by establishing a biomimetic environment conducive to restoring the structure and function of bone tissue in a manner harmonious with the body's biology, thereby leading to improved therapeutic results.

This review outlines the main challenges in designing osteoconductive scaffolds with osteoinductive potential for alveolar bone engineering. Emphasis is placed on understanding processes such as biomimetic mineralisation and ossification. Through a biomimetic approach, we examine a range of properties that these scaffolds should possess (Figure 1). Given that reviewing processing conditions and structural, mechanical, degradation, and surface properties is complex and subject to debate, we focus on discussing and identifying research gaps.

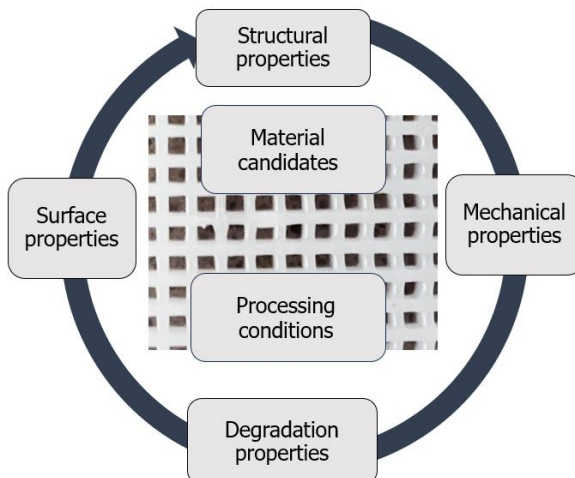


Figure 1. Scheme incorporating the most critical properties and parameters in the fabrication of 3D-printed PCL-based scaffolds.

2. Alveolar Bone

The alveolar bone is unique due to its embryonic cellular origin, specific ossification process, and connection to teeth via periodontal tissues. This bone plays a pivotal role in safely anchoring teeth, enabling them to withstand the forces generated during chewing and biting (mechanical function) [6,8]. Additionally, the alveolar bone contributes to maintaining the shape of the mouth by connecting the tooth root with surrounding bone tissue (stabilisation function) [49]. This linkage secures the tooth's position and reduces the risk of tooth loss due to periodontal disease or other oral health issues [50].

Moreover, the alveolar bone plays a significant role in tooth development. As the teeth evolve, the bone grows and reshapes to accommodate the emerging tooth. The alveolar bone also aids in maintaining teeth alignment posteruption, regulating the movement and positioning of periodontal ligaments [51].

Understanding the unique function and structure of the alveolar bone can significantly contribute to maintaining oral homeostasis, which is a balance between the resorption and formation of bone [6]. Bone tissue homeostasis is strongly related to the balanced activities of osteoblasts and osteoclasts, which are responsible for bone formation and resorption, respectively. Moreover, osteocytes play a pivotal role in regulating both of these processes [8,52]. These cells interact through mechano-biochemical signals with each other to regulate the processes of bone formation and resorption, which is crucial for bone homeostasis (Figure 2) [6,53].

Thus, the amount of bone tissue resorbed by osteoclasts is balanced by the amount of new bone formed by osteoblasts, ensuring that the net bone mass remains constant (coupling system). However, this equilibrium is disrupted following tooth extraction or during the early healing phase of severe periodontitis, resulting in excessive osteoclastic bone resorption—a primary characteristic of jawbone disease. The ultimate consequence of the alveolar bone's physiological remodelling is localised loss [6,53].

Therefore, all processes, including the ossification of the alveolar bone, are integral to oral health and development. This diverse jaw structure's morphological and mechanical features necessitate innovative therapeutic approaches [54].

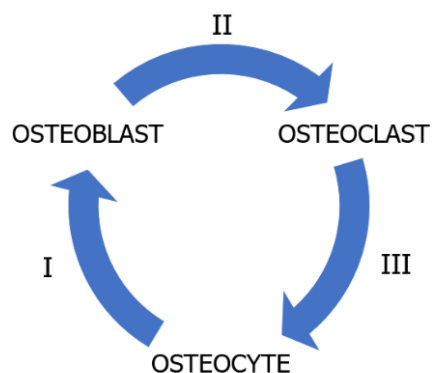


Figure 2. Scheme of osteocyte–osteoblast–osteoclast interactions enclosed in coupling system. (I) Osteocyte–osteoblast interactions: osteocytes possess the ability to detect mechanical loads on bone. When a bone is loaded, osteocytes convert this load into biochemical signals. Subsequently, osteocytes can release factors, such as prostaglandins and nitric oxide (NO), which modulate osteoblast activity. Through this mechanism, osteocytes promote the activation of osteoblasts to form new bone in response to loading. (II) Osteoblast–osteoclast interactions: osteoblasts produce and release factors such as RANKL (receptor activator of nuclear factor κ -B ligand) and M-CSF (macrophage colony-stimulating factor). RANKL binds to the RANK receptor on the surface of osteoclast precursors, leading to their differentiation into fully active osteoclasts. Additionally, osteoblasts produce osteoprotegerin (OPG), which serves as a 'trap' for RANKL, inhibiting osteoclast activation. The balance between RANKL and OPG in the bone microenvironment determines whether bone will be resorbed or formed. (III) Osteocyte–osteoclast interactions: osteocytes can also release RANKL, influencing the activation of osteoclasts. Furthermore, osteocytes can secrete factors that inhibit osteoclast activity in response to mechanical loading [6,55–57].

2.1. Ossification and Biomimetic Ossification

Ossification is the overarching process of bone formation. It predominantly results in the growth and repair of hard tissue at the macroscopic scale. Mimicking natural biological processes by inserting a PCL-based scaffold into an alveolar bone defect poses a significant challenge. The scaffold's architecture is designed to provide stability and mechanical strength commensurate with bone tissue.

Mechanisms of Ossification

Ossification primarily occurs through endochondral and intramembranous mechanisms [21,58]. Figure 3 offers a comparative overview of these processes. Alveolar bone ossification proceeds via the intramembranous mechanism [6,59]. From an engineering perspective, these two mechanisms exhibit several key distinctions.

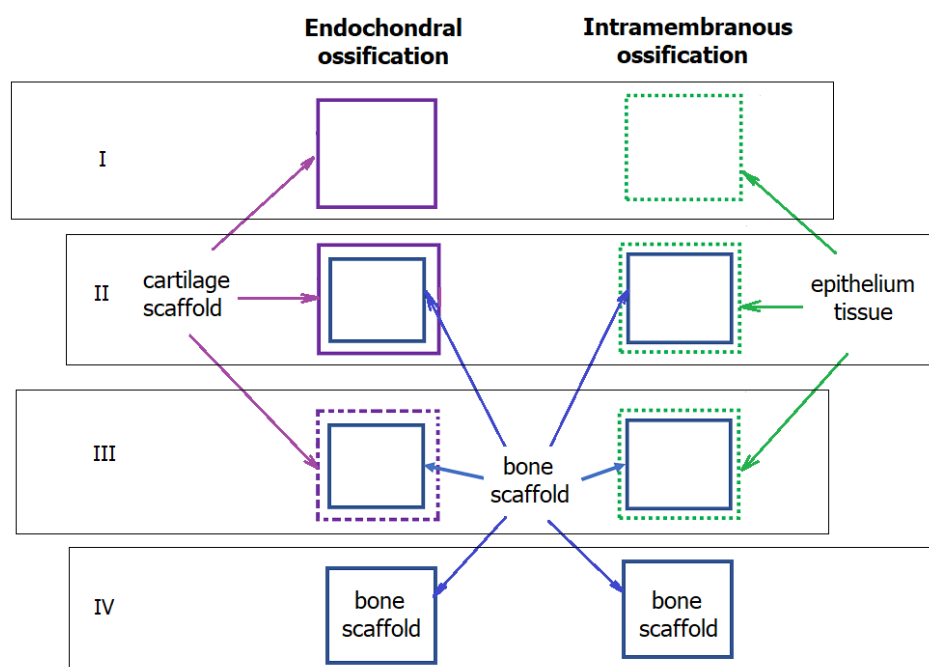


Figure 3. Diagram of the stages of bone ossifications. Endochondral ossification: (I) the formation of model cartilage (scaffold) rich in chondrocytes; osteoblasts migrate inside the cartilage scaffold; (II) inside the cartilage scaffold, osteoblasts produce primary bone in the form of bone trabeculae; (III) simultaneous loss of model cartilage and growth of bone tissue (chondrocytes undergo apoptosis and the cartilage matrix is degraded). Intramembranous ossification: (I) the formation of a tissue membrane rich in fibroblasts; fibroblasts differentiate into osteoblasts; (II) based on membrane tissue, osteoblasts produce primary bone in the form of bone trabeculae, which are connected to form a network; (III) a bone tissue grows in the space. For both of them: (IV) a bone is constantly transformed and adapted to the body's needs; osteoblasts, osteoclasts, and osteocytes control remodelling.

Firstly, endochondral ossification occurs within a pre-existing cartilaginous scaffold, which provides inherent mechanical stability during ossification and biodegrades as the bone tissue gains enough mechanical strength [60]. In contrast, intramembranous ossification directly occurs within connective tissue, lacking the mechanical robustness provided by a cartilaginous scaffold. This aspect makes the developing intramembranous ossification more vulnerable to external forces, potentially leading to deformities in the bone architecture [61].

Secondly, the origins of osteoblasts, the cells responsible for bone formation, differ between the two processes. In endochondral ossification, osteoblasts initially form outside the cartilaginous scaffold, typically differentiating in the bone marrow [62]. These cells then migrate into the scaffold, where they proliferate and differentiate. Conversely,

osteoblasts directly originate within the connective tissue in intramembranous ossification, differentiating from mesenchymal cells resembling primitive fibroblast precursors.

Consequently, the two ossification processes significantly differ in their mechanisms, particularly regarding their mechanical implications and osteoblast formation [63]. It would be intriguing to hypothesise whether introducing a scaffold could alter the biological behaviour of the healing and ossification process.

Understanding the ossification mechanism of the alveolar bone aligns with the biomimetic approach and aids in designing bone replacement material. The scaffold at the defect site should provide sufficient space for osteoblast development without creating a spatial barrier. One method to minimise this spatial barrier, thereby promoting the differentiation of osteoblasts (bone ossification) and fibroblasts (bone healing), is to enable the scaffold to transmit mechanical forces and convert them into a biochemical signal (mechanotransduction) [64].

2.2. Biomineratisation and Biomimetic Mineralisation

Bone mineralisation, a specific stage of ossification at the microscopic scale, involves the precipitation of calcium (Ca^{2+}) and primarily monohydrogen phosphate (HPO_4^{2-} , P_i) ions [65]. The typical biogenic mineral is hydroxyapatite ($\text{Ca}_{10}(\text{PO}_4)_6(\text{OH})_2$, HA), an inorganic component integral to bones and teeth [66]. Biomimetic mineralisation is a strategy that seeks to emulate natural mineralisation processes to create hydroxyapatite with a crystallographic structure that resembles bone apatite [67]. For instance, Cai et al. utilised X-ray spectroscopy to analyse the resulting materials. They found that the calcium-to-phosphorus (Ca/P) ratio of the synthesised hydroxyapatite (1.65) was similar to that of natural bone tissue (1.67) [68]. While the precise mechanism of biomineratisation remains controversial and not entirely understood due to limitations and gaps in comprehending this process *in vivo* [69], the control of hydroxyapatite (HA) crystallisation by an organic matrix, such as type I collagen (CGI), is common to all apatite-containing hard tissues [5,70].

2.2.1. Stages of Biomineratisation

From a crystallisation standpoint, biomineratisation can be divided into two stages: the nucleation of calcium phosphate ($\text{Ca}_3(\text{PO}_4)_2$, CaP_i) (i) and the growth of its crystals in the form of apatite (ii) (Figure 4).

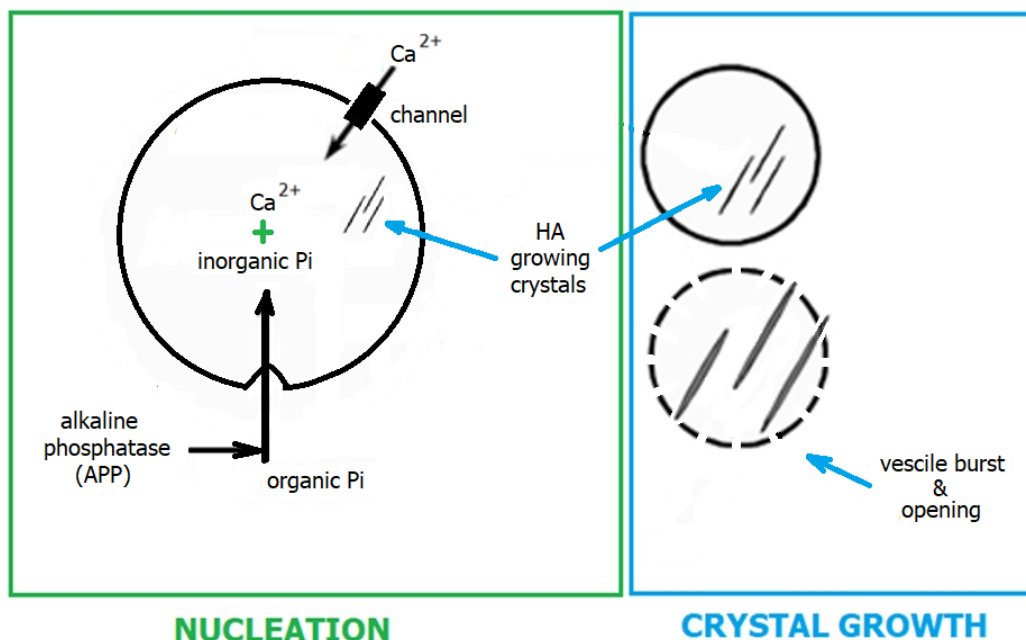


Figure 4. The formation of HA crystals in and out of the matrix vesicles.

HA nucleation occurs in matrix vesicles produced by osteoblasts and released into the extracellular matrix (ECM) [71]. Ca^{2+} is transported inside the vesicle by the Ca^{2+} pump, and P_i is converted from organic to inorganic by alkaline phosphatase. The matrix vesicle contains CGI, the matrix for CaP_i precipitation. Thus, this process occurs at the interface of the inorganic–organic phase [72,73]. From a biochemical perspective, the precipitation behaviour of CaP_i can be influenced by critical parameters, such as pH and the concentration of individual Ca^{2+} and P_i . Three variants are identified within the matrix vesicles, where a unique microenvironment prevails (Figure 5). In the first variant (pH equal to or lower than 6.2), biominerisation does not occur, even if an appropriate concentration of Ca^{2+} and P_i ions is present in the matrix vesicles. Equilibrium is then established between the concentrations of monohydrogen phosphate (HPO_4^{2-} , P_i) and dihydrogen phosphate (H_2PO_4^-) ions, where their concentration remains constant. In addition, HPO_4^{2-} is condensed into pyrophosphate ($\text{HP}_2\text{O}_7^{4-}$, PP_i) ions. The second variant occurs in a neutral or slightly alkaline environment (pH in the range of 7.0 to 7.2). Here, the precipitation process of Ca^{2+} and HPO_4^{2-} occurs.

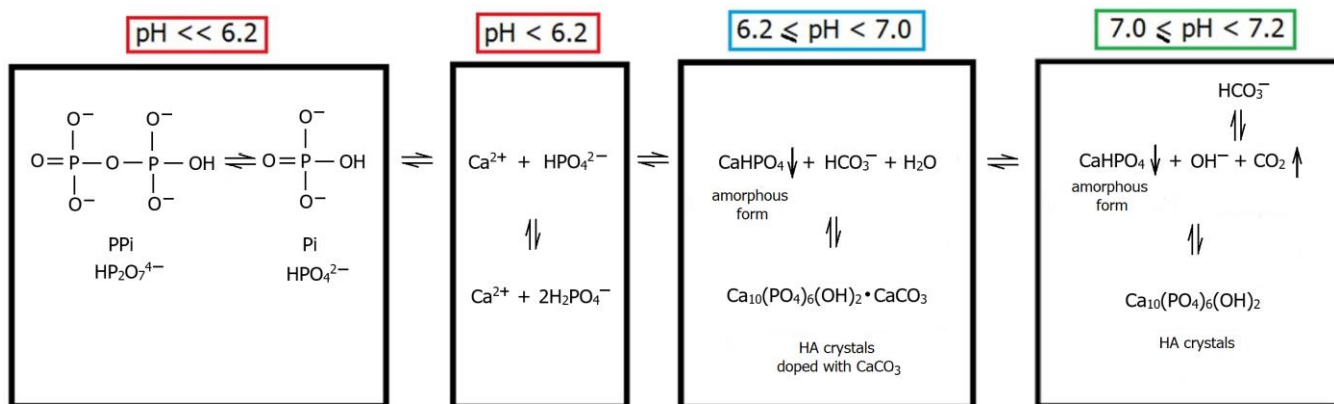


Figure 5. Scheme of the behaviour of Ca and P_i depending on pH in the matrix vesicle.

Furthermore, the bicarbonate (HCO_3^-) ions are enzymatically degraded to carbon dioxide (CO_2) and the hydroxyl anion (OH^-). It can be hypothesised that CO_2 contributes to the rupture of the matrix vesicle, and the OH^- is incorporated into the apatite structure, forming HA. The third variant (pH in the range of 6.2 to 7), which is most characteristic of bone, involves HCO_3^- not being fully decomposed and incorporated into the apatite structure [74]. Consequently, hydroxyapatite in bones, typically doped with bicarbonate (so-called bone apatite), is characterised by easier solubility, facilitating dynamic bone remodelling [75,76].

Crystal growth primarily occurs after the matrix vesicle opens. The standard size of the basal unit of bone apatite is 30–50 nm (length), 15–30 nm (width), and 2–10 nm (thickness) [77], exhibiting a rodlike or platelike microstructure, and is embedded in collagen fibres [78]. Bone apatite constitutes approximately 50 vol.% of the mature bone. The specific microstructural organisation of bone is age-dependent and varies among different bones and within different locations of the same bone [79]. HA crystals are deposited on collagen fibrils in intrafibrillar and extrafibrillar spaces [37,74]. HA crystal growth is regulated by noncollagenous proteins such as osteocalcin and SIBLING [80].

In addition, glycosaminoglycans (GAGs) also appear to be indirectly involved in HA crystal growth [81,82]. Many studies on bone mineralisation focus on the role of CGI and cells such as osteoblasts and osteoclasts, which may draw attention away from the functions of GAGs. Properties of GAGs, such as their ability to bind and hold water protection against mechanical stresses or interactions with proteins and minerals [83,84], may play pivotal roles in HA crystal growth. Therefore, further research is necessary to understand these processes better.

GAGs, soft and hard tissue ECM components, are highly anionic straight-chain polysaccharides composed of repeating disaccharide units. Each unit consists of amino sugar and uronic acid. GAGs in bones play a vital role in transmitting mechanical forces. Their structure enables them to absorb impact energy, reduce the risk of injury, and contribute to bone toughness by retaining bound water in a bone mineral matrix [85]. The GAGs align specifically with the CGI, increasing the ordering of the CGI fibrils in the direction of mechanical force transmission [83,84]. On the other hand, too high accumulation of GAGs in cartilage and bone tissues leads to progressive cartilage damage, reducing bone growth [86,87].

The primary component of the GAGs fraction in alveolar bone is chondroitin sulphate (ChS) [88,89]. ChS was first extracted from cartilage tissue. However, it is essential to note that interactions between ChS and type II collagen (CGII)—primarily found in cartilaginous tissue—may differ from interactions between ChS and CGI, which predominate in alveolar bone tissue. Although present in lesser amounts in bone than in cartilaginous tissue, ChS indirectly contributes to biominerallisation. Due to its chemical structure, ChS attracts Ca^{2+} and P_i ions deposited on collagen fibres to form the bone mineral unit [90,91]. ChS also provides chemical protection; its presence can prevent CGI from acidic denaturation even at low pH levels during inflammation [92]. Furthermore, ChS plays a pivotal role in controlling the shape, size, and number of apatite crystals, promoting the intrafibrillar growth of HA crystals [90,91]. It also enhances bone elasticity, although it may be presumed that this occurs in a manner distinct from that in cartilaginous tissue areas.

2.2.2. Theories of Biominerallisation Mechanism

Given the complexity of the nucleation and growth phenomena of HA crystals, the biominerallisation mechanism still needs to be fully understood. Therefore, two theories are proposed: classical and nonclassical [74].

The classical theory of bone mineralisation suggests that the critical determinant is the occurrence of the substrate, specifically the collagen matrix [74]. Type I collagen (CGI), the most abundant protein in mammals, constitutes 25% (by dry weight) of all proteins. It is one of ten types of collagen, making up about 90 wt.% of all collagens [93]. This protein is expressed in the cells of the skin, ligaments, tendons (fibroblasts), cartilage (odontoblasts), and bone (osteoblasts), serving as the primary structural element in these tissues [94,95].

The nonclassical theory of bone mineralisation posits that this process heavily relies on the activity of osteoblasts and osteoclasts. According to this, the collagen matrix is not the only determining factor for biominerallisation; noncollagen proteins such as bone sialoprotein (BSP), osteocalcin, and SIBLING proteins [53,70,96,97], as well as polysaccharide compounds like glycosaminoglycans (GAGs) [83], are also significant contributors. This theory argues that noncollagen proteins are pivotal in controlling the shape and size of apatite crystals, leading to proper bone mineralisation. Furthermore, the nonclassical theory suggests that mechanical stresses can influence biominerallisation. These stresses potentially modulate the biochemical signal, adding another layer of complexity to our understanding of biominerallisation [98].

Both theoretical viewpoints and the impact of mechanical stress should be considered in hard tissue engineering research designs to provide a comprehensive view of bone mineralisation.

2.3. Requirements for Bone Tissue Engineering (BTE)

Currently, aliphatic polyester-based scaffolds are gaining popularity over human-origin living bone tissue surgically transplanted (autograft) [99]. Research in this field focuses on composite scaffolds based on PCL, with HA and natural polymers (such as CGI or CS) [100–103]. In contrast to autografts (see Figure 6), PCL-based scaffolds, supplemented with HA, CGI, and CS, provide more control over the structure, mechanical properties, and composition. For a scaffold to effectively foster the growth of new bone tissue in a defect, it must exhibit properties conducive to bone regeneration. These re-

generative properties can be categorised into the following processes: osteoconduction, osteoinduction, osseointegration, and osteogenesis [104–107].

Osteoconduction is the 3D process of ingrowth of capillaries, perivascular tissue, and osteoprogenitor cells from the bone bed into a structure of the porous implant. The main factor ensuring osteoconductivity is a complex interplay between the microarchitecture and surface of the scaffold and its material type. The microarchitecture (porosity, pore size, and shape) is said to ultimately determine the efficiency of new bone formation and its vascularisation [108]. Osteoconduction is the main driving force of bone regeneration in the case of a scaffold [109].

Osseointegration is defined as a surface (2D) process in which the implant comes into direct contact with the bone and maintains it during functional loading. Its biological measure can be expressed as the percentage of bone in direct contact with the implant or the force needed to remove the implant from the bone. The main factor ensuring successful osseointegration is the determination of the appropriate macroarchitecture of an implant (i.e., its shape and hydrophilicity) [109–112].

Osteoinduction is a characteristic process inside the scaffold that, via the presence of appropriate biologically active substances (vital proteins and growth factors), encourages the differentiation of mesenchymal stem cells (MSCs) and other osteoprogenitor cells into osteoblasts [83,84]. Moreover, according to Weber, osteoinductive factors are independent of osteoconduction that has occurred [109].

Osteogenesis is the process by which osteoblasts in the scaffold produce minerals that calcify the collagen matrix (biomineralisation), creating a substrate for new bone formation (ossification) [113–115].

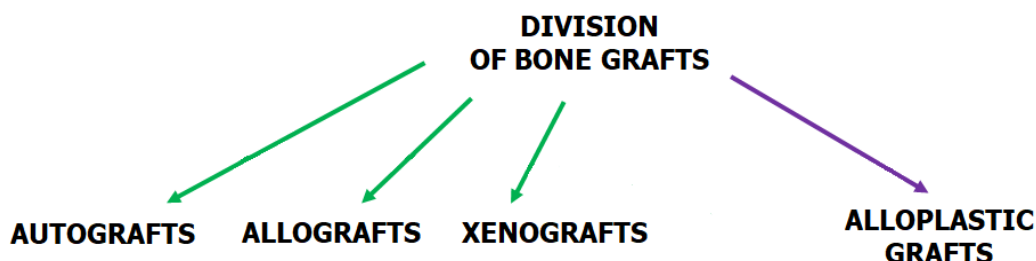


Figure 6. Division of bone grafts according to their origin. An autograft is a tissue transferred from the same individual. It has been considered to be the standard of bone graft replacements. An allograft is a tissue transplanted within the same species, e.g., from one person to another. A xenograft is a tissue or organ that is derived from a species that is different from the recipient of the specimen. An alloplastic graft consists of synthetic biopolymers. It is synthetically derived or made from natural materials [116].

Bone regeneration is a highly complex process. Oryan et al. assessed the bone repair effect of the (polylactide, PLA)/PCL/HA scaffold without loading it with differentiated bone cells. An *in vivo* analysis of this scaffold in rats confirmed that the bone tissue's self-healing potential was not sustained even 80 days postinjury. However, adhesion of native HA particles was observed in several scaffold areas. This result suggests that HA generates a conducive environment for cells to attach and proliferate within the fabricated scaffold [117]. Therefore, a cell-free scaffold can support mild repair effects.

Bone regeneration generally depends on the concurrent occurrence of the healing and ossification processes. Yu et al. studied *in vivo* the impact of a PCL/HA/CS scaffold loaded with osteogenic markers (e.g., BMP-2) and angiogenic markers (e.g., VEGF, PDGF) on bone regeneration in a rabbit model to achieve a pronounced therapeutic effect. These markers stimulate the differentiation of bone and epithelial tissue, respectively. It appears that both BMP-2 and VEGF mutually enhance the fracture regeneration process [45], which results in a notable improvement in new bone formation. However, regenerating the alveolar bone after tooth extraction remains a significant challenge [118]. Generally, healing and ossification are more cooperative and sequential stages.

In the case of alveolar bone, the inflammatory reaction that starts healing induces significant bone resorption. Although this phenomenon is temporary, it substantially reduces bone volume. Naik et al. conducted clinical trials utilising PCL-based scaffolds inspired by results previously documented in animal studies and performed augmentation of intraoral defects in a selected group of patients [119]. From the drawn conclusions, it can be inferred that the anatomical features of the sinus cavity play a crucial role in the success of local alveolar bone augmentation. New bone growth is observed when the graft material contacts the Schneiderian membranes, the floor, and the walls of the sinus without penetrating the delicate oral mucosa. Moreover, developing a method where the scaffold permits the migration of osteoblasts into the scaffold's inside has a significant value.

In bone tissue regeneration, numerous biological studies are conducted; for instance, the adhesion, proliferation, and differentiation of osteoblasts in the scaffold are examined. Ultimately, the repair effect of the alveolar bone is determined based on its volumetric growth [120]. Achieving an osteoconductive scaffold with osteoinductive potential involves developing scaffolds with desirable structural, mechanical, degradation, and surface properties to at least induce a mild repair effect on bone tissue. A mild repair effect on bone tissue suggests the potential for the inoculation of cells, markers, and growth factors into the scaffold's internal environment. Only such a scaffold, combined with cell therapy, results in satisfactory regeneration of bone tissue [27].

Furthermore, combining an osteoinductive strategy with a custom osteoconductive scaffold, identifying the limiting steps of biominerallisation and ossification mechanisms, and comparing the repair effect of the scaffold with a control group (autograft) will provide more reliable results. Despite many constraints, PCL-based composite scaffolds extruded from filament exhibit significant potential for BTE applications [121]. As the electrospun PCL/HA scaffold has been demonstrated to be a robust material for repairing bone defects [122,123] and, when loaded with various drugs and metal particles [124], significantly promoting osteogenic activity, there is a reasonable expectation that the 3D printing method could yield equivalent or even more substantial results [125].

3. Material Candidates for Scaffolds

3.1. Polycaprolactone (PCL)

PCL is a linear polyester (Figure 7) characterised by a slow degradation rate, which makes it suitable for potential load-bearing applications [126–128]. It has gained approval from the Food and Drug Administration (FDA), enabling new solutions for surgical implant material and drug delivery devices for tissue engineering and regenerative medicine applications [129,130]. Consequently, its usage in fabricating 3D scaffolds for bone engineering has increased. The advantages of PCL include high flexibility and elongation [131], satisfactory biocompatibility, lower acidity of breakdown products compared to other polyesters, and significant load-carrying potential [132].

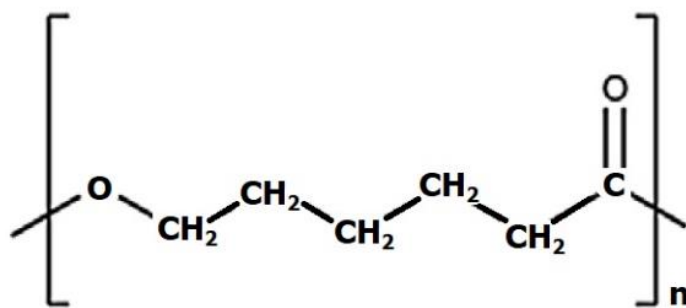


Figure 7. Chemical formula of PCL.

However, the limitations of pure PCL are worth noting. Due to its poor hydrophilicity, it lacks the osteogenic potential to induce bone regeneration [133]. Therefore, researchers have been combining PCL with various polymers [134–136] and inorganic substances [137–139] to enhance the biomechanical properties of the scaffolds. The incorporation of bioactive inorganic particles, such as HA [100,103,140–142] and CS [143–145], into the PCL matrix offers a promising solution to overcome these drawbacks.

3.2. Hydroxyapatite (HA)

The crystalline phases of CaP_i exhibit good biocompatibility, which makes them promising materials for repairing hard tissue defects [146]. The most common biomaterial CaP_i crystal phase is hydroxyapatite ((HA); Ca₁₀(PO₄)₆(OH)₂) (Figure 8), which is thermodynamically stable in body fluids [147]. HA has drawn researchers' interest in recent years due to its porous structure, modification potential, biocompatibility, and bioactivity, the latter referring to its high osteogenic potential [139]. This characteristic greatly accelerates bone and tooth regeneration. Moreover, studies indicate that HA nanoparticles can effectively suppress the growth of various cancer cells [148–150]. Over the past decade, HA has gained widespread recognition as a biomedical material used in bone repair, metal implant coating, dental restoration, and drug delivery systems [151].

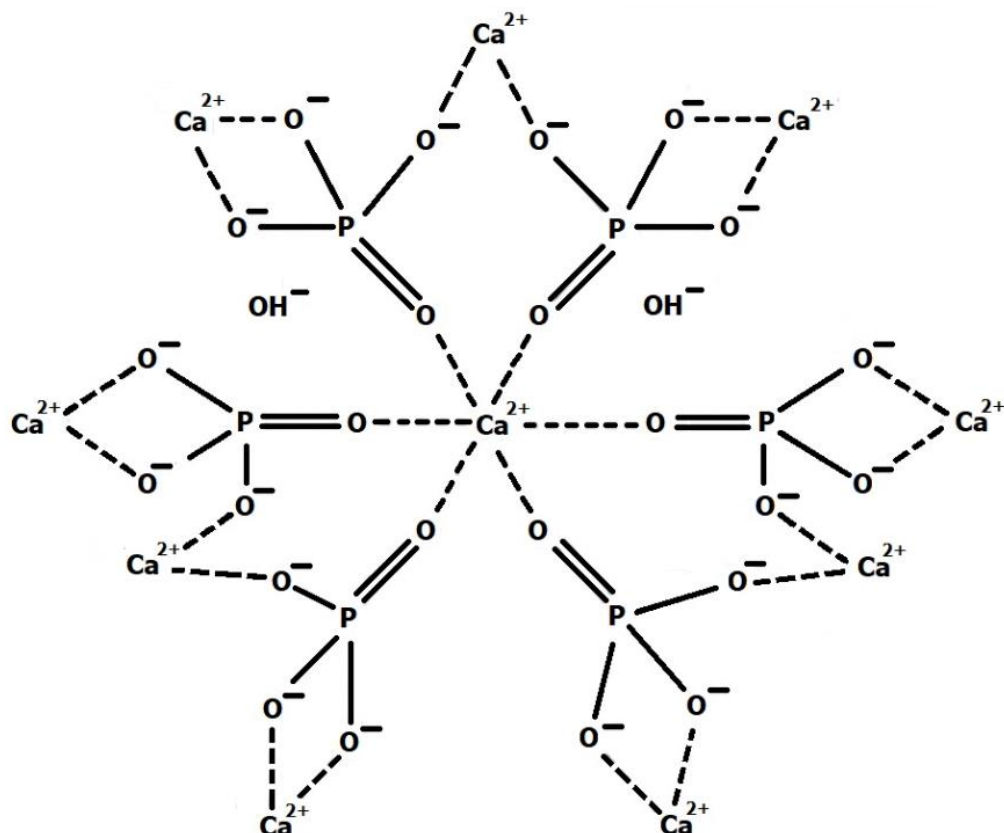


Figure 8. Chemical formula of HA.

The source of HA affects its chemical composition, structure, and properties [152]. Numerous methods have been developed to prepare HA. These techniques can be categorised into two groups: (i) biobased extraction methods, and (ii) synthetic methods, which include the hydrothermal method, chemical precipitation method, hydrolysis method, solid-state synthesis method, and sol-gel method [153].

Synthetic HA is the most commonly used material. It is easily obtained from an aqueous solution via a simple coprecipitation method [154]. HA can be produced in various crystallographic forms by reaction between calcium and phosphate salts. A significant feature of HA is its ability to accommodate suitable ionic substitutions, thereby influencing its composition, structure, and solubility. Consequently, ions of similar or smaller size than Ca^{2+} (such as Fe^{2+} , Cu^{2+} , and Mg^{2+}) can be incorporated into the HA crystal lattice with minimal impact on lattice parameters [155].

It was also demonstrated that lanthanides such as Yb and Ho, which have ionic radii much larger than Ca^{2+} , can enter the HA crystal lattice without significantly affecting its internal crystal structure [156]. Additionally, the incorporation of Si ions from metasilicate—which is generally absorbed and abundantly distributed in connective tissue—is significantly involved in bone regeneration [157,158]. Biologically synthesised HA created in a physiological environment typically contains various trace elements, including F, Si, Cu, Mg, Sr, Ag, Zn, and Fe, which aid bone regeneration [159,160].

The introduction of necessary elements into the HA structure to enhance its biological activity is appealing due to its compact process and simple composition. However, the conclusions derived from research on HA biominerallisation require further clarification [161]. From an engineering standpoint, the main challenge is to obtain HA with an admixture of a specific element that facilitates a long-term and slow release of trace elements required by the body [162].

Despite its many advantages, introduced HA remains a foreign substance to bone tissue. This is crucial because there are differences in the crystal structure, size, and stability between synthetic HA and *in vivo* mineralised HA [163]. On the other hand, synthetic HA with the same Ca/P ratio as bone minerals readily converts to bone apatite *in vivo*. The most limiting feature of HA from an engineering perspective is its high brittleness. To increase the mechanical strength and structure of the final scaffold, many researchers have introduced HA particles into the PCL matrix [117,164]. Ongoing research aims to achieve an evenly distributed high HA content, enabling the body to accept the bone graft material.

3.3. Natural Polymers

3.3.1. Type I Collagen (CGI)

One of the challenges in hard tissue engineering is the development of alternative sources of CGI as an initial-stage matrix of biomimetic mineralisation. Currently, CGI is obtained from the skin tissue of cows [165], rat tails [166], and fish [167]. Research is being conducted on using plant collagen in BTE. However, it still requires research and development of technology, in addition to plant collagen and the so-called recombinant collagen. Research is also being carried out to obtain synthetic collagen. This collagen is more accessible to manufacture and can be tailor-made for tissue engineering, but unfortunately, it is not as biocompatible as natural collagen. All of the above sources of CGI have their advantages and limitations. They require further research to provide a safe and effective replacement for natural collagen in bones [168].

CGI, the primary organic component of bone ECM, has a complex structure comprising three hierarchical levels. The base level consists of a triplet of amino acids, primarily proline (Pro), hydroxyproline (Hyp), and glycine (Gly) [169]. These triplets of amino acids are arranged repeatedly to form a secondary structure [170]. The tertiary level is a triple helix formed from three interconnected chains (Figure 9). At the supramolecular level, collagen fibrils form fibres [171], which undergo self-assembly into a hydrogel network under appropriate physicochemical conditions [172].

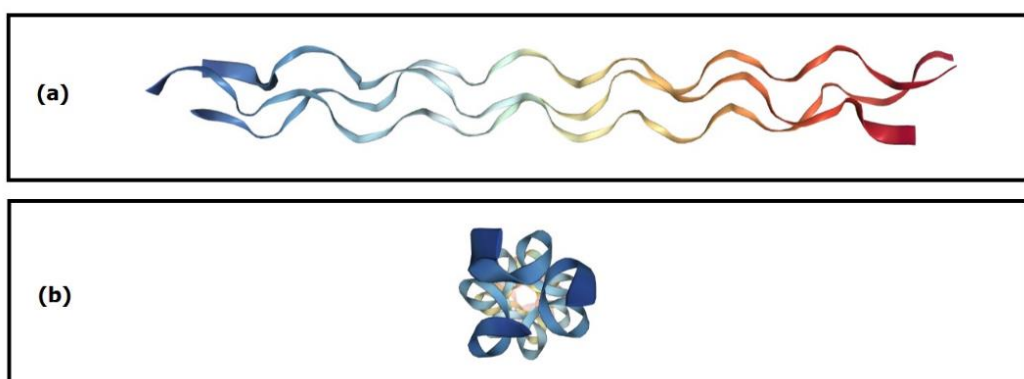


Figure 9. Tertiary structure of CGI. Longitudinal (a) and transverse (b) view.

A systematic analysis of CGI's primary amino acid sequence reveals a biomacromolecule enriched with charge. Recently, efforts to clarify the role of CGI molecules in mineral nucleation including performing molecular dynamics (MD) simulations [173,174]. Although most MD simulations or simplified in vitro studies neglect complex *in vivo* biological environments, the significant benefits and relevance of these discoveries and proposed theories are evident. This approach offers the advantage of preventing errors early in research.

Understanding CGI-HA interactions is crucial for comprehending biominerallisation and the formation of bone and tooth tissues [174]. The behaviour of Ca^{2+} and P_i ions is influenced not only by the pH and concentration in the environment but also by the type of protein involved, especially its conformation, which dictates the distribution of positive and negative charges on its surface [175].

Wang et al. utilised MD simulation to investigate the initial stage of biominerallisation, characterised by the aggregation and nucleation of Ca^{2+} and P_i to form CaP_i . The results demonstrated that P_i ions play a more critical role in biominerallisation than Ca ions. Moreover, the helical conformation of proteins enhances the likelihood of precipitation of the crystalline phase of HA. It is suggested that the intermittent distribution of acidic and basic residues on protein surfaces promotes the formation of large concentrations of Ca^{2+} and P_i , potentially leading to homogeneous nucleation [175]. The cumulative charge on the protein surface largely dictates the binding affinity of Ca and P_i ions [176].

Xue et al. proposed a mechanism for forming CaP_i minerals on the surface of CGI, which varies depending on the composition of phosphate and carbonate ions. The presence of HPO_4^{2-} in the solution is critical for regulating apatite nucleation, while the presence of H_2PO_4^- inhibits the crystal nucleation process. The inclusion of CO_3^{2-} in the solution can promote the formation of CaP_i clusters. The regulation of apatite clusters can be achieved by altering the ratio of anion concentrations, such as $\text{PO}_4^{3-}/\text{HPO}_4^{2-}$ and $\text{PO}_4^{3-}/\text{CO}_3^{2-}$. It is hypothesised that mineralisation and demineralisation are strongly tied to the thermal stability of bonds and the kinetics of ion association [177].

As a substitute for CGI, Zhou et al. designed and synthesised a bioactive peptide as a promising agent for preventing tooth decay. It can inhibit demineralisation in an acidic environment and induce self-healing remineralisation *in situ* [178]. In the outermost layer of the bioactive peptide, positively charged amino acid residues bind to P_i , while negative charges attract Ca^{2+} . Through this strong interaction, HA nucleation sites are formed [179]. Compared to CGI, this protein shows a statistically higher affinity to the tooth surface, stronger counteracting demineralisation, and the promotion of remineralisation of the tooth [180]. The bioactive peptide also has an antibacterial effect. It inhibits the adhesion of *Streptococcus mutans* (cariogenic bacteria) [179].

An integrated experimental and computational approach can provide high-resolution insight into the biominerallisation mechanism. MD simulations combined with empirical studies (e.g., NMR spectroscopy) allow for determining how the peptide interacts with the HA surface [181].

Another way to improve the regulation of HA nucleation processes is through enriched proteins in glutamate and aspartate residues and citrate ions. However, this mechanism still needs to be sufficiently elucidated. Zeng et al. used MD simulations to investigate how citrate ions regulate the adsorption behaviour of polyaspartic acid on the surface of HA in a CaP_i solution. Polyaspartic acid can be used as an ion chelate for Ca²⁺ complexation, and it can serve as a template for HA biomineralisation by organizing the distribution of Ca²⁺ on its surface. In mineralisation, citrate ions act as a bridge between the acidic peptide moiety and the HA surface. Thus, the synergistic role of citrate ion and acidic peptide may provide new insight into interfacial phenomena during biomineralisation [182]. In addition to the peptide structure, apatite doping also affects the adhesion of HA to the protein surface. The peptide binds through electrostatic interactions between the cationic peptide molecules and negatively charged groups on the crystal surface [174]. For example, HA modified by Sr²⁺ doping was better at promoting protein adhesion than pure HA [183].

3.3.2. Chitosan (CS)

CS is used in BTE because its chemical structure mimics the biological behaviour of glycosaminoglycans (GAGs) [184–186]. CS is a natural linear polymer composed of glucosamine and N-acetylglucosamine units linked by β -1,4-glycosidic bonds with free amino groups. It is the second most naturally occurring polysaccharide. CS is derived from chitin (CN) (see Figure 10), which is isolated from the exoskeletons of shrimps [187], crustaceans, insects, algae, and fungi. To extract CN from, for instance, a crustacean shell, the shell must undergo four steps: pretreatment (washing and drying), demineralisation (acid treatment), deproteinisation (base treatment), and discolouration. CN is then converted to CS through deacetylation (alkaline treatment), which involves the hydrolysis of the acetamide groups and transarrangement of the C-2/C-3 substituent systems in the sugar ring [187,188] (see Figure 10). In general, CS is insoluble in neutral or alkaline solutions due to its specific molecular structure. However, it can dissolve in acidic aqueous solutions ($\text{pH} < 6.5$) by protonating the -NH₂ moieties [189]. Both CN and CS can form hydrogels due to the large number of functional groups (hydroxyl and amino) available for chemical reactions [190,191]. However, CS has a stronger reactivity and higher hydrophilicity than CN because of the more significant number of amino groups from the deacetylation process [192].

Due to its biological properties (biocompatibility, biodegradability, bioactivity) [193] and polyelectrolyte activity, CS is a suitable organic material for the development of organic-inorganic composite materials, functioning as a carrier or stabiliser of hydroxyapatite (HA) [194–196]. Like GAGs, it supports cell adhesion and growth [197,198]. CS also garners attention for its antibacterial properties [199]. Its degradation products are nontoxic, nonimmunogenic, and noncarcinogenic, attributes gaining importance in tissue engineering, wound healing, and drug delivery [200–203].

The properties of CS are primarily influenced by the degree of deacetylation (DD) and molecular weight (MW). Various DDs and MWs of pure CS can be obtained by secondary treatment of CN [204]. Studies have demonstrated that DD affects the hydrophilicity and biocompatibility of CS, while MW largely determines the degradation rate and mechanical properties. Higher DD correlates with more efficient cell attachment, proliferation, and bioactivity of growth factors. When comparing two types of CS with identical DD but different MW, the one with a higher MW exhibits superior mechanical properties and a slower degradation rate. On the other hand, if two types of CS have the same MW but different DD, the CS with a higher DD degrades more quickly, contrary to the behaviour observed in low-molecular-weight CS [205,206]. Theoretically, CS with higher DD and MW is more suitable for biomedical applications.

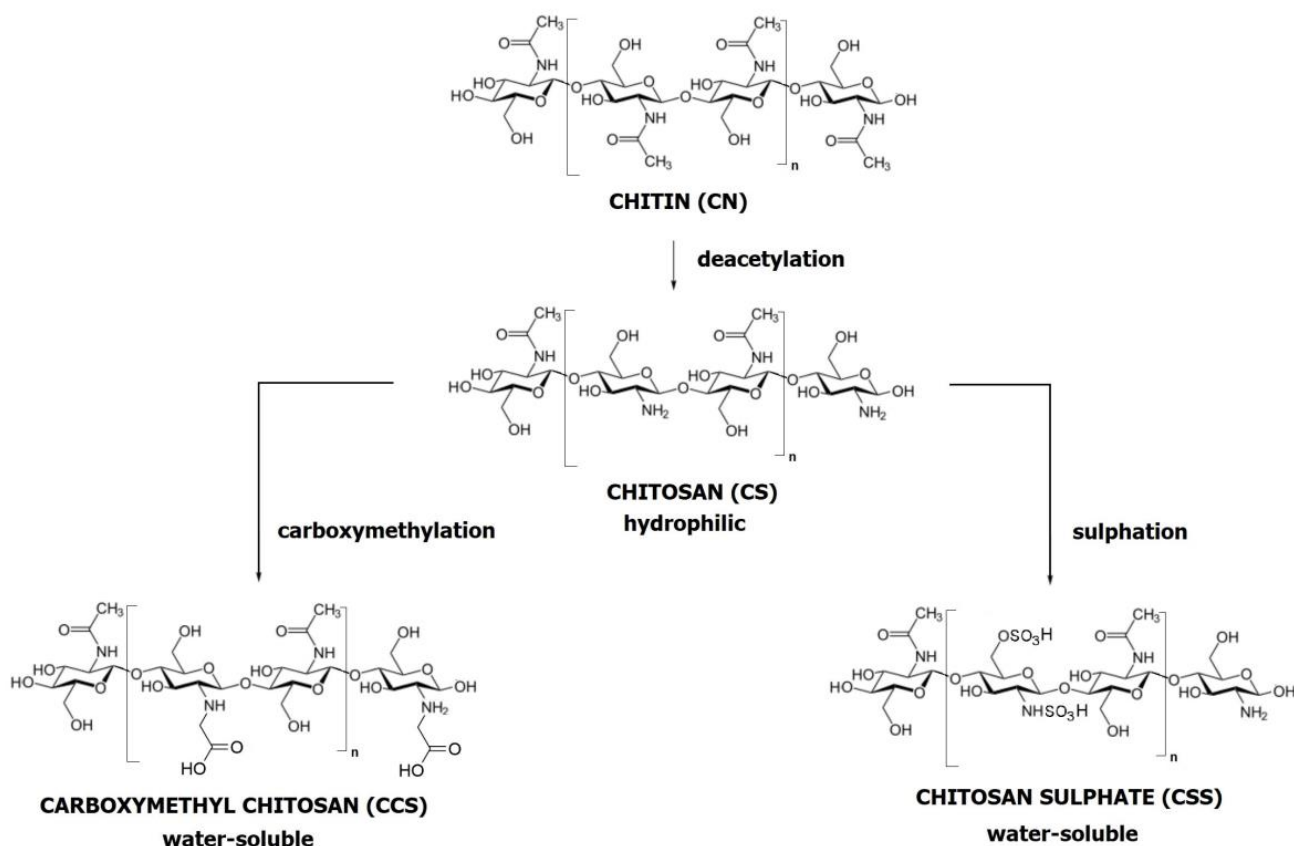


Figure 10. The modification pathways from chitin (CN), through chitosan (CS) to carboxymethyl chitosan (CCS) and chitosan sulphate (CSS).

CS, acting as a nucleation substrate, impacts the growth mechanism of HA crystals, which can occur in various ways. Depending on the type and content of ECM components, HA can assume different morphologies, such as spheres, rods, whiskers, needles, and plates [207]. MD simulations reveal possible chemical bond formations between the N atoms of CS and the Ca atoms of HA. Furthermore, they indicate the presence of hydrogen bonds between phosphate's oxygen atoms and CS's hydroxyl groups. This insight supports understanding the interfacial interaction mechanism, which depends not only on the primary structure of CS but also on the crystal lattice of HA particles. MD simulations predict the behaviour of CS macromolecules on different HA crystallographic planes, indicating that CS macromolecules adsorb more strongly to the HA (1 0 0) surface than to the HA (0 0 1) and HA (1 1 0) surfaces. The interactions between CS and HA were analysed using concentration profiles and pair correlation functions of nitrogen and oxygen atoms in CS [208].

MD simulations are also utilised to understand the mechanism that enhances the mechanical properties of biomaterials intended for hard tissues. Mathesan et al. observed that both Young's modulus and maximum stress increase with the rising content of HA and the degree of CS cross-linking. Changes in the conformation of CS chains and the evolution of intrinsic structural variables are tied to these mechanical properties. Further results suggest that the formation of hydrogen bonds and electrostatic interactions force changes in various systems [209]. MD simulations enable an understanding of the deformation mechanisms of HA crystals under uniaxial stretching and compression at the nanoscale. Depending on tensile and compressive loading direction, these can lead to significant compression/stretch asymmetry and crystal anisotropy [210]. It is particularly notable as native HA tends to be Ca deficient. In areas of Ca deficiency, cracks form and expand along the direction of the vacancy. While Ca vacancies can impair the mechanical properties of hydroxyapatite [211], it remains an open question whether these cracks in nanocrystals

represent the initial stage of a self-healing mechanism (micro-remodelling process) or if they signal the onset of hard tissue damage [212].

The functionalisation of CS is commonly employed to increase bioactivity, mainly focusing on the selective modification of free amino groups [213]. The reactive primary amines and the primary or secondary hydroxyl groups in CS lend it significant versatility [214,215]. CS derivatives are functional across numerous fields, such as food, agriculture, environment, textiles, medicine, and pharmacy. They can be fabricated in various forms, including gels, micro- or nanoparticles, coatings, and scaffolds [216].

A well-known example is chitosan sulphate (CSS) (see Figure 10). CSS mimics the main GAG in alveolar bone: chondroitin sulphate (ChS). CSS is a negatively charged polysaccharide that interacts with positively charged proteins, which could promote osteoblast adhesion, proliferation, or differentiation. The application of nanotechnology is also crucial, as creating structures at the nanoscale level makes it easier to emulate the natural microarchitecture of bone [217,218]. While these mimicry methods cannot fully replicate the complexity and precision of biomineralisation, they can support bone regeneration, especially in its initial stages. Therefore, further research is needed to understand these processes better.

Another example is carboxymethyl chitosan (CMC) (see Figure 10). A CMC-based scaffold coated with tricalcium phosphate (TCP) can biomineralise by forming HA deposits in an ex vivo tooth model [219]. The high mineralisation potential is attributed to carboxyl groups in the organic polymer, which facilitates the spontaneous growth of apatite crystals [220]. The development of these apatite crystals imparts bioactivity to the scaffold and may directly influence its bonding with surrounding structures [221]. Additionally, CMC has antibacterial properties, particularly against cariogenic bacteria, and exhibits considerable potential for wound healing due to its ability to control the expression of the transforming growth factor TGF- β 1, interleukin (IL-1), and tumour necrosis factor (TNF- α) [222–224].

4. Three-Dimensional (3D)-Printed PCL-Based Scaffold

Three-dimensional printing technology has revolutionised BTE by enabling the production of complex architecture PCL-based scaffolds. Moreover, the precision offered by computer-regulated manufacturing in 3D printing allows for optimising control of critical structural properties such as porosity, pore size, and interconnections in bone scaffolds [49,225]. Table 1 lists the key fabrication parameters for PCL-based scaffolds. Manufacturing 3D-printed grafts remains in its preliminary stages, and researchers still need to establish uniform dimensions for these scaffolds dedicated to BTE. Despite this, integrating cutting-edge imaging technologies with 3D printing, such as computed tomography (CT) and magnetic resonance imaging (MRI), enables the designing process of a scaffold architecture for unique tissue defects [13]. As a result, this enhances the efficacy of treating irregular wounds and tissue anomalies, significantly improving medical treatment techniques. In particular, 3D-printed PCL-based scaffolds may significantly contribute to specialised fields such as oral and maxillofacial surgery [11,226] due to their ability to custom-fit unique tissue defects, making them an invaluable tool. Despite the initial high costs associated with research on scaffolds in bone engineering, 3D printing has emerged as a feasible alternative to conventional graft practices [10,227]. Although the high costs associated with the initial stage of research on PCL-based scaffolds in bone engineering are emphasised [119], in the long term, they can reduce the money, time, and effort associated with implantation operations [49]. Consequently, the availability and accessibility of grafts are substantially improved, offering promising prospects for the future of bone engineering.

Table 1. Summary of the varied parameters of PCL-based scaffolds.

Composite	3D Printing Method	Scaffold Shape	Scaffold Dimensions (mm)	Interfibre Gap/Pore Size (μm)	Scaffold (Macro) Porosity (%)	Ref.
PCL/ β -TCP/CGI	SLS	Cylindrical	12.00(D) \times 2.40(H)	300–500	75–77	Liao et al. [17]
PCL/HA, PCL/ β -TCP	FDM	Cubic	Mechanical tests: 10.0(L) \times 10.0(W) \times 10.0(T);	Approx. 800	Approx. 60	Nyberg et al. [228]
		Cylindrical	Other tests: 4.00(D) \times 0.64(H)			
PCL/CS	E-jet 3D printing	Cuboidal	21.0 \pm 1.7(L) \times 12.6 \pm 0.9(W) \times 123.1 \pm 7.2(T)	195.8 \pm 9.1	74 \pm 3	Wu et al. [229]
PCL (subsequently modified by a CS thermogel)	FDM	Cuboidal	Mechanical tests: 10.0(L) \times 10.0(W) \times 2.0(T);	325.2 \pm 26.3	62.4 \pm 0.23	Dong et al. [67]
		Cylindrical	6.0(D) \times 2.0(H)			
PCL (subsequently modified by a CS thermogel)	FDM	Cylindrical	15.0(D) \times 5.0(H)	Approx. 1200	Approx. 65	Hernandez et al. [230]
PCL/ β -TCP	Extrusion-based 3D printing	Cylindrical	8.0(D) \times 2.0(H)	Approx. 300		Kim et al. [231]
PCL/HA	SFF	Cubic	5.0(L) \times 5.0(W) \times 5.0(T)	Approx. 350	Approx. 45	Cho et al. [232]
PCL/TCP	FDM	Cylindrical	6.0(D) \times 4.0(H)	Approx. 420		Kurzyk et al. [233]
PCL/GEL/BC/HA	FDM	Rectangular strips	10.0(L) \times 5.0(W) \times 3.0(T);	Approx. 300	Max. 80	Cakmak et al. [234]
PCL/HA	Extrusion-based 3D printing	Rectangular	Mechanical tests: 10.0(L) \times 10.0(W) \times 2.5(T);	Approx. 700		Gerdes et al. [122]
			Biological tests: 10.0(L) \times 10.0(W) \times 2.4(T)			
PCL/PGA	FDM	Disc	Morphological analysis and mechanical tests: 4.0(D) \times 4.0(H)	250–400, 150–350, >450	60, 50, 75	Hedayati et al. [235]
		Cuboidal	Biodegradation tests: 10(L) \times 6(W) \times 2(T)			
PCL/TCP PCL/HA	Laboratory-prepared 3D plotting system	Cylindrical (ring)	3(D _{in}) \times 8(D _{out}) \times 3(H)	>200 100–200 <100	Approx. 80	Jeong et al. [236]
		Plate	10(D) \times 3(H)			

Table 1. *Cont.*

Composite	3D Printing Method	Scaffold Shape	Scaffold Dimensions (mm)	Interfibre Gap/Pore Size (μm)	Scaffold (Macro) Porosity (%)	Ref.
PCL/HA/HS	FDM	Disc	6.0(D) \times 6.5(H) Biological tests: 6.0(D) \times 1.0(H)	400	70.8	Liu et al. [237]
PCL (subsequently modified by PEGDA)	FDM	Anatomic	24.7(L) \times 11.8(W) \times approx. 4(T)	284 \pm 31	63	Moura et al. [238]
PCL/PLA/HA (subsequently modified by CS/HS)	FFF	Cylindrical Cubic	Mechanical specimen: 6.0(D) \times 8.0(H) Mechanical specimen: 10.0(D) \times 10.0(H) Biodegradation specimen: 5.0(L) \times 5.0(W) \times 5.0(T)	500		Thunsiri et al. [239]
PCL/HA	Dual-extruder 3D printing	Cuboidal	1.0(L) \times 5.0(W) \times 5.0(T)	77.1 \pm 13.8		El-Habashy et al. [240]
PCL/HA	FFF	Cuboidal	15(L) \times 15(W) \times 5(T) 15(L) \times 15(W) \times 3(T) 35(L) \times 13(W) \times 8(T)	Approx. 1200		Kim et al. [241]
PCL/HA	Cryogenic 3D printing	Orthogonal grid	10(L) \times 10(W) \times 2(T)	235 \pm 43	42.84 \pm 1.41	Li et al. [242]
PLA/PCL/HA	Indirect 3D printing	Cubic	5(L) \times 5(W) \times 5(T)	141.0 \pm 47.0	69.00–70.00	Oryan et al. [117]
PCL/HA/SPION	3D printing with a screw-based extruding system	Cubic Disc	5(L) \times 5(W) \times 5(T) 15.0(D) \times 5.0(L)	Approx. 250	45.81	Petretta et al. [243]
PCL/AgNps	FDM	Disc	10.0(D)	431.7 \pm 24.6		Radhakrishnan et al. [131]
PCL/CS	3D bioprinting	Cuboidal	10(L) \times 10(W) \times 5(T)	360	Approx. 55	Rezaei et al. [244]
PCL	3D printing with novel plasma-assisted bioextrusion system	Cuboidal	11(L) \times 11(W) \times 5(H)	500 1000 1500 2000	60.7 75.5 78.6 85.7	Xu et al. [245]
PCL/CS PCL/ β -TPC	3D pneumatic melt extruded scaffold generation	Cuboidal	16.0(L) \times 16.0 (W) \times approx. 4.0(T) Biological tests: 4.0(L) \times 4.0(W) \times approx. 2.5(T)	381 \pm 6 395 \pm 17	47.0 \pm 2.0– 63.0 \pm 2.0	Yoshida et al. [121]
PCL/HA	3D printing with pneumatic chamber system	Cuboidal	Mechanical tests: 12(L) \times 12(W) \times 4(T)	Approx. 300		Zimmerling et al. [132]

Table 1. *Cont.*

Composite	3D Printing Method	Scaffold Shape	Scaffold Dimensions (mm)	Interfibre Gap/Pore Size (μm)	Scaffold (Macro) Porosity (%)	Ref.
PCL/HA	3D printing with a screw-fitted chamber system	Cylindrical	10(D) \times 2.5(H)	Approx. 350	58.0–60.0	Biscaia et al. [246]
PCL	Combination of 3D printing and electrospinning	Disc	21(D) \times 1(H)	Approx. 300		Gonzalez-Pujana et al. [247]
PCL/HA	FFF	Cylinder	Mechanical tests: Approx. 1.6(D) \times 80(H)	Approx. 400	37.0	Rezania et al. [22]
PCL/HA/PEGDA	3D printing with extrusion system	Disc	10(D) \times 3(H)	380	51.53 \pm 2.00 –52.20 \pm 1.67	Sousa et al. [248]
PCL/HA	FFF	Cuboid	Morphological analysis: 15(L) \times 15(D) \times 2(H) Mechanical tests: 15(L) \times 15(D) \times 4(H)	Approx. 550	60.0 \pm 0.9 –65.4 \pm 0.3	Wang et al. [16]
PCL/HA PCL/TCP	FDM	Cuboid	31.0(L) \times 26.7(D) \times 10.0(H)	Gradient of approx. 200, 300 and 500, 600	Approx. 52.0	Daskalakis et al. [34]
PCL	SLS	Disc	20(D) \times 2(H)	Approx. 500, and approx. 700	49.7 \pm 3.0–63.6 \pm 3.0	Janmohammadi et al. [18]
PCL/CS (subsequently loaded with VAN)	FDM	Disc-shaped	8.00(D) \times 1.50(H)	Approx. 200	Approx. 59.0	López-González et al. [249]
PCL/CS	RP	Anatomic (mandibular condyle)		100–200		Lee et al. [250]
PCL/MMBG/Al ₂ O ₃	LDM	Cubic	5(L) \times 5(W) \times 5(T)	0.005–0.020 (mesopores)	Above 80	Najafabadi et al. [251]

Abbreviation: PCL: polycaprolactone; TCP: tricalcium phosphate; HA: hydroxyapatite; HS: heparan sulphate; MMBG: magnetic mesoporous bioactive glass; AgNps: silver nanoparticles; PEGDA: diacrylate poly(ethylene glycol); VAN: vancomycin; RP: rapid prototyping; SLS: selective laser sintering; FDM: fused deposition modelling; LDM: liquid deposition modelling; FFF: fused filament fabrication; SFF: solid freeform; L: length; W: width; T: thickness; D: diameter; D_{in}: inner diameter; D_{out}: outer diameter.

4.1. Processing Conditions

The method of 3D printing for creating bone engineering scaffolds did not develop earlier because solvent casting was the primary fabrication technique. This delay can be attributed to the lack of suitable materials and control methods for extrusion [16,252]. Only recently has research focused on producing dispersions of nanomaterials in polymer matrices, particularly in PCL, which has led to the development of 3D-printed scaffolds in tissue engineering. These processes help meet the requirement for adequate physical connectivity, which is crucial for effective cell anchoring and adhesion [246].

4.1.1. Filament Processing

The extrusion process for PCL filaments necessitates careful consideration of additive content, rheological properties, and processing conditions tailored specifically for the fused filament fabrication (FFF) 3D printing method. Extruded PCL-based filaments, often combined with HA or CS, attract substantial interest due to their osteoinductive potential. Unique behaviour is observed when materials like PCL/HA are used during 3D printing. They form distinctive structures with a higher viscosity than the PCL control sample, requiring increased oversight due to an elevated risk of printer nozzle clogging. Maintaining comprehensive control over the filament deposition temperature and the distance between the filaments is critical to ensuring a successful 3D printing process [16].

Challenges arise when an increase in the HA concentration in the PCL-based filament leads to a corresponding increase in viscosity. This issue can be mitigated by elevating the heating temperature [121,253]. As for material composition, Biscaia et al. argued that incorporating HA into the PCL matrix enhances its mechanical properties, but these enhancements do not proportionally increase with the ceramics' presence in the composite. The most common weight ratio of polymer to ceramic is 80/20 or 60/40 wt.% [246,254]. In contrast, Rezania et al. suggested that the optimal concentration of HA in the PCL matrix is approximately 30 wt.% [22].

Excessively high HA content and greater fragmentation can increase the risk of ceramic particle agglomeration in the polymer matrix, resulting in a brittle material. However, a proper arrangement of bioceramic reinforcement in the polymer matrix can prevent stress concentration [22,255] and promote the structural integrity of the final material [16,256].

4.1.2. Three-Dimensional (3D) Printing

In the context of processing, PCL is one of the most preferred polymers for extrusion-based 3D printing dedicated to medical applications due to its low melting point of about 60 °C (melting temperature, T_m) [33,144,257]. Furthermore, the thermal degradation process of PCL does not begin until approximately 300 °C (degradation temperature, T_d) [34]. This fact indicates high static and dynamic thermal resistance due to the range between T_m and T_d , known as the wide processing window.

From a rheological perspective, molten PCL displays a broad range of viscoelastic behaviours. At lower temperatures within the processing window, it exhibits viscoelastic properties, whereas at higher temperatures, it assumes the characteristics of a viscous liquid. Consequently, the viscosity within this wide processing window can vary during printing. Therefore, adjusting printing parameters (temperature, melt index, printing speed) ensures consistently structured outcomes with similar pore sizes, shapes, and interconnections [121].

Interestingly, Ogata et al. demonstrated that polyesters (e.g., PLA) that have been melted once do not significantly change their viscosity upon reheating at a higher temperature [258]. However, concurrently, Yoshida et al. observed that the polymer's heating duration affects its extrusion's smoothness. This effect is likely due to small bubbles in the molten mix escaping during prolonged heating, which results in a more even distribution of extrusion pressure [121].

Moreover, the optimal velocity and temperature printing adjustment relies not only on the polymer features (such as the MW and polydispersity of PCL) but also on the

individual 3D printer heating system and variable ambient temperature. Although DSC studies demonstrate the low melting point of PCL (even approx. 51 °C) [259], the optimal temperature for 3D printing PCL from the extruded filament is around 85–90 °C [121]. Therefore, the wide PCL processing window confirms its potential for creating detailed and complex scaffold structures.

Interestingly, Ghorbani et al. [260] observed that the incorporation of HA induces a higher melting temperature and degree of crystallinity in PCL. Conversely, Biscaia et al. noted that incorporating HA into PCL reduces its endothermic melting enthalpy. This effect is likely attributable to the high crystallinity of HA, which is thought to accelerate the nucleation of PCL chain segments, thereby generating a lower degree of PCL crystallinity [246]. Moreover, 3D printing technology promotes oriented crystallisation [261]. The formation of row nuclei facilitates this process, further enhanced by the flow stress applied to the polymer melt during printing [12,261]. Notably, the crystallinity of the polymer significantly influences the mechanical properties of the produced scaffolds [246,248,261].

Lastly, 3D printing technology offers a distinct advantage over conventional manufacturing methods, such as salt leaching [262] and electrospinning [263,264]. As it does not require toxic solvents, 3D printing provides a safer and more environmentally friendly solution.

4.1.3. Hybrid Techniques

Despite its numerous advantages, a 3D-printed PCL-based scaffold has limitations, particularly in the postprocessing stage. The most significant of these are the following: (i) the sterilisation process required before implantation, and (ii) the brittleness of the final scaffold. First, sterilizing PCL-based scaffolds without disturbing their structure can be challenging. This issue partially depends on other characteristics such as mechanical, degradation, surface, and biological properties. Second, some researchers have adopted innovative postprinting modifications like enveloping the 3D-printed PCL scaffold with a layer of CS hydrogel [265] or using a PCL/CS composite [266] hydrogel to develop electrospun sheets, offering a potential solution to the brittleness problem [67]. It is worth noting that CS maintains its thermal stability at PCL printing temperatures. The first melt isothermal process, which occurs above 100 °C, relates more to the loss of bound water than to polysaccharide breakdown [264], thereby preserving its structural integrity during printing. Therefore, to tackle the above problems, 3D printing is combined with other methods, facilitating the development of scaffolds that encapsulate the benefits of both techniques.

3D printing can be combined with electrospinning to produce a scaffold that provides high control over micro- and macrostructure, shape, and mechanical strength. Electrospinning enables the production of fibres with dimensions ranging from microns to the submicron scale. Gonzalez-Pujana et al. demonstrated high metabolic activity and mineralisation of cells cultured on microfibres made from a PCL-based scaffold. Due to electrospun fibres, a microscale structure mimics the cells' natural environment, promoting osteogenic differentiation [247].

Another hybrid technology involves the combination of 3D printing and freeze-drying. This technology can produce spongy structures with controlled pore size gradients, resulting in scaffolds that exhibit interconnected and adjustable pore structures [267]. When a scaffold is soaked in a solution containing growth factors or other bioactive substances and then subjected to freeze-drying, these bioactive factors become fixed within the scaffold structure [268]. For instance, PCL has been functionalised with a decellularised bone extracellular matrix (dbECM) to produce osteoinductive fibres for 3D printing. Adding bone dbECM to PCL enhanced the mechanical properties of the resulting scaffold, improved cell adhesion, and promoted osteogenesis in mesenchymal stem cells (MSCs) [21,269].

4.2. Structural and Mechanical Properties

4.2.1. Size and Geometry of Interconnected Pores

One of the key aspects of scaffolds is their external morphology structure, which affects their performance and tissue interaction. The parameters closely related to the functionality of the scaffold are the size and geometry of pores and their interconnections.

Well-designed porosity with interconnected pores stimulates new bone tissue growth [270]. Additionally, vascular infiltration can be modulated by controlling pore size. Macropores provide space that facilitates cell migration and tissue penetration, thus promoting bone tissue regeneration. Numerous studies have examined the effect of varying pore sizes on the adhesion, proliferation, and migration of different cell types, such as osteoblasts, chondrocytes, and fibroblasts [271]. Oh et al. reported that the appropriate pore size for osteoblast and chondrocyte growth ranges from 300 to 400 μm , while fibroblasts should be around 200 μm [272]. Therefore, the suitable pore size in PCL scaffolds can be estimated to lie between 200 and 400 μm [238]. However, two optimal pore size ranges were also distinguished: 200–600 μm [16,273,274] and 450–700 μm [275]. For instance, Wang et al. used a pore size of 550 μm , which falls within these ranges [16]. Furthermore, pore sizes above 300 μm have been reported to improve vascularity and bone ingrowth [131,246,276–278].

Interestingly, Ghayor et al. challenged the long-standing assumption that the optimal pore size for bone scaffolds ranges from 0.3 to 0.5 mm. They contend that the ideal pore size should fall between 0.7 and 1.2 mm. These assertions stem from their work with TPC-based scaffolds produced through 3D printing, which they assessed for potential in facilitating *in vivo* bone formation. They suggest that these findings may pave the way for innovative methodologies in treating bone defects [36,108].

Building on Ghayor's paradigm regarding larger pore sizes, the research of Hernandez et al. warrants consideration. They devised a hybrid system using a PCL-based scaffold featuring a pore size of 1.2 mm complemented by a hydrogel. This design exhibited cytocompatibility, as evidenced by the successful adhesion and viability of hMSC within the hydrogel matrix and on the solid scaffold surfaces. Furthermore, biominerallisation tests in SBF highlighted the nucleation and growth of apatite crystals both within the hydrogel and on the PCL scaffold, attesting to its bioactivity. While this hybrid system is optimised for addressing long bone defects, comprehensive *in vitro* and *in vivo* studies remain indispensable [230].

Although pore size and geometry are known to influence cell behaviour and tissue formation *in vitro*, it is unclear how this translates to *in vivo* scenarios [279]. However, pore architecture inside a scaffold is inevitably necessary for effectively binding growth factors and nutrient transport to cells.

In addition to macropores, scaffolds also contain micropores, which can have positive and negative effects. On the one hand, they can accelerate surface roughness, degradation, and resorption of PCL, which is inherently slow. On the other hand, these micropores could reduce the structure's compressive strength [246]. Therefore, a balance must be found to maintain the scaffold's structural integrity.

Equally important is the scaffold's mechanical behaviour, which heavily depends on a precisely defined pore geometry and directly affects cell interaction. Scaffold structures can be fabricated in various forms, such as helixes, meshes, rings [265], or orthogonal, circular, and sinusoidal shapes [280]. Thus, innovative, versatile, and efficient strategies to 3D print PCL scaffolds with unique anisotropic and curved geometries could better mimic natural tissue.

In conclusion, while size and geometry influence cell behaviour and tissue formation *in vitro*, our understanding of how this translates to the *in vivo* scenario remains limited [108,279]. However, one thing is certain: pore architecture is a necessary, though not sufficient, condition for the effective binding of growth factors and transport of nutrients to cells. By appropriately designing porosity, pore size, and geometry, we can achieve scaffolds with optimal mechanical properties, enhancing osteoconductive features.

4.2.2. Mechanical Compressive Strength and Elastic Modulus

In BTE, predicting the forces exerted on native bone during normal function is particularly relevant for designing, fabricating, and integrating a printed scaffold with the host. The most important mechanical property parameters for alveolar bone are the compressive strength and modulus of elasticity, as, during the opening and closing of the jaw, the most significant force induced at the dental symphysis is the compressive force in the transverse direction [281]. The mechanical properties of the 3D-printed PCL scaffold's layer-by-layer construction can be estimated based on the compact and cancellous bone structure's volume ratio.

Generally, the compact structure of bone, depending on the orientation of HA crystal growth (transverse or longitudinal), mechanically resembles either a semibrittle or viscoelastic material [282]. The transverse compressive strength of the compact bone structure ranges from 131 to 224 MPa. The modulus of elasticity for compact bone is 17.0 to 20.0 GPa in the longitudinal direction, with a shear modulus of 3.30 GPa and a structural density of 1.80 g/cm³ [283].

As for the cancellous bone structure, it is highly porous, and its density is 0.20 g/cm³. The compressive strength of the spongy bone structure depends on its apparent density and ranges from 2.0 to 5.0 MPa. The modulus of elasticity ranges from 90.0 to 400.0 MPa [284].

The volume ratio of these structures, constituting the alveolar bone, is determined by various factors such as the location of bone loss in the alveolar bone, age, sex, and health status. The optimal compressive strength might range between 5.0 and 131.0 MPa, while the elastic modulus could lie between 400.0 MPa and 17.0 GPa. Lv et al. contend that scaffolds, which mimic the structure of natural cancellous bone, adapt more adeptly to the microenvironment [285]. Conversely, Pitrolino et al. questioned the validity of designing scaffolds to align with the mechanical properties of native bone tissue. They argued that designing an optimal cellular niche should take precedence over delineating the mechanical strength specifications of scaffolds, as osteocytes—when formed in the appropriate cellular niche—assume the role of structural and mechanical integration within the tissue [286].

Although modelling the alveolar bone's mechanical properties requires more detailed research and analysis, compact and cancellous bone structures' compressive strength and elastic modulus provide valuable data. Implanting a scaffold with either excessive or insufficient mechanical strength at the implant site could fail to support native bone growth or lead to bone resorption. Thus, the scaffold's ability to provide the required mechanical support is a critical criterion for the resulting structure. For instance, Wang et al. obtained PCL-based scaffolds with HA (20 wt.%), achieving compressive strength and elastic modulus of 8.0–11.7 MPa and 11.4–29.2 GPa, respectively. According to the proposal above, these values meet the proposal requirements of the mechanical property of trabecular bones [16].

Apart from orientation, location, and host age, the water environment plays a crucial role in the mechanical assessment of the scaffold. The behaviour of bone in a wet state significantly diverges from that in its dry form [79,287]. To facilitate proper regeneration without notable deformations, the PCL-based scaffold—modified by introducing HA and CS—should offer an elastic modulus identical to that of hard tissues: 1500 MPa in dry and approximately 10 MPa in wet conditions. Pressure causes the liquid to be extruded from the porous structure, thereby increasing the colloidal osmotic pressure and, consequently, the Young's modulus. An elevated Young's modulus enhances resilience to high stress [288,289], and the higher the elastic modulus, the less likely the scaffold will deform.

4.2.3. Mechanotransduction

The alveolar bone develops healthily when optimal mechanical forces act on it. Osteocytes embedded in the bone matrix are the primary mechanically sensitive cells involved in the transduction of mechanical stress into a biological response [6]. It is assumed that resorption of the alveolar bone occurs especially when a tooth is missing, i.e., when the alveolar bone is unaffected by mechanical forces. Regarding the designed scaffolds, structural parameters (porosity, pore connections, pore size, and pore geometry) and mechanical

parameters (compressive strength and modulus of elasticity) affect how osteocytes perceive mechanical stimuli, which may affect their biochemical reactions. In this respect, the intramembranous ossification of the alveolar bone can be analogously compared to the piezoelectric effect. Since the mechanical stresses in the piezoelectric material generate an electric field (electrical signal), the mechanical stresses in the alveolar bone initiate a biochemical signal towards enzymatic activation for biominerallisation, which ultimately ends in ossification. This unique ability to convert mechanical forces into a biochemical signal is called mechanotransduction. Probably, ionic proteins are responsible for mechanotransduction [290]. These proteins immediately respond to mechanical stimuli by initiating an ionic current. As evidence grows regarding the critical role of this phenomenon in the management of physiological processes, there is a need to identify these proteins [291]. Design scaffolds taking this phenomenon into account become increasingly urgent.

Understanding the relationship between the structural and mechanical parameters of the scaffold and its mechanotransduction capacity is crucial in bone tissue regeneration [122]. The question arises: how does mechanotransduction affect the ossification process? Al-Maslamani et al. developed cell-stretching devices to explore the molecular pathways responsible for cellular responses to mechanobiological processes [292]. Therefore, in the context of BTE, essential factors influencing regenerated bone dynamics are not only biological but also mechanical issues. Figure 11 shows theoretical diagrams of the relationship between mechanical stress (MS), biochemical signals (BS), and the ossification process (OP). Ossification of the healing alveolar bone uses physical movement, mainly compressive forces (less stretching), imitating orthodontic tooth movement.

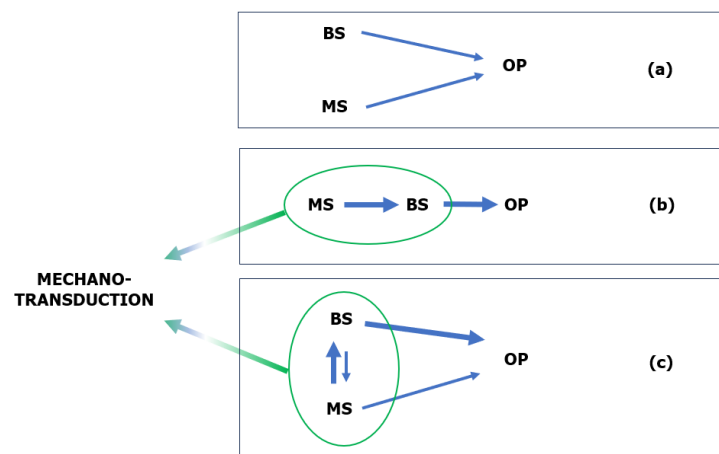


Figure 11. Diagrams of the relationship between mechanical stress (MS), biochemical signals (BS), and ossification process (OP). Several models explaining the relationship between MS and BS in OP may be considered. In the parallel model (a), MS and BS are presumed to function independently, yet they concurrently influence OP without mechanotransduction. In the series model (b), it is suggested that MS initiates BS, which then triggers OP, indicating the presence of mechanotransduction. Finally, the series-parallel model (c) proposes that MS and BS interact with each other through a coupled mechanism, affecting OP, which is characteristic of mechanotransduction. Option (a) is a theoretical concept and is regarded as the least likely, while option (c), although more complex, is considered the most plausible.

In a biomechanical context, tensile stress breaks down adjacent ECM molecules, thereby evenly distributing protein molecules. Compressive stress causes the accumulation of adjacent molecules, shortening the distance between HA crystals and affecting bone tissue growth. Both of these stresses regulate bone tissue homeostasis at the local site. Undoubtedly, bone tissue expands as a result of its regular mechanical stimulation. Due to the nature of the load, this stimulation can be divided into two types, static load (Wolf's law) and dynamic load (Delpech's law), which affect the formation of bone trabeculae. Too little or too much static load on the bones causes osteoporosis, while too little or too

much dynamic load causes atherosclerosis. Disproportionate stress and friction promote inflammation, activating the action of osteoclasts and cytokinins [289]. The hypothesis remains unsettled as to whether the action of compressive and tensile forces in the early period of alveolar process healing is necessary.

4.3. Degradation Properties

A particular challenge in designing a PCL-based scaffold is considering its degradation properties. From a materials engineering perspective, degradation deteriorates the structural integrity of the structure and leads to a decline in the mechanical properties of the scaffold. It indicates that a scaffold must be designed so that native bone tissue forms in place of the degraded polymer, subsequently assuming the structural and strength functions. The primary task within this paradigm is to synchronise scaffold degradation kinetics with tissue regeneration rates while maintaining identical structural and mechanical integrity [293]. In the context of bone engineering, PCL has a long degradation time of two to four years [264,294], while bone remodelling takes about six months [295]. Factors that may affect the rate of degradation and the structural and mechanical integration of the scaffold include the following:

- Material characteristics (degree of crystallinity, polydispersity and MW of PCL, amount and type of components with osteoinductive potential in the PCL matrix).
- Topological features (porosity, size and shape of pores, thickness of solid material).
- Degradation environment (pH, ion exchange) [34,296].

4.3.1. Degradation Mechanism

Understanding the degradation mechanism of PCL is essential for its application in the biomedical and pharmaceutical domains [297]. PCL belongs to semicrystalline polymers. Chemical degradation primarily occurs in the amorphous regions of PCL where hydrolysis of ester bonds takes place, breaking longer PCL chains into oligomeric (shorter) ones [296,298,299]. Yoshida et al. reported that the hydrolysis of PCL ester groups exhibits first-order kinetics, meaning that the degradation rate depends mainly on the amount and MW of the polymer [121]. However, an autocatalytic effect emerges in the amorphous regions as the degradation progresses. The cleavage of labile ester moieties, and thus the formation of oligomers with carboxylic and hydroxyl end groups, can uncontrollably accelerate the hydrolysis of adjacent ester moieties [300,301]. PCL degradation products diffuse less easily than other polyesters with shorter aliphatic chains. In addition, the oligomers formed are acidic. Yoshida et al. recorded a pH value that dropped from pH 7.45 to pH 6.11 within 28 days of degradation, a finding also consistent with the downward trend reported by Sung et al. [32]. Lowering the pH confirms that acidic metabolites are formed due to PCL degradation [264]. Although a decrease in pH occurs, PCL degradation products induce fewer pH changes in the local medium than other aliphatic polyesters [296]. Incorporating ceramic particles into a PCL matrix exhibits buffering behaviour [117]. However, a comparison of the degradation kinetics of PCL-based scaffolds containing different ceramic materials still needs to be included [34].

Although the amorphous regions of semicrystalline polymers are more susceptible to hydrolytic degradation [296,299], degradation also occurs in the less accessible crystalline regions, which, in the case of PCL, are represented by numerous spherulites. As the degradation of the intact chains in the crystalline regions progresses, the form of the spherulites changes into so-called “crystalline residues” that take on the structure of “elongated-chain crystallites” [297].

Along with hydrolytic degradation, the phenomenon of recrystallisation occurs. It involves the amorphous areas of PCL rearranging to more ordered structures in contact with the crystalline areas (interspherulitic boundaries). Li et al. reported that adding PCL (approx. 25 wt.%) to other aliphatic polyesters such as PLA (approx. 75 wt.%) leads to an increase in the degree of crystallinity of the composite—from the initial 14 wt.% by mass up to 52 wt.%—after 63 weeks of research on the degradation process. This reorganisation is

attributed to the low glass transition temperature of the polymer [302]. The preservation of amorphous regions and the dominance of imperfect and defective crystalline regions helps counteract the phenomenon of recrystallisation, thereby increasing the degradation rate. It can be found that the addition of CS reduces the spherulites and forms more distinct interspherulitic PCL boundaries [260]. The effect of counteracting the phenomenon of recrystallisation is attributed to the hydrolysis of glycosidic bonds between polysaccharide rings in CS chains [265,303], which aids in the hydrolytic degradation of PCL ester groups.

In vivo, enzymatic degradation also occurs, which attacks the crystalline regions of PCL, disintegrating the scaffold structure. In vitro studies in which a PCL-based scaffold was subjected to enzymatic degradation began to be reported in the literature [304,305]. However, Bartnikowski et al. exposed PCL-based 3D scaffolds to concentrated hydrochloric acid (HCl). Acid etching of these scaffolds with different concentrations of HCl, due to the intense penetration of protons (H^+), ultimately led to the disintegration of the scaffold structure. The features of acid hydrolysis represent degradation under physiological conditions. Acid digestion can be compared to the action of enzymes in the oral cavity at the site of the defect, which, due to inflammation, is locally acidic. By imitating the microenvironment of the cavity, one can estimate material characteristics and scaffold topology, both of which are dependent not only on the structure and components but also on the technique used to manufacture the material [296].

4.3.2. Structural and Mechanical Integrity

The type of erosion determines the structural and mechanical integrity of PCL-based scaffolds. Subject to hydrolytic and enzymatic degradation, scaffolds may undergo either surface or bulk erosion or a combination of both.

Surface erosion is common with polyesters, which, despite being hydrophobic, are highly susceptible to surface hydrolysis. The advantage of surface erosion is that while the structure's size decreases with weight loss, its density remains unchanged. This characteristic allows the scaffold to maintain its mechanical integrity, a property critical to BTE. Generally, the surface will degrade initially when the scaffold structure comes into contact with a degrading medium. As the medium penetrates the material, most of the scaffold's solid material begins to break down. This process results in bulk erosion, during which the construct's volume stays the same, but there is a decrease in density and mechanical strength [306].

Although surface erosion is generally slower than mass erosion, it is typically more desirable because the material decomposes uniformly at a constant rate, making it easier to control. Furthermore, uncontrolled autocatalytic degradation often occurs in conjunction with progressing bulk erosion. It is frequently observed with polyesters, as their acidic degradation products cannot easily diffuse through the polymer network. This results in a localised increase in acidity, which in turn accelerates the scaffold's degradation in an uncontrolled manner [29,307].

The task involves designing a scaffold with a specific surface erosion timeline and estimating the final stage of degradation when simultaneous surface and volume erosion occurs to predict the time of structural and mechanical disintegration. Maintaining structural and mechanical integrity depends not only on the underlying mechanism of PCL degradation but also on the scaffold's topology and the surrounding microenvironment [296].

The type of erosion also depends on the fibre thickness and the nature of the solid scaffold material. For instance, once the critical thickness of aliphatic polyester fibre exceeds 2 mm, the degradation mechanism changes from surface erosion to bulk erosion, regardless of ion exchange [306]. In the core part of the materials, partially degraded oligomeric chains accumulate and initiate hydrolysis with a high catalytic effect, potentially leading to accelerated and uncontrolled hydrolytic degradation in the core part—a phenomenon referred to as core-accelerated bulk erosion. However, concerning poly(L-lactide) PLLA, a polyester belonging to the same polymer family as PCL, Tsuji et al. observed that when the diameter of the scaffold fibres is less than 2 mm and optimal ion exchange is ensured, PLLA

tends to undergo surface erosion [297]. In this case, ions do not diffuse into the material, meaning that a substantial part remains unaffected. Interestingly, Grizzi et al. noted that foils, powders, and microspheres of PLLA degrade much more slowly than solid material samples [308]. The smaller the polymer size (corresponding to an increased specific surface area), the slower the degradation rate.

Although enhancing the surface area of aliphatic polyester-based scaffold fibres slows down degradation, the degradation process becomes more uniform and easily controlled due to the reduction in internal heterogeneous autocatalytic degradation. An illustrative example is a study on the degradation rate of films of another aliphatic polyester (e.g., PLLA) about porosity. It was found that nonporous PLLA degrades faster than porous PLLA [309,310]. This phenomenon can be attributed to the fact that ion exchange is facilitated in a porous structure, thus inhibiting autocatalytic bulk erosion and maintaining the structure's integrity for extended periods.

The type of erosion also depends on factors related to the degradation medium, such as pH, temperature, and the presence of ions and enzymes. Therefore, the site of implant placement is vital. In areas with poor vascularisation and low diffusion, degradation products tend to linger, resulting in increased acidity. Bulk erosion is in environments where the ion exchange of Ca^{2+} and P_i is restricted [297]. Consequently, the type of erosion is strongly determined by the ion exchange characteristics of the microenvironment. When optimal ion exchange occurs, the types of erosion generally occur sequentially: surface erosion precedes bulk erosion.

In conclusion, the degradation of aliphatic polyesters, e.g., PCL, involves a complex interplay of several parallel and successive phenomena, including water absorption, cleavage of ester bonds, neutralisation of terminal carboxyl groups on the surface, internal autocatalysis, diffusion and solubilisation of oligomers, and recrystallisation effects [311,312]. The type of erosion that PCL naturally undergoes in a physiological environment is currently debated. Although pure PCL scaffolds do not experience significant erosion initially (nominally less than 1 wt.% loss, up to 1 to 3 months) [313,314], the situation alters slightly for a PCL scaffold with incorporated ceramic particles or CS. These scaffolds exhibit weight loss within the first seven days. However, the origin of this material loss is challenging to ascertain. It could be attributed less to PCL degradation and more to the strong binding of water to HA and CS, as these compounds make it difficult to remove moisture [121].

4.4. Surface Properties

A scaffold in bone engineering should be biocompatible and biodegradable, and also, its surface should be conducive to migration and anchoring osteoblasts as a direct site of interaction with host cells. The scaffold's physical properties (e.g., surface roughness, development of the specific surface area) [315] play a critical role in providing cell anchorage [16]. Successful anchoring enables effective cell adhesion [316]. Cell adhesion allows cells to stick to the scaffold's surface through specific molecular interactions, promotes cell proliferation, and enables cell differentiation through the development of a specific surface area [251,317].

Natural polymers such as proteins (e.g., CGI) and polysaccharides (e.g., CS) are considered suitable materials for facilitating osteoblast anchoring due to the presence of functional groups that differ in polarity, electrostatic charge, and ability to interact via van der Waals forces [318]. Unfortunately, their relatively poor mechanical properties, such as high brittleness and insufficient compressive strength, do not meet the necessary structural and mechanical requirements. Thus, while natural polymers possess high osteoinductive potential, they lack osteoconductive features. This leads to the consideration of synthetic biopolymers like PCL in BTE. PCL has appropriate mechanical properties but is marked by significant hydrophobicity [319]. Modifying a PCL-based scaffold is required to improve its surface wettability [103,320].

One method of enhancing the hydrophilicity of a PCL-based scaffold surface is through the incorporation of HA. The presence of ceramic particles increases the material's hy-

drophilicity due to the micropores that appear on the surface of the scaffold fibres, which are associated with greater polarity. While the reasons for the altered surface architecture are unclear, as noted by various authors, a strong correlation has been identified between increased roughness and improved cell adhesion [152,246]. The uniform distribution of HA in the PCL matrix, with some particles exposed on the surface of the filament and some forming agglomerations, amplifies its cellular activity [16,321]. For instance, a higher value of surface roughness of the scaffold fibres was also observed when the concentration of CS was increased [121].

Two specific methods for surface functionalisation, aimed at eliciting desired biological responses, are also noted: gas plasma treatment and the exposure of the polymer surface to other reactive reagents, such as through acid and alkali etching [319].

These methods enhance surface roughness and introduce new functional groups through the covalent modification of the polymer surface due to surface degradation. These surfaces can then be further modified by attaching biologically active compounds such as CGI and growth factors (e.g., BMP-2). This wetting effect can enhance the degree of biomimetic mineralisation [322–325]. The surface properties of PCL can be altered by combining plasma treatment and collagen modification. Studies were also conducted to immobilise collagen on the surface of ultrathin PCL films, significantly improving hydrophilicity after surface modification [326]. The rate of cell attachment and proliferation on the resulting films was increased. Integrins, cytoskeletal and ECM proteins such as CGI and the arginyl-glycyl-aspartic acid (RGD) peptide, can be covalently attached or physically deposited (via electrostatic adsorption) on the PCL surface.

Another method to increase the hydrophilicity of a PCL-based scaffold involves etching with concentrated acids or bases. For instance, a PCL-based scaffold can be immersed in a NaOH solution for 24 h, increasing hydrophilicity promoted by alkaline hydrolysis [238]. This process contributes to the formation of additional carboxylate (COO^-) and hydroxyl (OH^-) groups at the ends of the PCL chain on the surface of the scaffold, thereby increasing its roughness through surface erosion. The interaction of the PCL-based scaffold with a drop of water has been found to correlate with scaffold–protein and scaffold–cell interactions [327,328]. Therefore, the contact angle can be interpreted as an indicator of the scaffold’s initial cell adhesion capacity. For instance, PCL scaffolds with higher HA concentrations (20 wt.%) exhibit a smaller contact angle (approx. 78°), reflecting superior hydrophilicity [236].

5. Conclusions

Designing scaffolds for alveolar bone augmentation poses a significant challenge. Any discussion to determine scaffold characteristics should begin with a systematic meta-analysis of biomimetic mineralisation and ossification. Currently, the literature primarily consists of phenomenological descriptions of these processes. Although our understanding of bone tissue growth at the micro- and macroscopic levels is limited, an examination of the mechanisms of biomimetic mineralisation and ossification through the lens of materials engineering and bone tissue can provide direction for the development of osteoconductive scaffolds with osteoinductive potential.

The initial proposal for design involves the selection of materials. A scaffold based on polycaprolactone (PCL), characterised by its optimal biocompatibility, biodegradability, and bioresorbability, emerges as a suitable candidate for scaffolds that exhibit osteoconductive characteristics. Synthetic polyesters can undergo modifications to render their properties suitable for bone tissue engineering (BTE). PCL-based scaffolds, when modified with hydroxyapatite (HA), type I collagen (CGI), and chitosan (CS) particles, demonstrate high osteoinductive potential. Molecular dynamics (MD) simulations of the CGI–HA and CS–HA interactions serve as a guide for in vitro testing.

The strategy for designing PCL-based scaffolds is in its nascent stages. Currently, it involves employing heuristic methods to explore the most effective ways of obtaining and analysing scaffold properties. A research path ranging from fundamental principles to

clinical applications must be standardised to implement a scaffold in an alveolar bone defect successfully. The present challenge at the meta-analytical level calls for an interdisciplinary approach (Figure 12). Each step of the design process necessitates verifying and evaluating correlation relationships to ensure the scaffold meets the required standards and proves safe and effective for final clinical applications.

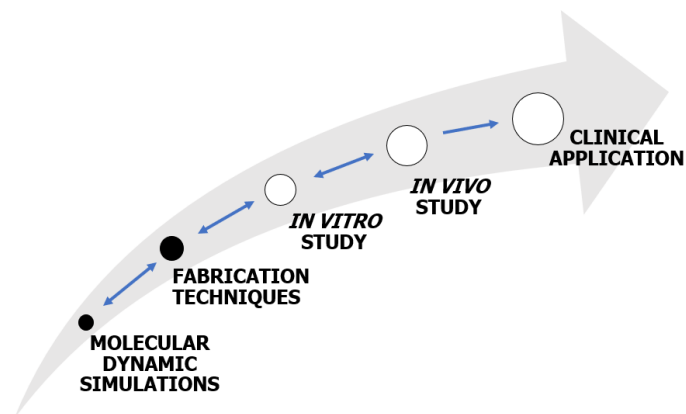


Figure 12. Diagram presenting the pathways from fundamental principles to clinical applications. Each phase of the methodology is predicated on a structured analytical procedure, which entails the decomposition of multifaceted issues into more manageable constituent elements. This is followed by a synthesis procedure, which involves a methodical progression from elementary subjects and phenomena to those of greater complexity. Finally, an enumeration procedure is employed, necessitating a thorough and systematic review to ascertain that all facets of the problem under investigation have been duly considered.

Currently, the prevailing trend in designing precise augmentation of alveolar bone defects involves fabricating scaffolds using 3D printing. The ideal pore size and interconnectivity for cell migration, nutrient transport, and vascularisation have yet to be standardised. Moreover, integrating mechanotransduction and cell signals into 3D-printed scaffolds to guide and stimulate bone growth still needs to be explored. The standardisation of mechanical properties is also a subject of debate. Additionally, while most studies initially focus on mechanical properties, the long-term performance of scaffolds in vitro and in vivo, as degradation progresses, remains to be investigated.

Further research is required to determine how to maintain structural and mechanical integrity. Moreover, surface modifications of the scaffold play a pivotal role. A burgeoning area of research involves introducing HA/CS composites into the PCL matrix or depositing CGI onto the surface of the PCL scaffold.

Despite current research gaps, the potential of 3D-printed PCL-based scaffolds reinforced with HA, CGI, and CS for BTE is significant. The design of the scaffolds' structural, mechanical, degradation, and surface properties could promote osteoblast adhesion, proliferation, and differentiation. These are crucial mechanisms for successful bone regeneration, especially in the case of the alveolar bone, which is sensitive to disturbances in homeostasis. Future research to resolve the discussed limitations will facilitate the development of new concepts and research procedures in BTE.

Author Contributions: Writing—original draft preparation, K.S.; Writing—review and editing, K.S., P.Ś. and M.P.; Visualization, K.S.; Supervision, P.Ś. and M.P.; Project administration, M.P.; Funding acquisition, M.P. All authors have read and agreed to the published version of the manuscript.

Funding: This article was funded by The National Centre for Research and Development, Poland: LIDER/42/0149/L-9/17/NCBR/2018.

Institutional Review Board Statement: Not applicable.

Informed Consent Statement: Not applicable.

Data Availability Statement: No new data were created.

Conflicts of Interest: The authors declare no conflict of interest.

References

- Cho, H.J.; Jeon, J.Y.; Ahn, S.J.; Lee, S.W.; Chung, J.R.; Park, C.J.; Hwang, K.G. The preliminary study for three-dimensional alveolar bone morphologic characteristics for alveolar bone restoration. *Maxillofac. Plast. Reconstr. Surg.* **2019**, *41*, 2–8. [[CrossRef](#)] [[PubMed](#)]
- Lin, W.; Li, Q.; Zhang, D.; Zhang, X.; Qi, X.; Wang, Q.; Chen, Y.; Liu, C.; Li, H.; Zhang, S.; et al. Mapping the immune microenvironment for mandibular alveolar bone homeostasis at single-cell resolution. *Bone Res.* **2021**, *9*, 17. [[CrossRef](#)] [[PubMed](#)]
- Sakkas, A.; Wilde, F.; Heufelder, M.; Winter, K.; Schramm, A. Autogenous bone grafts in oral implantology—Is it still a “gold standard”? A consecutive review of 279 patients with 456 clinical procedures. *Int. J. Implant Dent.* **2017**, *3*, 23. [[CrossRef](#)]
- Park, S.A.; Lee, H.-J.; Kim, K.-S.; Lee, S.J.; Lee, J.-T.; Kim, S.-Y.; Chang, N.-H.; Park, S.-Y. In Vivo Evaluation of 3D-Printed Polycaprolactone Scaffold Implantation Combined with β -TCP Powder for Alveolar Bone Augmentation in a Beagle Defect Model. *Materials* **2018**, *11*, 238. [[CrossRef](#)] [[PubMed](#)]
- Zhou, Y.; Liu, K.; Zhang, H. Biomimetic Mineralization: From Microscopic to Macroscopic Materials and Their Biomedical Applications. *ACS Appl. Bio Mater.* **2023**, *6*, 3516–3531. [[CrossRef](#)] [[PubMed](#)]
- Omi, M.; Mishina, Y. Roles of osteoclasts in alveolar bone remodeling. *Genes. J. Genet. Dev.* **2022**, *60*, e23490. [[CrossRef](#)]
- Guo, R.; Liwen, Z.; Menglong, H.; Huang, Y.; Weiran, L. Alveolar bone changes in maxillary and mandibular anterior teeth during orthodontic treatment: A systematic review and meta-analysis. *Orthod. Craniofac. Res.* **2021**, *24*, 165–179. [[CrossRef](#)]
- Lin, S.; Li, X.; Liu, H.; Wu, F.; Yang, L.; Su, Y.; Li, J.; Duan, S. Clinical applications of concentrated growth factors combined with bone substitutes for alveolar ridge preservation in maxillary molar area: A randomized controlled trial. *Int. J. Implant Dent.* **2021**, *7*, 115. [[CrossRef](#)]
- Holly, D.; Klein, M.; Mazreku, M.; Zamborsk, R.; Polak, Š.; Danišovič, L. Stem Cells and Their DerivativesImplications for Alveolar Bone Regeneration: A Comprehensive Review. *Int. J. Mol. Sci.* **2021**, *22*, 11746. [[CrossRef](#)]
- Liu, N.; Zhang, X.; Guo, Q.; Wu, T.; Wang, Y. 3D Bioprinted Scaffolds for Tissue Repair and Regeneration. *Front. Mater.* **2022**, *9*, 925321. [[CrossRef](#)]
- Tejo-Otero, A.; Buj-Corral, I.; Fenollosa-Artes, F. 3D Printing in Medicine for Preoperative Surgical Planning: A Review. *Ann. Biomed. Eng.* **2020**, *48*, 536–555. [[CrossRef](#)] [[PubMed](#)]
- Tojeira, A.; Biscaia, S.S.; Viana, T.Q.; Sousa, I.S.; Mitchell, G.R. Controlling Morphology in 3D Printing. In *Controlling the Morphology of Polymers: Multiple Scales of Structure and Processing*; Springer: Cham, Switzerland, 2016; pp. 181–207, ISBN 9783319393223.
- Haleem, A.; Javaid, M.; Hasan, R.; Suman, R. 3D printing applications in bone tissue engineering. *J. Clin. Orthop. Trauma* **2020**, *11*, S118–S124. [[CrossRef](#)] [[PubMed](#)]
- Pitjamit, S.; Thunsiri, K.; Nakkiew, W.; Wongwichai, T.; Pothacharoen, P.; Wattanutchariya, W. The Possibility of Interlocking Nail Fabrication from FFF 3D Printing PLA/PCL/HA Composites Coated by Local Silk Fibroin for Canine Bone Fracture Treatment. *Materials* **2020**, *13*, 1564. [[CrossRef](#)] [[PubMed](#)]
- Kim, C.G.; Han, K.S.; Lee, S.; Kim, M.C.; Kim, S.Y.; Nah, J. Fabrication of Biocompatible Polycaprolactone—Hydroxyapatite Composite Filaments for the FDM 3D Printing of Bone Scaffolds. *Appl. Sci.* **2021**, *11*, 6351. [[CrossRef](#)]
- Wang, F.; Tankus, E.B.; Santarella, F.; Rohr, N.; Sharma, N.; Märtin, S.; Michalscheck, M.; Maintz, M.; Cao, S.; Thieringer, F.M. Fabrication and Characterization of PCL/HA Filament as a 3D Printing Material Using Thermal Extrusion Technology for Bone Tissue Engineering. *Polymers* **2022**, *14*, 669. [[CrossRef](#)] [[PubMed](#)]
- Liao, H.; Lee, M.; Tsai, W.; Wang, H.; Lu, W. Osteogenesis of adipose-derived stem cells on polycaprolactone— β -tricalcium phosphate scaffold fabricated via selective laser sintering and surface coating with collagen type I. *J. Tissue Eng. Regen. Med.* **2016**, *10*, 337–353. [[CrossRef](#)] [[PubMed](#)]
- Janmohammadi, M.; Nourbakhsh, M.S.; Bahraminasab, M.; Tayebi, L. Effect of Pore Characteristics and Alkali Treatment on the Physicochemical and Biological Properties of a 3D-Printed Polycaprolactone Bone Scaffold. *ACS Omega* **2023**, *8*, 7378–7394. [[CrossRef](#)]
- Lin, Y.M.; Chen, H.; Lin, C.H.; Huang, P.J.; Lee, S.Y. Development of polycaprolactone/hydroxyapatite composite resin for 405 nm digital light projection 3D printing. *Rapid Prototyp. J.* **2020**, *26*, 951–958. [[CrossRef](#)]
- Joseph, B.; James, J.; Grohens, Y.; Kalarikkal, N.; Thomas, S. Additive Manufacturing of Poly (ϵ -Caprolactone) for Tissue Engineering. *JOM* **2020**, *72*, 4127–4138. [[CrossRef](#)]
- Freeman, F.E.; Pitacco, P.; Van Dommelen, L.H.A.; Nulty, J.; Browe, D.C.; Shin, J.; Alsberg, E.; Kelly, D.J. 3D bioprinting spatiotemporally defined patterns of growth factors to tightly control tissue regeneration. *Sci. Adv.* **2020**, *6*, eabb5093. [[CrossRef](#)]
- Rezania, N.; Asadi-Eydivand, M.; Abolfathi, N.; Bonakdar, S.; Mehrjoo, M.; Solati-Hashjin, M. Three-dimensional printing of polycaprolactone/hydroxyapatite bone tissue engineering scaffolds mechanical properties and biological behavior. *J. Mater. Sci. Mater. Med.* **2022**, *33*, 31. [[CrossRef](#)] [[PubMed](#)]
- Bayart, M.; Dubus, M.; Charlon, S.; Kerdjoudj, H.; Baleine, N.; Benali, S.; Raquez, J.M.; Soulestin, J. Pellet-Based Fused Filament Fabrication (FFF)-Derived Process for the Development of Polylactic Acid/Hydroxyapatite Scaffolds Dedicated to Bone Regeneration. *Materials* **2022**, *15*, 5615. [[CrossRef](#)] [[PubMed](#)]

24. Åkerlund, E.; Diez-Escudero, A.; Grzeszczak, A.; Persson, C. The Effect of PCL Addition on 3D-Printable PLA/HA Composite Filaments for the Treatment of Bone Defects. *Polymers* **2022**, *14*, 3305. [[CrossRef](#)] [[PubMed](#)]
25. Carvalho, M.S.; Cabral, J.M.S. Bone Matrix Non-Collagenous Proteins in Tissue Engineering: Creating New Bone by Mimicking the Extracellular Matrix. *Polymers* **2021**, *13*, 1095. [[CrossRef](#)]
26. Hutmacher, D.W.; Schantz, T.; Zein, I.; Ng, K.W.; Teoh, S.H.; Tan, K.C. Mechanical properties and cell cultural response of polycaprolactone scaffolds designed and fabricated via fused deposition modeling. *J. Biomed. Mater. Res.* **2001**, *55*, 203–216. [[CrossRef](#)] [[PubMed](#)]
27. Yu, N.; Nguyen, T.; Cho, Y.D.; Kavanagh, N.M.; Ghassib, I.; Giannobile, W.V. Personalized scaffolding technologies for alveolar bone regenerative medicine. *Orthod. Craniofac. Res.* **2019**, *22*, 69–75. [[CrossRef](#)]
28. Dwivedi, R.; Kumar, S.; Pandey, R.; Mahajan, A.; Nandana, D.; Katti, D.S.; Mehrotra, D. Journal of Oral Biology and Craniofacial Research Polycaprolactone as biomaterial for bone scaffolds: Review of literature. *J. Oral Biol. Craniofac. Res.* **2020**, *10*, 381–388. [[CrossRef](#)]
29. Antheunis, H.; Van Der Meer, J.C.; De Geus, M.; Heise, A.; Koning, C.E. Autocatalytic equation describing the change in molecular weight during hydrolytic degradation of aliphatic polyesters. *Biomacromolecules* **2010**, *11*, 1118–1124. [[CrossRef](#)]
30. Yeo, T.; Ko, Y.G.; Kim, E.J.; Kwon, O.K.; Chung, H.Y.; Kwon, O.H. Promoting bone regeneration by 3D-printed poly(glycolic acid)/hydroxyapatite composite scaffolds. *J. Ind. Eng. Chem.* **2021**, *94*, 343–351. [[CrossRef](#)]
31. Mondal, S.; Nguyen, T.P.; Pham, V.H.; Hoang, G.; Manivasagan, P.; Kim, M.H.; Nam, S.Y.; Oh, J. Hydroxyapatite nano bioceramics optimized 3D printed poly lactic acid scaffold for bone tissue engineering application. *Ceram. Int.* **2020**, *46*, 3443–3455. [[CrossRef](#)]
32. Sung, H.J.; Meredith, C.; Johnson, C.; Galis, Z.S. The effect of scaffold degradation rate on three-dimensional cell growth and angiogenesis. *Biomaterials* **2004**, *25*, 5735–5742. [[CrossRef](#)]
33. Murphy, S.H.; Leeke, G.A.; Jenkins, M.J. A Comparison of the use of FTIR spectroscopy with DSC in the characterisation of melting and crystallisation in polycaprolactone. *J. Therm. Anal. Calorim.* **2012**, *107*, 669–674. [[CrossRef](#)]
34. Daskalakis, E.; Hassan, M.H.; Omar, A.M.; Acar, A.A.; Fallah, A.; Cooper, G.; Weightman, A.; Blunn, G.; Koc, B.; Bartolo, P. Accelerated Degradation of Poly- ϵ -caprolactone Composite Scaffolds for Large Bone Defects. *Polymers* **2023**, *15*, 670. [[CrossRef](#)]
35. Li, M.; Jia, W.; Zhang, X.; Weng, H.; Gu, G.; Chen, Z. Hyaluronic acid oligosaccharides modified mineralized collagen and chitosan with enhanced osteoinductive properties for bone tissue engineering. *Carbohydr. Polym.* **2021**, *260*, 117780. [[CrossRef](#)] [[PubMed](#)]
36. Ghayor, C.; Bhattacharya, I.; Weber, F.E. The optimal microarchitecture of 3D-printed β -TCP bone substitutes for vertical bone augmentation differs from that for osteoconduction. *Mater. Des.* **2021**, *204*, 109650. [[CrossRef](#)]
37. Chen, L.; Hu, J.; Ran, J.; Shen, X.; Tong, H. Synthesis and Cytocompatibility of Collagen/Hydroxyapatite Nanocomposite Scaffold for Bone Tissue Engineering. *Polym. Compos.* **2014**, *37*, 81–90. [[CrossRef](#)]
38. Alkhursani, S.A.; Ghobashy, M.M.; Al-qahtany, S.A.; Meganid, A.S.; El-halim, S.M.A.; Ahmad, Z.; Khan, F.S.; Abdel, G.; Atia, N.; Cavalu, S. Application of Nano-Inspired Scaffolds-Based Biopolymer Hydrogel for Bone and Periodontal Tissue Regeneration. *Polymers* **2022**, *14*, 3791. [[CrossRef](#)]
39. Neves, M.I.; Ara, M.; Moroni, L.; Silva, R.M.P.; Barrias, C.C. Glycosaminoglycan-Inspired Biomaterials for the Development of Bioactive Hydrogel Networks. *Molecules* **2020**, *25*, 978. [[CrossRef](#)]
40. Islam, M.M.; Shahruzzaman, M.; Biswas, S.; Nurus Sakib, M.; Rashid, T.U. Chitosan based bioactive materials in tissue engineering applications—A review. *Bioact. Mater.* **2020**, *5*, 164–183. [[CrossRef](#)]
41. Hu, Y.; Chen, J.; Fan, T.; Zhang, Y.; Zhao, Y.; Shi, X.; Zhang, Q. Biomimetic mineralized hierarchical hybrid scaffolds based on in situ synthesis of nano-hydroxyapatite/chitosan/chondroitin sulfate/hyaluronic acid for bone tissue engineering. *Colloids Surf. B Biointerfaces* **2017**, *157*, 93–100. [[CrossRef](#)]
42. Deshpande, R.; Shukla, S.; Sayyad, R.; Salunke, S.; Nisal, A.; Venugopalan, P. Silk fibroin and ceramic scaffolds: Comparative in vitro studies for bone regeneration. *Bioeng. Transl. Med.* **2021**, *6*, e10221. [[CrossRef](#)] [[PubMed](#)]
43. Vázquez, J.A.; Rodriguez-Amado, I.; Montemayor, M.I.; Fraguas, J.; González, M.D.P.; Murado, M.A. Chondroitin Sulfate, Hyaluronic Acid and Chitin/Chitosan Production Using Marine Waste Sources: Characteristics, Applications and Eco-Friendly Processes: A Review. *Mar. Drugs* **2013**, *11*, 747–774. [[CrossRef](#)] [[PubMed](#)]
44. Swanson, T.E.; Cheng, X.; Friedrich, C. Development of chitosan—Vancomycin antimicrobial coatings on titanium implants. *J. Biomed. Mater. Res. Part A* **2011**, *97A*, 167–176. [[CrossRef](#)] [[PubMed](#)]
45. Yu, H.; Xia, L.; Leng, X.; Chen, Y.; Zhang, L.; Ni, X.; Luo, J.; Leng, W. Improved repair of rabbit calvarial defects with hydroxyapatite/chitosan/polycaprolactone composite scaffold-engrafted EPCs and BMSCs. *Front. Bioeng. Biotechnol.* **2022**, *10*, 928041. [[CrossRef](#)]
46. Hokmabad, V.R.; Davaran, S.; Aghazadeh, M.; Alizadeh, E.; Salehi, R.; Ramazani, A. A Comparison of the Effects of Silica and Hydroxyapatite Nanoparticles on Poly(ϵ -caprolactone)-Poly(ethylene glycol)-Poly(ϵ -caprolactone)/Chitosan Nanofibrous Scaffolds for Bone Tissue Engineering. *Tissue Eng. Regen. Med.* **2018**, *15*, 735–750. [[CrossRef](#)]
47. Ressler, A. Chitosan-Based Biomaterials for Bone Tissue Engineering Applications: A Short Review. *Polymers* **2022**, *14*, 3430. [[CrossRef](#)]
48. Guo, L.; Liang, Z.; Yang, L.; Du, W.; Yu, T.; Tang, H.; Li, C. The role of natural polymers in bone tissue engineering. *J. Control. Release* **2021**, *338*, 571–582. [[CrossRef](#)]

49. Yang, X.; Wang, Y.; Zhou, Y.; Chen, J. The Application of Polycaprolactone in Three-Dimensional Printing Scaffolds for Bone Tissue Engineering. *Polymers* **2021**, *13*, 2754. [[CrossRef](#)]
50. Tsuchida, S.; Nakayama, T. Recent Clinical Treatment and Basic Research on the Alveolar Bone. *Biomedicines* **2023**, *11*, 843. [[CrossRef](#)]
51. Wang, H.; Li, T.; Wang, X.; Guan, Y.; Jiang, Y.; Chen, S.; Zou, S.; Duan, P. Mechanisms of sphingosine-1-phosphate (S1P) signaling on excessive stress-induced root resorption during orthodontic molar intrusion. *Clin. Oral Investig.* **2022**, *26*, 1003–1016. [[CrossRef](#)]
52. Hashimoto, K.; Kaito, T.; Furuya, M.; Seno, S. In vivo dynamic analysis of BMP-2-induced ectopic bone formation. *Sci. Rep.* **2020**, *10*, 4751. [[CrossRef](#)] [[PubMed](#)]
53. Yan, Z.-Q.; Yong, X.-K.W.; Wang, Z.Z.; Wang, Z.; Jin, L.; Yin, H.; Xia, K.; Feng, Y.T.S.; Tang, P.X.S.; Jia, C.F.; et al. H-type blood vessels participate in alveolar bone remodeling during murine tooth extraction healing. *Oral Dis.* **2020**, *26*, 998–1009. [[CrossRef](#)] [[PubMed](#)]
54. Zhang, Q.; Wu, W.; Qian, C.; Xiao, W.; Zhu, H.; Guo, J. Advanced biomaterials for repairing and reconstruction of mandibular defects. *Mater. Sci. Eng. C* **2019**, *103*, 109858. [[CrossRef](#)] [[PubMed](#)]
55. Tanaka, Y.; Nakayamada, S.; Okada, Y. Osteoblasts and osteoclasts in bone remodeling and inflammation. *Curr. Drug Targets Inflamm. Allergy* **2005**, *4*, 325–328. [[CrossRef](#)] [[PubMed](#)]
56. Proff, P.; Römer, P. The molecular mechanism behind bone remodelling: A review. *Clin. Oral Investig.* **2009**, *13*, 355–362. [[CrossRef](#)]
57. Xiong, J.; O'Brien, C.A. Osteocyte RANKL: New Insights into the Control of Bone Remodeling. *J. Bone Miner. Res.* **2012**, *27*, 499–505. [[CrossRef](#)]
58. Bernhard, J.C.; Marolt Presen, D.; Li, M.; Monforte, X.; Ferguson, J.; Leinfellner, G.; Heimel, P.; Betti, S.L.; Shu, S.; Teuschl-Woller, A.H.; et al. Effects of Endochondral and Intramembranous Ossification Pathways on Bone Tissue Formation and Vascularization in Human Tissue-Engineered Grafts. *Cells* **2022**, *11*, 3070. [[CrossRef](#)]
59. Rodrigues, G.; Florencio-Silva, R.; Sasso-Cerri, E.; Paulo, S.; Damas, C.; Jesus, M. De Spatio-temporal immunolocalization of VEGF-A, Runx2, and osterix during the early steps of intramembranous ossification of the alveolar process in rat embryos. *Dev. Biol.* **2021**, *478*, 133–143. [[CrossRef](#)]
60. Mackie, E.J.; Ahmed, Y.A.; Tatarczuch, L.; Chen, K.; Mirams, M. Endochondral ossification: How cartilage is converted into bone in the developing skeleton. *Int. J. Biochem. Cell Biol.* **2008**, *40*, 46–62. [[CrossRef](#)]
61. Isaksson, H.; Wilson, W.; van Donkelaar, C.C.; Huiskes, R.; Ito, K. Comparison of biophysical stimuli for mechano-regulation of tissue differentiation during fracture healing. *J. Biomech.* **2006**, *39*, 1507–1516. [[CrossRef](#)]
62. Shu, H.S.; Liu, Y.L.; Tang, X.T.; Zhang, X.S.; Zhou, B.; Zou, W.; Zhou, B.O.; Shu, H.S.; Liu, Y.L.; Tang, X.T.; et al. Tracing the skeletal progenitor transition during postnatal bone formation. *Cell Stem Cell* **2021**, *28*, 2122–2136.e3. [[CrossRef](#)] [[PubMed](#)]
63. Chan, W.C.W.; Tan, Z.; To, M.K.T.; Chan, D. Regulation and Role of Transcription Factors in Osteogenesis. *Int. J. Mol. Sci.* **2021**, *22*, 5445. [[CrossRef](#)] [[PubMed](#)]
64. Xu, X.; Liu, S.; Liu, H.; Ru, K.; Jia, Y.; Wu, Z. Piezo Channels: Awesome Mechanosensitive Structures in Cellular Mechanotransduction and Their Role in Bone. *Int. J. Mol. Sci.* **2021**, *22*, 6429. [[CrossRef](#)] [[PubMed](#)]
65. Foley, B.; Selmane, M.; Mezzetti, A.; Lefebvre, C.; El Kirat, K.; Landoulsi, J. Tunable Enzyme-Assisted Mineralization of Apatitic Calcium Phosphate by Homogeneous Catalysis. *Int. J. Mol. Sci.* **2023**, *24*, 43. [[CrossRef](#)]
66. Dorozhkin, S.V.; Epple, M. Biological and Medical Significance of Calcium Phosphates. *Angew. Chemie Int. Ed.* **2002**, *41*, 3130–3146. [[CrossRef](#)]
67. Dong, L.; Wang, S.-J.; Zhao, X.-R.; Zhu, Y.-F.; Yu, J.-K. 3D-Printed Poly(ϵ -caprolactone) Scaffold Integrated with Cell-laden Chitosan Hydrogels for Bone Tissue Engineering. *Sci. Rep.* **2017**, *7*, 13412. [[CrossRef](#)]
68. Cai, X.; Tong, H.; Shen, X.; Chen, W.; Yan, J.; Hu, J. Preparation and characterization of homogeneous chitosan—Polylactic acid/hydroxyapatite nanocomposite for bone tissue engineering and evaluation of its mechanical properties. *Acta Biomater.* **2009**, *5*, 2693–2703. [[CrossRef](#)]
69. Kunitomi, Y.; Hara, E.S.; Okada, M.; Nagaoka, N.; Kuboki, T.; Nakano, T.; Kamioka, H.; Matsumoto, T. Biomimetic mineralization using matrix vesicle nanofragments. *J. Biomed. Mater. Res. Part A* **2019**, *107A*, 1021–1030. [[CrossRef](#)]
70. Moradian-Oldak, J.; George, A. Biominerization of Enamel and Dentin Mediated by Matrix Proteins. *J. Dent. Res.* **2021**, *100*, 1020–1029. [[CrossRef](#)]
71. Bozycki, L.; Mroczek, J.; Bessueille, L.; Mebarek, S.; Buchet, R.; Pikula, S.; Strzelecka-Kiliszek, A. Annexins A2, A6 and Fetuin—A Affect the Process of Mineralization in Vesicles Derived from Human Osteoblastic. *Int. J. Mol. Sci.* **2021**, *22*, 3993. [[CrossRef](#)]
72. Anderson, H.C. Matrix Vesicles and Calcification. *Curr. Rheumatol. Rep.* **2017**, *5*, 222–226. [[CrossRef](#)] [[PubMed](#)]
73. Hasegawa, T. Ultrastructure and biological function of matrix vesicles in bone mineralization. *Histochem. Cell Biol.* **2018**, *149*, 289–304. [[CrossRef](#)] [[PubMed](#)]
74. Yu, L.; Wei, M. Biominerization of Collagen-Based Materials for Hard Tissue Repair. *Int. J. Mol. Sci.* **2021**, *22*, 944. [[CrossRef](#)]
75. De-Leon, S.B.-T. The Evolution of Biominerization through the Co-Option of Organic Scaffold Forming Networks. *Cells* **2022**, *11*, 595. [[CrossRef](#)] [[PubMed](#)]
76. Thang, L.H.; Bang, L.T.; Long, B.D.; Son, N.A.; Ramesh, S. Effect of Carbonate Contents on the Thermal Stability and Mechanical Properties of Carbonated Apatite Artificial Bone Substitute with Different Carbonate Ion Sources. *J. Mater. Eng. Perform.* **2023**, *32*, 1006–1016. [[CrossRef](#)]

77. Olszta, M.J.; Cheng, X.; Soo, S.; Kumar, R.; Kim, Y.; Kaufman, M.J.; Douglas, E.P.; Gower, L.B. Bone structure and formation: A new perspective. *Mater. Sci. Eng. R* **2007**, *58*, 77–116. [[CrossRef](#)]
78. Le Cann, S.; Törnquist, E.; Silva, I.; Fraulob, M.; Albini, H.; Verezhak, M.; Guizar-sicairos, M.; Isaksson, H.; Häiat, G. Acta Biomaterialia Spatio-temporal evolution of hydroxyapatite crystal thickness at the bone-implant interface. *Acta Biomater.* **2020**, *116*, 391–399. [[CrossRef](#)]
79. Wang, L.; Ciani, C.; Doty, S.B.; Fritton, S.P. Delineating bone's interstitial fluid pathway in vivo. *Bone* **2004**, *34*, 499–509. [[CrossRef](#)]
80. Lin, X.; Patil, S.; Gao, Y.; Qian, A. The Bone Extracellular Matrix in Bone Formation and Regeneration. *Front. Pharmacol.* **2020**, *11*, 757. [[CrossRef](#)]
81. Best, S.M.; Duer, M.J.; Reid, D.G.; Wise, R. Towards a model of the mineral—Organic interface in bone: NMR of the structure of synthetic glycosaminoglycan- and polyaspartate-calcium phosphate composites. *Magn. Reson. Chem.* **2008**, *46*, 323–329. [[CrossRef](#)]
82. Kaczmarek, B.; Sionkowska, A. Influence of glycosaminoglycans on the properties of thin films based on chitosan/collagen blends. *J. Mech. Behav. Biomed. Mater.* **2018**, *80*, 189–193. [[CrossRef](#)] [[PubMed](#)]
83. Menezes, R.; Vincent, R.; Osorno, L.; Hu, P.; Livingston, T. Biomaterials and tissue engineering approaches using glycosaminoglycans for tissue repair: Lessons learned from the native extracellular matrix. *Acta Biomater.* **2023**, *163*, 210–227. [[CrossRef](#)] [[PubMed](#)]
84. Wojtas, M.; Lausch, A.J.; Sone, E.D. Glycosaminoglycans accelerate biomimetic collagen mineralization in a tissue-based in vitro model. *Proc. Natl. Acad. Sci. USA* **2020**, *117*, 12636–12642. [[CrossRef](#)]
85. Hua, R.; Ni, Q.; Eliason, T.D.; Han, Y.; Gu, S. Biglycan and chondroitin sulfate play pivotal roles in bone toughness via retaining bound water in bone mineral matrix. *Matrix Biol.* **2020**, *94*, 95–109. [[CrossRef](#)] [[PubMed](#)]
86. Melbouci, M.; Mason, R.W.; Suzuki, Y.; Fukao, T.; Orii, T.; Tomatsu, S. Review: Growth Impairment in Mucopolysaccharidoses. *Mol. Genet. Metab.* **2018**, *124*, 1–10. [[CrossRef](#)] [[PubMed](#)]
87. Nakamura-utsunomiya, A. Bone Biomarkers in Mucopolysaccharidoses. *Int. J. Mol. Sci.* **2021**, *22*, 12651. [[CrossRef](#)] [[PubMed](#)]
88. Wang, W.; Wang, A.; Hu, G.; Bian, M.; Chen, L.; Zhao, Q.; Sun, W.; Wu, Y. Potential of an Aligned Porous Hydrogel Scaffold Combined with Periodontal Ligament Stem Cells or Gingival Mesenchymal Stem Cells to Promote Tissue Regeneration in Rat Periodontal Defects. *ACS Biomater. Sci. Eng.* **2023**, *9*, 1961–1975. [[CrossRef](#)]
89. Waddington, R.J.; Embrey, G.; Last, K. Glycosaminoglycans of human alveolar bone. *Archs Oral Biol.* **1989**, *34*, 587–589. [[CrossRef](#)]
90. He, H.; Shao, C.; Mu, Z.; Mao, C.; Sun, J.; Chen, C.; Tang, R.; Gu, X. Promotion effect of immobilized chondroitin sulfate on intrafibrillar mineralization of collagen. *Carbohydr. Polym.* **2020**, *229*, 115547. [[CrossRef](#)]
91. Hao, J.; Wan, Q.; Mu, Z.; Gu, J.; Yu, W.; Qin, W.; Li, Y.; Wang, C.; Ma, Y.; Jiao, K.; et al. A seminal perspective on the role of chondroitin sulfate in biomineralization. *Carbohydr. Polym.* **2023**, *310*, 120738. [[CrossRef](#)]
92. Tatara, Y.; Suto, S.; Itoh, K. Novel roles of glycosaminoglycans in the degradation of type I collagen by cathepsin K. *Glycobiology* **2017**, *27*, 1089–1098. [[CrossRef](#)] [[PubMed](#)]
93. Buckley, M.R.; Evans, E.B.; Matuszewski, P.E.; Chen, Y.; Satchel, L.N.; Elliott, D.M.; Soslowsky, L.J.; Dodge, G.R. Distributions of types I, II and III collagen by region in the human supraspinatus supraspinatus tendon. *Connect. Tissue Res.* **2013**, *54*, 374–379. [[CrossRef](#)] [[PubMed](#)]
94. Sorvina, A.; Antoniou, M.; Esmaeili, Z.; Kochetkova, M. Unusual Suspects: Bone and Cartilage ECM Proteins as Carcinoma Facilitators. *Cancers* **2023**, *15*, 791. [[CrossRef](#)]
95. Holwerda, A.M.; van Loon, L.J.C. The impact of collagen protein ingestion on musculoskeletal connective tissue remodeling: A narrative review. *Nutr. Rev.* **2021**, *80*, 1497–1514. [[CrossRef](#)] [[PubMed](#)]
96. Liu, M.M.; Li, W.T.; Xia, X.M.; Wang, F.; Macdougall, M.; Chen, S. Dentine Sialophosphoprotein Signal in Dentineogenesis and Dentine Regeneration. *Eur. Cell Mater.* **2021**, *42*, 43–62. [[CrossRef](#)]
97. Yang, H.; Fan, Z. The functional extracellular matrix on the regulation of odontogenic differentiation of stem cells. *Curr. Med.* **2022**, *1*, 10. [[CrossRef](#)]
98. Combes, C.; Cazalbou, S.; Rey, C. Apatite Biominerals. *Minerals* **2016**, *6*, 34. [[CrossRef](#)]
99. Lawrence, L.M.; Salary, R.R.; Miller, V.; Valluri, A.; Denning, K.L.; Case-perry, S.; Abdelgaber, K.; Smith, S.; Claudio, P.P.; Day, J.B. Osteoregenerative Potential of 3D-Printed Poly ϵ -Caprolactone Tissue Scaffolds In Vitro Using Minimally Manipulative Expansion of Primary Human Bone Marrow Stem Cells. *Int. J. Mol. Sci.* **2023**, *24*, 4940. [[CrossRef](#)]
100. Moghaddaszadeh, A.; Seddiqi, H.; Najmoddin, N.; Ravasjani, S.A.; Klein-Nulend, J. Biomimetic 3D-printed PCL scaffold containing a high concentration carbonated-nanohydroxyapatite with immobilized-collagen for bone tissue engineering: Enhanced bioactivity and physicomechanical characteristics. *Biomed. Mater.* **2021**, *16*, 65029. [[CrossRef](#)]
101. Yadav, N.; Mudgal, D.; Anand, R.; Jindal, S.; Mishra, V. Recent development in nanoencapsulation and delivery of natural bioactives through chitosan scaffolds for various biological applications. *Int. J. Biol. Macromol.* **2022**, *220*, 537–572. [[CrossRef](#)]
102. Egorov, A.; Riedel, B.; Vinke, J.; Schmal, H.; Thomann, R.; Thomann, Y.; Seidenstuecker, M. The Mineralization of Various 3D-Printed PCL Composites. *J. Funct. Biomater.* **2022**, *13*, 238. [[CrossRef](#)] [[PubMed](#)]
103. Ebrahimi, Z.; Irani, S.; Ardeshtirajlajimi, A.; Seyedjafari, E. Enhanced osteogenic differentiation of stem cells by 3D printed PCL scaffolds coated with collagen and hydroxyapatite. *Sci. Rep.* **2022**, *12*, 12359. [[CrossRef](#)] [[PubMed](#)]
104. Daculsi, G.; Fellah, B.H.; Miramond, T.; Durand, M. Osteoconduction, Osteogenicity, Osteoinduction, what are the fundamental properties for a smart bone substitutes. *IRBM* **2013**, *34*, 346–348. [[CrossRef](#)]

105. Gomes-Araújo, N.; Gavilán-Romero, F.; Arnáez-García, I.; Ramos-Martínez, C.; Pérez-Sánchez, A.M. Osseointegration mechanisms: A proteomic approach. *JBIC J. Biol. Inorg. Chem.* **2018**, *23*, 459–470. [[CrossRef](#)]
106. Rather, H.A.; Jhala, D.; Vasita, R. Dual functional approaches for osteogenesis coupled angiogenesis in bone tissue engineering. *Mater. Sci. Eng. C* **2019**, *103*, 109761. [[CrossRef](#)] [[PubMed](#)]
107. Xiao, D.; Zhang, J.; Zhang, C.; Barbieri, D.; Yuan, H.; Moroni, L.; Feng, G. The role of calcium phosphate surface structure in osteogenesis and the mechanisms involved. *Acta Biomater.* **2020**, *106*, 22–33. [[CrossRef](#)]
108. Ghayor, C.; Weber, F.E. Osteoconductive microarchitecture of bone substitutes for bone regeneration revisited. *Front. Physiol.* **2018**, *9*, 960. [[CrossRef](#)]
109. Weber, F.E. Reconsidering Osteoconduction in the Era of Additive Manufacturing. *Tissue Eng. Part B Rev.* **2019**, *25*, 375–386. [[CrossRef](#)]
110. Barrere, F.; van der Valk, C.M.; Dalmeijer, R.A.J.; Meijer, G.; Van Blitterswijk, C.A.; De Groot, K.; Layrolle, P. Osteogenecity of octacalcium phosphate coatings applied on porous metal implants. *J. Biomed. Mater. Res. Part A* **2002**, *66A*, 792–889. [[CrossRef](#)]
111. Yousefiasl, S.; Sharifi, E.; Salahinejad, E.; Makvandi, P.; Irani, S.; Cam, C.A.D. Bioactive 3D-printed chitosan-based scaffolds for personalized craniofacial bone tissue engineering. *Eng. Regen.* **2023**, *4*, 1–11. [[CrossRef](#)]
112. Srividya, S.; Sridevi, G.; Kumar, B.S.; Sastry, T.P. Biocatalysis and Agricultural Biotechnology Fabrication, characterization and osseointegration of bonegraft incorporated with leaf extracts of *Ormoscaprum Sennoides* and biocompatible polymers. *Biocatal. Agric. Biotechnol.* **2018**, *15*, 92–102. [[CrossRef](#)]
113. Chen, X.; Fan, H.; Deng, X.; Wu, L.; Yi, T.; Gu, L.; Zhou, C.; Fan, Y.; Zhang, X. Scaffold Structural Microenvironmental Cues to Guide Tissue Regeneration in Bone Tissue Applications. *Nanomaterials* **2018**, *8*, 960. [[CrossRef](#)] [[PubMed](#)]
114. Ye, H.; Zhu, J.; Deng, D.; Jin, S.; Li, J.; Man, Y. Enhanced osteogenesis and angiogenesis by PCL/chitosan/Sr-doped calcium phosphate electrospun nanocomposite membrane for guided bone regeneration. *J. Biomater. Sci.* **2019**, *30*, 1505–1522. [[CrossRef](#)] [[PubMed](#)]
115. Suzuki, O.; Hamai, R.; Sakai, S. The material design of octacalcium phosphate bone substitute: Increased dissolution and osteogenecity. *Acta Biomater.* **2023**, *158*, 1–11. [[CrossRef](#)] [[PubMed](#)]
116. Shin, S.Y.; Rios, H.F.; Giannobile, W.V.; Oh, T. *Periodontal Regeneration: Current Therapies*; Elsevier Inc.: Amsterdam, The Netherlands, 2015; ISBN 9780123971579.
117. Oryan, A.; Hassanajili, S.; Sahvieh, S. Effectiveness of a biodegradable 3D polylactic acid/poly(ε-caprolactone)/hydroxyapatite scaffold loaded by differentiated osteogenic cells in a critical-sized radius bone defect in rat. *J. Tissue Eng. Regen. Med.* **2021**, *15*, 150–162. [[CrossRef](#)] [[PubMed](#)]
118. Liu, J.; Ruan, J.; Weir, M.D.; Ren, K.; Schneider, A.; Wang, P.; Oates, T.W.; Chang, X.; Xu, H.H.K. Periodontal Bone-Ligament-Cementum Regeneration via Scaffolds and Stem Cells. *Cells* **2019**, *8*, 537. [[CrossRef](#)]
119. Naik, C.; Srinath, N.; Ranganath, M.K.; Umashankar, D.N.; Gupta, H. Evaluation of polycaprolactone scaffold for guided bone regeneration in maxillary and mandibular defects: A clinical study. *Natl. J. Maxillofac. Surg.* **2020**, *11*, 207–212. [[CrossRef](#)]
120. Fan, Y.; Cui, C.; Rosen, C.J.; Sato, T.; Xu, R.; Li, P.; Wei, X.; Bi, R.; Yuan, Q. Klotho in Osx⁺-mesenchymal progenitors exerts pro-osteogenic and anti-inflammatory effects during mandibular alveolar bone formation and repair. *Signal Transduct. Target. Ther.* **2022**, *7*, 155. [[CrossRef](#)]
121. Yoshida, M.; Turner, P.R.; John, C.; Azam, M.; Jaydee, A. A comparison between β-tricalcium phosphate and chitosan poly-caprolactone-based 3D melt extruded composite scaffolds. *Biopolymers* **2022**, *113*, e23482. [[CrossRef](#)]
122. Gerdes, S.; Mostafavi, A.; Ramesh, S.; Memic, A.; Rivero, I.V.; Rao, P.; Tamayol, A. Bone Process–Structure–Quality Relationships of Three-Dimensional Printed Poly(Caprolactone)-Hydroxyapatite Scaffolds. *Tissue Eng. Part A* **2020**, *26*, 279–291. [[CrossRef](#)]
123. Liu, S.; Zheng, Y. Preparation and characterization of a novel polylactic acid/hydroxyapatite composite scaffold with biomimetic micro-nano fibrous porous structure. *J. Mater. Sci. Mater. Med.* **2020**, *31*, 74. [[CrossRef](#)] [[PubMed](#)]
124. Banimohamad-shotorbani, B.; Rahmani, A.; Bakhtshayesh, D.; Mehdiyoun, A.; Jarolmasjed, S.; Shafaei, H. The efficiency of PCL/HAp electrospun nanofibers in bone regeneration: A review. *J. Med. Eng. Technol.* **2021**, *45*, 511–531. [[CrossRef](#)] [[PubMed](#)]
125. Raheem, A.A.; Hameed, P.; Whenish, R.; Elsen, R.S.; Aswin, G.; Jaiswal, A.K.; Prashanth, K.G.; Manivasagam, G. A review on development of bio-inspired implants using 3d printing. *Biomimetics* **2021**, *6*, 65. [[CrossRef](#)]
126. Hong, J.K.; Cooke, S.L.; Whittington, A.R.; Roman, M. Bioactive Cellulose Nanocomposites for Bone Tissue Engineering Applications. *Front. Bioeng. Biotechnol.* **2021**, *9*, 605924. [[CrossRef](#)] [[PubMed](#)]
127. Malikmammadov, E.; Tanir, T.E.; Kiziltay, A.; Hasirci, V. *PCL and PCL-Based Materials in Biomedical Applications*; Taylor & Francis: Abingdon, UK, 2017; Volume 11, ISBN 9031221031.
128. Kumar, A.; Mohammad, S.; Ibrahim, M.; Agrim, A.; Anwar, A.; Leon, C.H.; Terracciano, A.; Zhao, X.; Su, T.; Kalyon, D.M. Load-bearing biodegradable PCL-PGA-beta TCP scaffolds for bone tissue regeneration. *J. Biomed. Mater. Res.* **2021**, *109*, 193–200. [[CrossRef](#)]
129. Bruyas, A.; Lou, F.; Stahl, A.M.; Gardner, M.; Maloney, W.; Goodman, S.; Yang, Y.P. Systematic characterization of 3D-printed PCL/β-TCP scaffolds for biomedical devices and bone tissue engineering: Influence of composition and porosity. *J. Mater. Res.* **2018**, *33*, 1948–1959. [[CrossRef](#)]
130. Wang, W.; Caetano, G.; Ambler, W.S.; Blaker, J.J.; Fraide, M.A.; Mandal, P.; Diver, C.; Bártolo, P. Enhancing the Hydrophilicity and Cell Attachment of 3D Printed PCL/Graphene Scaffolds for Bone Tissue Engineering. *Materials* **2016**, *9*, 992. [[CrossRef](#)]

131. Radhakrishnan, S.; Nagarajan, S.; Belaid, H.; Farha, C.; Iatsunskyi, I.; Coy, E.; Soussan, L.; Huon, V.; Bares, J.; Belkacemi, K.; et al. Fabrication of 3D printed antimicrobial polycaprolactone scaffolds for tissue engineering applications. *Mater. Sci. Eng. C* **2021**, *118*, 111525. [[CrossRef](#)]
132. Zimmerling, A.; Yazdanpanah, Z.; Cooper, D.M.L.; Johnston, J.D.; Chen, X. 3D printing PCL/nHA bone scaffolds: Exploring the influence of material synthesis techniques. *Biomater. Res.* **2021**, *25*, 3. [[CrossRef](#)]
133. López-Castejón, M.L.; Reviriego, M.L.; Álvarez-Castillo, E.; Aguilar, J.M.; Bengoechea, C. Eco-Composites from Silkworm Meal and Polycaprolactone: Effect of Formulation and Processing Conditions. *Polymers* **2022**, *14*, 2342. [[CrossRef](#)]
134. Fairag, R.; Li, L.; Ramirez-GarcialunaLuna, J.L.; Taylor, M.S.; Gaerke, B.; Weber, M.H.; Rosenzweig, D.H.; Haglund, L. A Composite Lactide-Mineral 3D-Printed Scaffold for Bone Repair and Regeneration. *Front. Cell Dev. Biol.* **2021**, *9*, 654518. [[CrossRef](#)] [[PubMed](#)]
135. Averianov, I.; Stepanova, M.; Solomakha, O.; Gofman, I.; Serdobintsev, M.; Blum, N.; Kaftuirev, A.; Baulin, I.; Nashchekina, J.; Lavrentieva, A.; et al. 3D-Printed composite scaffolds based on poly(ϵ -caprolactone) filled with poly(glutamic acid)-modified cellulose nanocrystals for improved bone tissue regeneration. *J. Biomed. Research* **2022**, *110*, 2422–2437. [[CrossRef](#)] [[PubMed](#)]
136. Krobot, Š.; Melcová, V.; Mencík, P.; Kontárová, S.; Rampichová, M.; Hedvíčáková, V.; Mojžišová, E.; Baco, A.; Prikryl, R. Based Blends for Tissue Engineering and Bone Medical Applications Processed by FDM 3D Printing. *Polymers* **2023**, *15*, 2404. [[CrossRef](#)] [[PubMed](#)]
137. Mancuso, E.; Shah, L.; Jindal, S.; Serenelli, C.; Michail, Z.; Khanbareh, H.; Tirella, A. Materials Science & Engineering C Additively manufactured BaTiO₃ composite scaffolds: A novel strategy for load bearing bone tissue engineering applications. *Mater. Sci. Eng. C* **2021**, *126*, 112192. [[CrossRef](#)]
138. Kao, C.-Y.; Lin, Y.-T.-L.; Lin, Y.-H.; Lee, A.K.-X.; Ng, S.Y.; Huang, T.-H.; Hsu, T.-T. Synergistic Effect of Static Magnetic Fields and 3D-Printed Iron-Oxide-Nanoparticle-Containing Calcium Silicate/Poly- ϵ -Caprolactone Scaffolds for Bone Tissue Engineering. *Cells* **2022**, *11*, 3967. [[CrossRef](#)]
139. Cao, C.; Huang, P.; Prasopthum, A.; Parsons, A.J.; Ai, F.; Yang, J. Characterisation of bone regeneration in 3D printed ductile PCL/PEG/hydroxyapatite scaffolds with high ceramic microparticle concentrations. *Biomater. Sci.* **2022**, *10*, 138–152. [[CrossRef](#)]
140. Christen, M.; Vercesi, F. Polycaprolactone: How a Well-Known and Futuristic Polymer Has Become an Innovative Collagen-Stimulator in Esthetics. *Clin. Cosmet. Investig. Dermatol. ISSN* **2022**, *13*, 31–48. [[CrossRef](#)]
141. She, Y.; Fan, Z.; Wang, L.; Li, Y.; Sun, W.; Tang, H.; Zhang, L. 3D Printed Biomimetic PCL Scaffold as Framework Interspersed With Collagen for Long Segment Tracheal Replacement. *Front. Cell Dev. Biol.* **2021**, *9*, 629796. [[CrossRef](#)]
142. Kim, S.; Heo, S.; Oh, G.; Yi, M. A 3D-Printed Polycaprolactone/Marine Collagen Scaffold Reinforced with Carbonated Hydroxyapatite from Fish Bones for Bone Regeneration. *Mar. Drugs* **2022**, *20*, 344. [[CrossRef](#)]
143. Li, P.; Fu, L.; Liao, Z.; Peng, Y.; Ning, C.; Gao, C. Biomaterials containing synovial mesenchymal stem cells for cartilage regeneration based on tetrahedral framework nucleic acid recruitment. *Biomaterials* **2021**, *278*, 121131. [[CrossRef](#)]
144. Yang, Y.; Wu, H.; Fu, Q.; Xie, X.; Song, Y.; Xu, M.; Li, J. Materials & Design 3D-printed polycaprolactone-chitosan based drug delivery implants for personalized administration. *Mater. Des.* **2022**, *214*, 110394. [[CrossRef](#)]
145. Shirzaei Sani, I.; Rezaei, M.; Baradar Khoshfetrat, A.; Razzaghi, D. Preparation and characterization of polycaprolactone/chitosan-g-polycaprolactone/hydroxyapatite electrospun nanocomposite scaffolds for bone tissue engineering. *Int. J. Biol. Macromol.* **2021**, *182*, 1638–1649. [[CrossRef](#)] [[PubMed](#)]
146. Ressler, A.; Bauer, L.; Prebeg, T.; Ledinski, M.; Hussainova, I.; Urli, I. PCL/Si-Doped Multi-Phase Calcium Phosphate Scaffolds Derived from Cuttlefish Bone. *Materials* **2022**, *15*, 3348. [[CrossRef](#)] [[PubMed](#)]
147. Stulajterova, R.; Medvecky, L. Effect of calcium ions on transformation brushite to hydroxyapatite in aqueous solutions. *Colloids Surf. A Physicochem. Eng. Asp.* **2008**, *316*, 104–109. [[CrossRef](#)]
148. Alghazwani, Y.; Venkatesan, K.; Prabahar, K.; El-sherbiny, M. The Combined Anti-Tumor Efficacy of Bioactive Hydroxyapatite Nanoparticles Loaded with Altretamine. *Pharmaceutics* **2023**, *15*, 302. [[CrossRef](#)]
149. Wang, R.; Liu, W.; Wang, Q.; Li, G.; Wan, B.; Sun, Y.; Niu, X.; Chen, D.; Tian, W. Anti-osteosarcoma effect of hydroxyapatite nanoparticles both in vitro and in vivo by downregulating the FAK/PI3K/Akt signaling pathway. *Biomater. Sci.* **2020**, *8*, 4426–4437. [[CrossRef](#)]
150. Kargozar, S.; Mollazadeh, S.; Kermani, F.; Webster, T.J.; Nazarnezhad, S.; Hamzehlou, S.; Baino, F. Hydroxyapatite Nanoparticles for Improved Cancer Theranostics. *J. Funct. Biomater.* **2022**, *13*, 100. [[CrossRef](#)]
151. Du, M.; Chen, J.; Liu, K.; Xing, H.; Song, C. Recent advances in biomedical engineering of nano-hydroxyapatite including dentistry, cancer treatment and bone repair. *Compos. Part B Eng.* **2021**, *215*, 108790. [[CrossRef](#)]
152. Cestari, F.; Petretta, M.; Yang, Y.; Motta, A.; Grigolo, B.; Sglavo, V.M. 3D printing of PCL/nano-hydroxyapatite scaffolds derived from biogenic sources for bone tissue engineering. *Sustain. Mater. Technol.* **2021**, *29*, e00318. [[CrossRef](#)]
153. Sadat-Shojai, M.; Khorasani, M.; Dinpanah-khoshdargi, E.; Jamshidi, A. Synthesis methods for nanosized hydroxyapatite with diverse structures. *Acta Biomater.* **2013**, *9*, 7591–7621. [[CrossRef](#)]
154. Qi, M.; Huang, Z.; Phakatkar, A.; Yao, W.; Yuan, Y.; Foroozan, T.; Xiao, G.; Shahbazian-Yassar, R.; Lua, Y.; Shokuhfar, T. Facile hydrothermal synthesis of antibacterial multi-layered hydroxyapatite nanostructures with superior flexibility. *CrystEngComm* **2018**, *20*, 1304–1312. [[CrossRef](#)]
155. Lakrat, M.; Jodati, H.; Mejdoubi, E.M.; Evis, Z. Synthesis and characterization of pure and Mg, Cu, Ag, and Sr doped calcium-deficient hydroxyapatite from brushite as precursor using the dissolution-precipitation method. *Powder Technol.* **2023**, *413*, 118026. [[CrossRef](#)]

156. Li, X.; Zou, Q.; Man, Y.; Li, W. Synergistic Effects of Novel Superparamagnetic/Upconversion HA Material and Ti/Magnet Implant on Biological Performance and Long-Term In Vivo Tracking. *Small* **2019**, *15*, 1901617. [[CrossRef](#)]
157. Schwartz, K.; Milne, D. Growth-promoting Effects of Silicon in Rats. *Nature* **1972**, *239*, 333–334. [[CrossRef](#)] [[PubMed](#)]
158. Srinath, P.; Azeem, P.A.; Reddy, K.V. Review on calcium silicate-based bioceramics in bone tissue engineering. *International Journal of Applied Ceramic Technology*. *Int. J. Appl. Ceram. Technol.* **2020**, *17*, 2450–2464. [[CrossRef](#)]
159. Gomez-Vazquez, O.M.; Correa-Piña, B.A.; Zubieta-Otero, L.F.; Castillo-Paz, A.M.; Londoño-Restrepo, S.M.; Rodriguez-García, M.E. Synthesis and characterization of bioinspired nano-hydroxyapatite by wet chemical precipitation. *Ceram. Int.* **2021**, *47*, 32775–32785. [[CrossRef](#)]
160. Tarafder, S.; Davies, N.M.; Bandyopadhyay, A.; Bose, S. 3D printed tricalcium phosphate bone tissue engineering scaffolds: Effect of SrO and MgO doping on in vivo osteogenesis in a rat distal femoral defect model. *Biomater. Sci.* **2013**, *1*, 1250–1259. [[CrossRef](#)]
161. Campodoni, E.; Montanari, M.; Artusi, C.; Bergamini, L.; Bassi, G.; Destro, E.; Fenoglio, I.; Panseri, S.; Tampieri, A.; Sanson, A.; et al. Biominerization: A new tool for developing eco-sustainable Ti-doped hydroxyapatite-based hybrid UV filters. *Biomater. Adv.* **2023**, *151*, 213474. [[CrossRef](#)]
162. Li, J.; Zhang, T.; Liao, Z.; Wei, Y.; Hang, R.; Huang, D. Engineered functional doped hydroxyapatite coating on titanium implants for osseointegration. *J. Mater. Res. Technol.* **2023**, *27*, 122–152. [[CrossRef](#)]
163. Li, X.; Zou, Q.; Chen, H.; Li, W. In vivo changes of nanoapatite crystals during bone reconstruction and the differences with native bone apatite. *Sci. Adv.* **2019**, *5*, eaay6484. [[CrossRef](#)]
164. Ottensmeyer, P.F.; Witzler, M.; Schulze, M. Small Molecules Enhance Scaffold-Based Bone Grafts via Purinergic Receptor Signaling in Stem Cells. *Int. J. Mol. Sci.* **2018**, *19*, 3601. [[CrossRef](#)]
165. Noorzai, S.; Johannes, C.; Verbeek, R.; Christopher, M.; Janis, L. Collagen Extraction from Various Waste Bovine Hide Sources. *Waste Biomass Valorization* **2020**, *11*, 5687–5698. [[CrossRef](#)]
166. Brooker, C.; Tronci, G. Effect of Mammalian Tissue Source on the Molecular and Macroscopic Characteristics of UV-Cured Type I Collagen Hydrogel Networks. *Prosthesia* **2022**, *4*, 1. [[CrossRef](#)]
167. Acharya, P.P.; Kupendra, M.H.; Fasim, A.; Shivajirao, S.; Krishna, M.V. A comparative assessment of collagen type 1 from silver carp (fresh water) and milk shark (marine) fish waste. *3 Biotech* **2022**, *12*, 82. [[CrossRef](#)] [[PubMed](#)]
168. Binlatcheh, T.; Thammanichanon, P.; Rittipakorn, P.; Thinsathid, N.; Jitprasertwong, P. Collagen-Based Biomaterials in Periodontal Regeneration: Current Applications and Future Perspectives of. *Biomimetics* **2022**, *7*, 34. [[CrossRef](#)] [[PubMed](#)]
169. Shoulders, M.D.; Raines, R.T. Collagen Structure and Stability. *Annu. Rev. Biochem.* **2009**, *78*, 929–958. [[CrossRef](#)]
170. Lin, K.; Zhang, D.; Macedo, M.H.; Cui, W.; Sarmento, B. Advanced Collagen-Based Biomaterials for Regenerative Biomedicine. *Adv. Funct. Mater.* **2019**, *29*, 1804943. [[CrossRef](#)]
171. Ferreira, A.M.; Gentile, P.; Chiono, V.; Ciardelli, G. Collagen for bone tissue regeneration. *Acta Biomater.* **2012**, *8*, 3191–3200. [[CrossRef](#)]
172. Leary, L.E.R.O.; Fallas, J.A.; Bakota, E.L.; Kang, M.K.; Hartgerink, J.D. Multi-hierarchical self-assembly of a collagen mimetic peptide from triple helix to nanofibre and hydrogel. *Nat. Chem.* **2011**, *3*, 821–828. [[CrossRef](#)]
173. Tan, X.; Xue, Z.; Zhu, H.; Wang, X.; Xu, D. How Charged Amino Acids Regulate Nucleation of Biomimetic Hydroxyapatite Nanoparticles on the Surface of Collagen Mimetic Peptides: Molecular Dynamics and Free Energy Investigations. *Cryst. Growth Des.* **2020**, *20*, 4561–4572. [[CrossRef](#)]
174. Duanis-Assaf, T.; Hu, T.; Lavie, M.; Zhang, Z.; Reches, M. Understanding the Adhesion Mechanism of Hydroxyapatite-Binding Peptide. *Langmuir* **2022**, *38*, 968–978. [[CrossRef](#)] [[PubMed](#)]
175. Wang, S.; Umrath, F.; Cen, W.; Reinert, S.; Alexander, D. Angiogenic Potential of VEGF Mimetic Peptides for the Biofunctionalization of Collagen/Hydroxyapatite Composites. *Biomolecules* **2021**, *11*, 1538. [[CrossRef](#)] [[PubMed](#)]
176. Ling, C.; Zhao, W.; Wang, Z.; Chen, J.; Ustriyana, P.; Gao, M.; Sahai, N. Structure–Activity Relationships of Hydroxyapatite-Binding Peptides. *Langmuir* **2020**, *36*, 2729–2739. [[CrossRef](#)] [[PubMed](#)]
177. Xue, Z.; Wang, X.; Xu, D. Molecular dynamic simulation of prenucleation of apatite at a type I collagen template: Ion association and mineralization control. *Phys. Chem. Chem. Phys.* **2022**, *24*, 11370–11381. [[CrossRef](#)] [[PubMed](#)]
178. Zhou, L.; Wong, H.M.; Zhang, Y.Y.; Li, Q.L. Constructing an Antibiofouling and Mineralizing Bioactive Tooth Surface to Protect against Decay and Promote Self-Healing. *ACS Appl. Mater. Interfaces* **2020**, *12*, 3021–3031. [[CrossRef](#)]
179. Zhou, L.; Li, Q.L.; Wong, H.M. A Novel Strategy for Caries Management: Constructing an Antibiofouling and Mineralizing Dual-Bioactive Tooth Surface. *ACS Appl. Mater. Interfaces* **2021**, *13*, 31140–31152. [[CrossRef](#)]
180. Zhou, Z.; Ge, X.; Bian, M.; Xu, T.; Li, N.; Lu, J.; Yu, J. Remineralization of dentin slices using casein phosphopeptide—Amorphous calcium phosphate combined with sodium tripolyphosphate. *Biomed. Eng.* **2020**, *19*, 18. [[CrossRef](#)]
181. Buckle, E.L.; Prakash, A.; Bonomi, M.; Sampath, J.; Pfaendtner, J.; Drobny, G.P. Solid-State NMR and MD Study of the Structure of the Statherin Mutant SNa15 on Mineral Surfaces. *J. Am. Chem. Soc.* **2019**, *141*, 1998–2011. [[CrossRef](#)]
182. Zeng, J.; Yang, S.; Yu, H.; Xu, Z.; Quan, X.; Zhou, J. Simulation Insight into the Synergic Role of Citrate and Polyaspartic Peptide in Biominerization. *Langmuir* **2021**, *37*, 3410–3419. [[CrossRef](#)]
183. Basu, S.; Basu, B.; Maiti, P.K. A computational study on strontium ion modified hydroxyapatite–fibronectin interactions. *Phys. Chem. Chem. Phys.* **2023**, *24*, 27989–28002. [[CrossRef](#)]
184. Khor, E.; Yong, L. Implantable applications of chitin and chitosan. *Biomaterials* **2003**, *24*, 2339–2349. [[CrossRef](#)]

185. Korpayev, S.; Kaygusuz, G.; Murat, S.; Orhan, K. International Journal of Biological Macromolecules Chitosan/collagen based biomimetic osteochondral tissue constructs: A growth factor-free approach. *Int. J. Biol. Macromol.* **2020**, *156*, 681–690. [[CrossRef](#)] [[PubMed](#)]
186. Jia, M.; Kim, J.; Rolandi, M.; Duong, T. Natural biopolymers as proton conductors in bioelectronics. *Biopolymers* **2021**, *112*, e23433. [[CrossRef](#)]
187. Pakizeh, M.; Moradi, A.; Ghassemi, T. Chemical extraction and modification of chitin and chitosan from shrimp shells. *Eur. Polym. J.* **2021**, *159*, 110709. [[CrossRef](#)]
188. Al Sagheer, F.A.; Al-Sughayer, M.A.; Muslim, S.; Elsabee, M.Z. Extraction and characterization of chitin and chitosan from marine sources in Arabian Gulf. *Carbohydr. Polym.* **2009**, *77*, 410–419. [[CrossRef](#)]
189. Bajaj, M.; Winter, J.; Gallert, C. Effect of deproteinization and deacetylation conditions on viscosity of chitin and chitosan extracted from Crangon crangon shrimp waste. *Biochem. Eng. J.* **2011**, *56*, 51–62. [[CrossRef](#)]
190. Tian, X.; Hua, T.; Poon, T.; Yang, Y.; Hu, H.; Fu, J.; Li, J.; Niu, B. Study on Effects of Blending Fiber Type and Ratio on Antibacterial Properties of Chitosan Blended Yarns and Fabrics. *Fibers Polym.* **2022**, *23*, 2565–2576. [[CrossRef](#)]
191. Wu, P.; Xi, X.; Li, R.; Sun, G. Engineering Polysaccharides for Tissue Repair and Regeneration. *Macromol. Biosci.* **2021**, *21*, 2100141. [[CrossRef](#)]
192. Bakshi, P.S.; Selvakumar, D.; Kadirvelu, K.; Kumar, N.S. International Journal of Biological Macromolecules Chitosan as an environment friendly biomaterial—A review on recent modifications and applications. *Int. J. Biol. Macromol.* **2020**, *150*, 1072–1083. [[CrossRef](#)]
193. Tian, Y.; Wu, D.; Wu, D.; Cui, Y.; Ren, G.; Wang, Y.; Webster, T. Chitosan-Based Biomaterial Scaffolds for the Repair of Infected Bone Defects. *Front. Bioeng. Biotechnol.* **2022**, *10*, 899760. [[CrossRef](#)]
194. Patel, A.; Zaky, S.H.; Schoedel, K.; Li, H.; Sant, V.; Beniash, E.; Sfeir, C.; Stoltz, D.B.; Sant, S. Acta Biomaterialia Design and evaluation of collagen-inspired mineral-hydrogel nanocomposites for bone regeneration. *Acta Biomater.* **2020**, *112*, 262–273. [[CrossRef](#)]
195. Zhang, S.; Zhao, G.; Ma, W.; Song, Y.; Huang, C.; Xie, C. The root-like chitosan nanofiber porous scaffold cross-linked by genipin with type I collagen and its osteoblast compatibility. *Carbohydr. Polym.* **2022**, *285*, 119255. [[CrossRef](#)]
196. Tao, F.; Cheng, Y.; Shi, X.; Zheng, H.; Du, Y.; Xiang, W.; Deng, H. Applications of chitin and chitosan nano fibers in bone regenerative engineering. *Carbohydr. Polym.* **2020**, *230*, 115658. [[CrossRef](#)] [[PubMed](#)]
197. Shen, Y.; Xu, Y.; Yi, B.; Wang, X.; Tang, H.; Chen, C.; Zhang, Y. Engineering a Highly Biomimetic Chitosan-Based Cartilage Scaffold by Using Short Fibers and a Cartilage-Decellularized Matrix. *Biomacromolecules* **2021**, *22*, 2284–2297. [[CrossRef](#)] [[PubMed](#)]
198. Sukpaita, T.; Chirachanchai, S.; Pimchaokham, A.; Ampornaramveth, R.S. Chitosan-based scaffold for mineralized tissues regeneration. *Mar. Drugs* **2021**, *19*, 551. [[CrossRef](#)] [[PubMed](#)]
199. Emilia, S.; Winnicka, K. Stability of Chitosan—A Challenge for Pharmaceutical and Biomedical Applications. *Mar. Drugs* **2015**, *13*, 1819–1846. [[CrossRef](#)]
200. Dash, M.; Chiellini, F.; Ottenbrite, R.M.; Chiellini, E. Progress in Polymer Science Chitosan—A versatile semi-synthetic polymer in biomedical applications. *Prog. Polym. Sci.* **2011**, *36*, 981–1014. [[CrossRef](#)]
201. Jayakumar, R.; Prabaharan, M.; Kumar, P.T.S.; Nair, S.V.; Tamura, H. Biomaterials based on chitin and chitosan in wound dressing applications. *Biotechnol. Adv.* **2011**, *29*, 322–337. [[CrossRef](#)]
202. Levengood, S.K.L.; Zhang, M. Chitosan-based scaffolds for bone tissue engineering. *J. Mater. Chem. B* **2014**, *2*, 3161–3184. [[CrossRef](#)]
203. Mogosanu, G.D.; Grumezescu, M.A. Natural and synthetic polymers for wounds and burns dressing. *Int. J. Pharm.* **2014**, *463*, 127–136. [[CrossRef](#)]
204. Lim, C.; Hwang, S.D.; Lee, W.D. Intermolecular interactions of chitosan: Degree of acetylation and molecular weight. *Carbohydr. Polym.* **2021**, *259*, 117782. [[CrossRef](#)] [[PubMed](#)]
205. Hsu, S.-H.; Whu, S.W.; Hsieh, S.-C.; Tsai, C.-L.; Chen, D.C.; Tan, T. Evaluation of Chitosan-alginate-hyaluronate Complexes Modified by an RGD-containing Protein as Tissue-engineering Scaffolds for Cartilage Regeneration. *Artif. Organs* **2004**, *28*, 693–703. [[CrossRef](#)] [[PubMed](#)]
206. Hsu, S.; Whu, S.W.; Tsai, C.; Wu, Y.; Chen, H.; Hsieh, K. Chitosan as Scaffold Materials: Effects of Molecular Weight and Degree of Deacetylation. *J. Polym. Res.* **2004**, *11*, 141–147. [[CrossRef](#)]
207. Hou, X.; Zhang, L.; Zhou, Z.; Luo, X.; Wang, T.; Zhao, X. Calcium Phosphate-Based Biomaterials for Bone Repair. *Funct. Mater.* **2022**, *13*, 187. [[CrossRef](#)] [[PubMed](#)]
208. Zhang, H.P.; Lu, X.; Fang, L.M.; Qu, S.X.; Feng, B.; Weng, J. Atomic-scale interactions at the interface of biopolymer/hydroxyapatite. *Biomed. Mater.* **2008**, *3*, 44110. [[CrossRef](#)]
209. Mathesan, S.; Rath, A.; Ghosh, P. Molecular mechanisms in deformation of cross-linked hydrogel nanocomposite. *Mater. Sci. Eng. C* **2016**, *59*, 157–167. [[CrossRef](#)]
210. Snyder, A.D.; Salehinia, I. Study of nanoscale deformation mechanisms in bulk hexagonal hydroxyapatite under uniaxial loading using molecular dynamics. *J. Mech. Behav. Biomed. Mater.* **2020**, *110*, 103894. [[CrossRef](#)]
211. Ji, C.; He, B.; Yun, S.; Bai, X.; Lin, B. Journal of the Mechanical Behavior of Biomedical Materials The fracture mechanical behavior simulation of calcium-deficient hydroxyapatite crystals by molecular dynamics and first-principles calculation. *J. Mech. Behav. Biomed. Mater.* **2023**, *137*, 105526. [[CrossRef](#)]

212. Lew, A.J.; Beniash, E.; Gilbert, P.U.P.A.; Buehler, M.J. Role of the Mineral in the Self-Healing of Cracks in Human Enamel. *ASC Nano* **2022**, *16*, 10273–10280. [[CrossRef](#)]
213. Patrulea, V.; Ostafe, V.; Borchard, G.; Jordan, O. European Journal of Pharmaceutics and Biopharmaceutics Chitosan as a starting material for wound healing applications. *Eur. J. Pharm. Biopharm.* **2015**, *97*, 417–426. [[CrossRef](#)]
214. Croisier, F.; Jérôme, C. Chitosan-based biomaterials for tissue engineering. *Eur. Polym. J.* **2013**, *49*, 780–792. [[CrossRef](#)]
215. Venkatesan, J.; Kim, S. Chitosan Composites for Bone Tissue Engineering—An Overview. *Mar. Drugs* **2010**, *8*, 2252–2266. [[CrossRef](#)] [[PubMed](#)]
216. Wang, W.; Meng, Q.; Li, Q.; Liu, J.; Zhou, M.; Jin, Z.; Zhao, K. Chitosan Derivatives and Their Application in Biomedicine. *Int. J. Mol. Sci.* **2020**, *21*, 487. [[CrossRef](#)] [[PubMed](#)]
217. Holme, K.R.; Perlin, A.S. Chitosan N-sulfate. A water-soluble polyelectrolyte. *Carbohydr. Res.* **1997**, *302*, 7–12. [[CrossRef](#)] [[PubMed](#)]
218. Nishimura, S.; Kai, H.; Shinada, K.; Yoshidaa, T.; Tokurab, S.; Kurita, K.; Nakashimad, H.; Yamamotod, N.; Uryue, T. Regioselective syntheses of sulfated polysaccharides: Specific anti-HIV-1 activity of novel chitin sulfates. *Carbohydr. Res.* **1998**, *306*, 427–433. [[CrossRef](#)]
219. Budiraharjo, R.; Neoh, K.G.; Kang, E.T.; Kishen, A. Bioactivity of novel carboxymethyl chitosan scaffold incorporating MTA in a tooth model. *Int. Endod. J.* **2010**, *43*, 930–939. [[CrossRef](#)]
220. Oliveira, A.L.; Mano, J.F.; Reis, R.L. Nature-inspired calcium phosphate coatings: Present status and novel advances in the science of mimicry. *Curr. Opin. Solid State Mater. Sci.* **2003**, *7*, 309–318. [[CrossRef](#)]
221. Sagar, N.; Pandey, A.K.; Gurbani, D.; Khan, K.; Singh, D.; Chaudhari, B.P.; Soni, V.P.; Chattopadhyay, N.; Dhawan, A.; Bellare, J.R. In-Vivo Efficacy of Compliant 3D Nano-Composite in Critical-Size Bone Defect Repair: A Six Month Preclinical Study in Rabbit. *PLoS ONE* **2013**, *8*, e77578. [[CrossRef](#)]
222. Zheng, Z.; Zhang, W.; Sun, W. Influence of the carboxymethyl chitosan anti-adhesion solution on the TGF- β 1 in a postoperative peritoneal adhesion rat. *J. Mater. Sci. Mater. Med.* **2013**, *24*, 2549–2559. [[CrossRef](#)]
223. Qiao, J.; Liu, Y.; Jiang, Z.; Yang, Y.; Liu, W.; Han, B. Preparation and renoprotective effects of carboxymethyl chitosan oligosaccharide on adriamycin nephropathy. *Carbohydr. Polym.* **2018**, *201*, 347–356. [[CrossRef](#)]
224. Liu, X.; Wu, Y.; Zhao, X.; Wang, Z. Fabrication and applications of bioactive chitosan-based organic-inorganic hybrid materials: A review. *Carbohydr. Polym.* **2021**, *267*, 118179. [[CrossRef](#)] [[PubMed](#)]
225. Ghilan, A.; Chiriac, A.P.; Nita, L.E.; Rusu, A.G.; Neamtu, I.; Chiriac, V.M. Trends in 3D Printing Processes for Biomedical Field: Opportunities and Challenges. *J. Polym. Environ.* **2020**, *28*, 1345–1367. [[CrossRef](#)] [[PubMed](#)]
226. Kantaros, A. 3D Printing in Regenerative Medicine: Technologies and Resources Utilized. *Int. J. Mol. Sci.* **2022**, *23*, 14621. [[CrossRef](#)] [[PubMed](#)]
227. Yusoff, N.H.M.; Teo, L.-R.I.; Phang, S.-J.; Wong, V.-L.; Cheah, K.-H.; Siew-Shee, L. Recent Advances in Polymer-based 3D Printing for Wastewater Treatment Application: An Overview. *Chem. Eng. J.* **2021**, *429*, 132311. [[CrossRef](#)]
228. Nyberg, E.; Rindone, A.; Dorafshar, A.; Grayson, W.L. Comparison of 3D-Printed Poly-e-Caprolactone Scaffolds Functionalized with Tricalcium Phosphate, Hydroxyapatite, Bio-Oss, or Decellularized Bone Matrix. *Tissue Eng. Part A* **2017**, *23*, 503–514. [[CrossRef](#)]
229. Wu, Y.; Sriram, G.; Fawzy, A.S.; Fuh, J.Y.H.; Rosa, V.; Cao, T.; Wong, Y.S. Fabrication and evaluation of electrohydrodynamic jet 3D printed polycaprolactone/chitosan cell carriers using human embryonic stem cell-derived fibroblasts. *J. Biomater. Appl.* **2016**, *31*, 181–192. [[CrossRef](#)]
230. Hernandez, I.; Kumar, A. A Bioactive Hydrogel and 3D Printed Polycaprolactone System for Bone Tissue Engineering. *Gels* **2017**, *3*, 26. [[CrossRef](#)]
231. Kim, J.; Ahn, G.; Kim, C.; Lee, J.; Lee, I.; An, S.; Yun, W.; Kim, S.; Shim, J. Synergistic Effects of Beta Tri-Calcium Phosphate and Porcine-Derived Decellularized Bone Extracellular Matrix in 3D-Printed Polycaprolactone Scaffold on Bone Regeneration. *Macromol. Biosci.* **2018**, *18*, 1800025. [[CrossRef](#)]
232. Cho, S.Y.; Choi, S.; Lee, S.-H.; Kim, K.K.; Cho, Y. Assessments of polycaprolactone/hydroxyapatite composite scaffold with enhanced biomimetic mineralization by exposure to hydroxyapatite via a 3D-printing system and alkaline erosion. *Eur. Polym. J.* **2019**, *113*, 340–348. [[CrossRef](#)]
233. Kurzyk, A.; Ostrowska, B.; Wojciech, Š.; Pojda, Z. Characterization and Optimization of the Seeding Process of Adipose Stem Cells on the Polycaprolactone Scaffolds. *Stem Cells Int.* **2019**, *2019*, 1201927. [[CrossRef](#)]
234. Cakmak, A.M.; Unal, S.; Sahin, A.; Oktar, F.N.; Sengor, M.; Ekren, N.; Gunduz, O.; Kalaskar, D.M. 3D Printed Polycaprolactone/Gelatin/Bacterial Cellulose/Hydroxyapatite Composite Scaffold for Bone Tissue Engineering. *Polymers* **2020**, *12*, 1962. [[CrossRef](#)] [[PubMed](#)]
235. Hedayati, S.K.; Behravesh, A.H.; Hasannia, S.; Bagheri Saed, A.; Akhoundi, B. 3D printed PCL scaffold reinforced with continuous biodegradable fiber yarn: A study on mechanical and cell viability properties. *Polym. Test.* **2020**, *83*, 106347. [[CrossRef](#)]
236. Jeong, H.-J.; Gwak, S.-J.; Seo, K.D.; Lee, S.; Yun, J.-H.; Cho, Y.-S.; Lee, S.-J. Fabrication of Three-Dimensional Composite Scaffold for Simultaneous Alveolar Bone Regeneration in Dental Implant Installation. *Int. J. Mol. Sci.* **2020**, *21*, 1863. [[CrossRef](#)] [[PubMed](#)]
237. Liu, Y.; Wang, R.; Chen, S.; Xu, Z.; Wang, Q.; Yuan, P.; Zhou, Y.; Zhang, Y.; Chen, J. Heparan sulfate loaded polycaprolactone-hydroxyapatite scaffolds with 3D printing for bone defect repair. *Int. J. Biol. Macromol.* **2020**, *148*, 153–162. [[CrossRef](#)]

238. Moura, C.; Trindade, D.; Vieira, M.; Francisco, L.; Ângelo, D.F.; Alves, N. Multi-Material Implants for Temporomandibular Joint Disc Repair: Tailored Additive Manufacturing Production. *Front. Bioeng. Biotechnol.* **2020**, *8*, 342. [CrossRef] [PubMed]
239. Thunsiri, K.; Pitjamit, S.; Pothacharoen, P.; Prusakorn, D.; Nakkiew, W.; Wattanutchariya, W. The 3D-Printed Bilayer's Bioactive-Biomaterials Scaffold for Full-Thickness Articular Cartilage Defects Treatment. *Materials* **2020**, *13*, 3417. [CrossRef]
240. El-Habashy, S.E.; El-Kamel, A.H.; Essawy, M.M.; Abdelfattah, E.A.; Eltaher, H.M. Engineering 3D-printed core–shell hydrogel scaffolds reinforced with hybrid hydroxyapatite/polycaprolactone nanoparticles for in vivo bone regeneration. *Biomater. Sci.* **2021**, *9*, 4019–4039. [CrossRef]
241. Kim, Y.; Son, K.; Lee, J. Auxetic structures for tissue engineering scaffolds and biomedical devices. *Materials* **2021**, *14*, 6821. [CrossRef]
242. Li, Y.; Yu, Z.; Ai, F.; Wu, C.; Zhou, K.; Cao, C.; Li, W. Characterization and evaluation of polycaprolactone/hydroxyapatite composite scaffolds with extra surface morphology by cryogenic printing for bone tissue engineering. *Mater. Des.* **2021**, *205*, 109712. [CrossRef]
243. Petretta, M.; Gambardella, A.; Desando, G.; Cavallo, C.; Bartolotti, I.; Shelyakova, T.; Goranov, V.; Brucale, M.; Dediu, V.A.; Fini, M.; et al. Multifunctional 3D-Printed Magnetic Polycaprolactone/Hydroxyapatite Scaffolds for Bone Tissue Engineering. *Polymers* **2021**, *13*, 3825. [CrossRef]
244. Rezaei, F.S.; Khorshidian, A.; Beram, M. 3D printed chitosan/polycaprolactone scaffold for lung tissue engineering: Hope to be useful for. *RSC Adv.* **2021**, *11*, 19508–19520. [CrossRef] [PubMed]
245. Xu, Z.; Omar, A.M.; Bartolo, P. Experimental and Numerical Simulations of 3D-Printed Polycaprolactone Scaffolds for Bone Tissue Engineering Applications. *Materials* **2021**, *14*, 3546. [CrossRef] [PubMed]
246. Biscaia, S.; Branquinho, M.V.; Alvites, R.D.; Fonseca, R.; Sousa, A.C.; Pedrosa, S.; Caseiro, A.R.; Guedes, F.; Patr, T.; Viana, T.; et al. 3D Printed Poly(ϵ -caprolactone)/Hydroxyapatite Scaffolds for Bone Tissue Engineering: A Comparative Study on a Composite Preparation by Melt Blending or Solvent Casting Techniques and the Influence of Bioceramic Content on Scaffold Properties. *Int. J. Mol. Sci.* **2022**, *23*, 2318. [CrossRef] [PubMed]
247. Gonzalez-Pujana, A.; Carranza, T.; Santos-vizcaino, E.; Igartua, M. Hybrid 3D Printed and Electrospun Multi-Scale Hierarchical Polycaprolactone Scaffolds to Induce Bone Differentiation. *Pharmaceutics* **2022**, *14*, 2843. [CrossRef]
248. Sousa, A.C.; Biscaia, S.; Alvites, R.; Branquinho, M.; Lopes, B.; Valente, J.; Franco, M.; Santos, D.; Mendonça, C.; Alves, N.; et al. Assessment of 3D-Printed Polycaprolactone, Hydroxyapatite Nanoparticles and Diacrylate Poly(ethylene glycol) Scaffolds for Bone Regeneration. *Pharmaceutics* **2022**, *14*, 2643. [CrossRef]
249. López-González, I.; Hernández-Heredia, A.B.; Rodríguez-López, M.I.; Auñón-Calles, D.; Boudifa, M.; Gabaldón, J.A.; Meseguer-Olmo, L. Evaluation of the In Vitro Antimicrobial Efficacy against *Staphylococcus Aureus* and *Epidermidis* of a Novel 3D-Printed Degradable Drug Delivery System Based on Polycaprolactone/Chitosan/Vancomycin—Preclinical Study. *Pharmaceutics* **2023**, *15*, 1763. [CrossRef]
250. Lee, S.J.; Heo, D.N.; Park, J.S.; Kwon, S.K.; Lee, J.H.; Lee, J.H.; Kim, W.D.; Kwon, I.K.; Park, S.A. Characterization and preparation of bio-tubular scaffolds for fabricating artificial vascular grafts by combining electrospinning and a 3D printing system. *Phys. Chem. Chem. Phys.* **2014**, *17*, 2996–2999. [CrossRef]
251. Najafabadi, F.M.; Karbasi, S.; Benisi, S.Z.; Shojaei, S. Physical, mechanical, and biological performance of chitosan-based nanocomposite coating deposited on the polycaprolactone-based 3D printed scaffold: Potential application in bone tissue engineering. *Int. J. Biol. Macromol.* **2023**, *243*, 125218. [CrossRef]
252. Chia, H.N.; Wu, B.M. Recent advances in 3D printing of biomaterials. *J. Biol. Eng.* **2015**, *9*, 4. [CrossRef]
253. Huang, B.; Bártolo, P.J. Rheological characterization of polymer/ceramic blends for 3D printing of bone scaffolds. *Polym. Test.* **2018**, *68*, 365–378. [CrossRef]
254. Babilotte, J.; Guduric, V.; Le Nihouannen, D.; Naveau, A.; Fricain, J.C.; Catros, S. 3D printed polymer–mineral composite biomaterials for bone tissue engineering: Fabrication and characterization. *J. Biomed. Mater. Res. Part B Appl. Biomater.* **2019**, *107*, 2579–2595. [CrossRef] [PubMed]
255. Šupová, M. Problem of hydroxyapatite dispersion in polymer matrices: A review. *J. Mater. Sci. Mater. Med.* **2009**, *20*, 1201–1213. [CrossRef] [PubMed]
256. Mohd Pu'Ad, N.A.S.; Abdul Haq, R.H.; Mohd Noh, H.; Abdullah, H.Z.; Idris, M.I.; Lee, T.C. Synthesis method of hydroxyapatite: A review. *Mater. Today Proc.* **2019**, *29*, 233–239. [CrossRef]
257. Seyedsalehi, A.; Daneshmandi, L.; Barajaa, M.; Riordan, J.; Laurencin, C.T. Fabrication and characterization of mechanically competent 3D printed polycaprolactone-reduced graphene oxide scaffolds. *Sci. Rep.* **2020**, *10*, 22210. [CrossRef]
258. Ogata, N.; Yamaguchi, S.; Shimada, N.; Lu, G.; Iwata, T.; Nakane, K.; Ogihara, T. Poly(lactide) Nanofibers Produced by a Melt-Electrospinning System with a Laser Melting Device. *J. Appl. Polym. Sci.* **2007**, *104*, 1641–1645. [CrossRef]
259. Wissamitanan, T.; Dechwayukul, C.; Kalkornsurapranee, E.; Thongruang, W. Proper blends of biodegradable polycaprolactone and natural rubber for 3D printing. *Polymers* **2020**, *12*, 2416. [CrossRef]
260. Ghorbani, F.M.; Kaffashi, B.; Shokrollahi, P.; Akhlaghi, S.; Hedenqvist, M. Effect of hydroxyapatite nano-particles on morphology, rheology and thermal behavior of poly(caprolactone)/chitosan blends. *Mater. Sci. Eng. C* **2016**, *59*, 980–989. [CrossRef]
261. Dubinenko, G.; Zinoviev, A.; Bolbasov, E.; Kozelskaya, A.; Shesterikov, E.; Novikov, V.; Tverdokhlebov, S. Highly filled poly(l-lactic acid)/hydroxyapatite composite for 3D printing of personalized bone tissue engineering scaffolds. *J. Appl. Polym. Sci.* **2021**, *138*, 49662. [CrossRef]

262. Honarvar, A.; Karbasi, S.; Hashemibeni, B.; Setayeshmehr, M.; Kazemi, M.; Valiani, A. Effects of cartilage acellular solubilised ECM on physicomechanical and biological properties of polycaprolactone/fibrin hybrid scaffold fabricated by 3D-printing and salt-leaching methods. *Mater. Technol.* **2022**, *37*, 204–212. [[CrossRef](#)]
263. Sun, Y.; Cheng, S.; Lu, W.; Wang, Y.; Zhang, P.; Yao, Q. Electrospun fibers and their application in drug controlled release, biological dressings, tissue repair, and enzyme immobilization. *RSC Adv.* **2019**, *9*, 25712–25729. [[CrossRef](#)]
264. Yoshida, M.; Turner, P.R.; Ali, M.A.; Cabral, J.D. Three-Dimensional Melt-Electrowritten Polycaprolactone/Chitosan Scaffolds Enhance Mesenchymal Stem Cell Behavior. *ACS Appl. Bio Mater.* **2021**, *4*, 1319–1329. [[CrossRef](#)] [[PubMed](#)]
265. Nawrotek, K.; Małkiewicz, M.; Zawadzki, D. Fabrication and Characterization of Polycaprolactone/Chitosan—Hydroxyapatite Hybrid Implants for Peripheral. *Polymers* **2021**, *13*, 775. [[CrossRef](#)] [[PubMed](#)]
266. Sarasam, A.; Madihally, S.V. Characterization of chitosan—Polycaprolactone blends for tissue engineering applications. *Biomaterials* **2005**, *26*, 5500–5508. [[CrossRef](#)] [[PubMed](#)]
267. Li, Y.; Peng, Y.; Hu, Y.; Liu, J.; Yuan, T.; Zhou, W.; Dong, X.; Wang, C.; Binks, B.P.; Yang, Z. Fabrication of Poly(ϵ -caprolactone)-embedded Lignin-Chitosan Nanocomposite Porous Scaffolds from Pickering Emulsions. *Langmuir* **2023**, *39*, 6947–6956. [[CrossRef](#)] [[PubMed](#)]
268. Hassanajili, S.; Pour, A.; Oryan, A.; Talaei-Khozani, T. Preparation and characterization of PLA/PCL/HA composite scaffolds using indirect 3D printing for bone tissue engineering. *Mater. Sci. Eng. C* **2019**, *104*, 109960. [[CrossRef](#)]
269. Freeman, F.E.; Brennan, M.Á.; Browne, D.C.; Renaud, A.; De Lima, J.; Kelly, D.J.; Mcnamara, L.M.; Layrolle, P. A Developmental Engineering-Based Approach to Bone Repair: Endochondral Priming Enhances Vascularization and New Bone Formation in a Critical Size Defect. *Front. Bioeng. Biotechnol.* **2020**, *8*, 230. [[CrossRef](#)]
270. Mohammadi, H.; Sepantafar, M.; Muhamad, N.; Bakar Sulong, A. How Does Scaffold Porosity Conduct Bone Tissue Regeneration? *Adv. Eng. Mater.* **2021**, *23*, 2100463. [[CrossRef](#)]
271. Moura, C.S.; Da Silva, C.L.; Bárto, P.J.; Ferreira, F.C. Combination of 3D extruded-based poly(ϵ -caprolactone) scaffolds with mesenchymal stem/stromal cells: Strategy optimization. *Procedia Eng.* **2015**, *110*, 122–127. [[CrossRef](#)]
272. Oh, S.H.; Park, I.K.; Kim, J.M.; Lee, J.H. In vitro and in vivo characteristics of PCL scaffolds with pore size gradient fabricated by a centrifugation method. *Biomaterials* **2007**, *28*, 1664–1671. [[CrossRef](#)]
273. Fantini, M.; Curto, M.; De Crescenzo, F. A method to design biomimetic scaffolds for bone tissue engineering based on Voronoi lattices. *Virtual Phys. Prototyp.* **2016**, *11*, 77–90. [[CrossRef](#)]
274. Kühl, J.; Gorb, S.; Kern, M.; Klüter, T.; Kühl, S.; Seekamp, A.; Fuchs, S. Extrusion-based 3D printing of osteoinductive scaffolds with a spongiosa-inspired structure. *Front. Bioeng. Biotechnol.* **2023**, *11*, 1–18. [[CrossRef](#)] [[PubMed](#)]
275. Gonçalves, E.M.; Oliveira, F.J.; Silva, R.F.; Neto, M.A.; Fernandes, M.H.; Amaral, M.; Vallet-Regí, M.; Vila, M. Three-dimensional printed PCL-hydroxyapatite scaffolds filled with CNTs for bone cell growth stimulation. *J. Biomed. Mater. Res. Part B Appl. Biomater.* **2016**, *104*, 1210–1219. [[CrossRef](#)] [[PubMed](#)]
276. Park, J.S.; Lee, S.J.; Jo, H.H.; Lee, J.H.; Kim, W.D.; Lee, J.Y.; Park, S.A. Fabrication and characterization of 3D-printed bone-like β -tricalcium phosphate/polycaprolactone scaffolds for dental tissue engineering. *J. Ind. Eng. Chem.* **2017**, *46*, 175–181. [[CrossRef](#)]
277. Cho, Y.S.; Gwak, S.J.; Cho, Y.S. Fabrication of polycaprolactone/nano hydroxyapatite (Pcl/nHA) 3D scaffold with enhanced in vitro cell response via design for additive manufacturing (dfam). *Polymers* **2021**, *13*, 1394. [[CrossRef](#)] [[PubMed](#)]
278. Murphy, C.M.; Haugh, M.G.; O'Brien, F.J. The effect of mean pore size on cell attachment, proliferation and migration in collagen-glycosaminoglycan scaffolds for bone tissue engineering. *Biomaterials* **2010**, *31*, 461–466. [[CrossRef](#)]
279. Paris, M.; Götz, A.; Hettrich, I.; Bidan, C.M.; John, W.C.; Razi, H.; Zizak, I.; Hutmacher, D.W.; Fratzl, P.; Georg, N.; et al. SCaffold curvature-mediated novel biominerilization process originates a continuous soft tissue-to-bone interface. *Acta Biomater.* **2017**, *60*, 64–80. [[CrossRef](#)]
280. Fonseca, D.R.; Sobreiro-Almeida, R.; Sol, P.C.; Neves, N.M. Development of non-orthogonal 3D-printed scaffolds to enhance their osteogenic performance. *Biomater. Sci.* **2018**, *6*, 1569–1579. [[CrossRef](#)]
281. Zamani, Y.; Amoabediny, G.; Mohammadi, J.; Seddiqi, H.; Helder, M.N.; Zandieh-Doulabi, B.; Klein-Nulend, J.; Koolstra, J.H. 3D-printed poly(ϵ -caprolactone) scaffold with gradient mechanical properties according to force distribution in the mandible for mandibular bone tissue engineering. *J. Mech. Behav. Biomed. Mater.* **2020**, *104*, 103638. [[CrossRef](#)]
282. Athanasiou, K.A.; Zhu, C.F.; Lanctot, D.R.; Agrawal, C.M.; Wang, X. Fundamentals of biomechanics in tissue engineering of bone. *Tissue Eng.* **2000**, *6*, 361–381. [[CrossRef](#)]
283. Yaszemski, M.J.; Payne, R.G.; Hayes, W.C.; Langer, R.; Mikos, A.G. Evolution of bone transplantation: Molecular, cellular and tissue strategies to engineer human bone. *Biomaterials* **1996**, *17*, 175–185. [[CrossRef](#)]
284. Røhl, L.; Larsen, E.; Linde, F.; Odgaard, A.; Jørgensen, J. Tensile and compressive properties of cancellous bone. *J. Biomech.* **1991**, *24*, 1143–1149. [[CrossRef](#)]
285. Lv, Y.; Liu, G.; Wang, B.; Tang, Y.; Lin, Z.; Liu, J.; Wei, G.; Wang, L. Pore Strategy Design of a Novel NiTi-Nb Biomedical Porous Scaffold Based on a Triply Periodic Minimal Surface. *Front. Bioeng. Biotechnol.* **2022**, *10*, 910475. [[CrossRef](#)] [[PubMed](#)]
286. Pitrolino, K.A.; Felfel, R.M.; Pellizzeri, L.M.; McLaren, J.; Popov, A.A.; Sottile, V.; Scotchford, C.A.; Scammell, B.E.; Roberts, G.A.F.; Grant, D.M. Development and in vitro assessment of a bi-layered chitosan-nano-hydroxyapatite osteochondral scaffold. *Carbohydr. Polym.* **2022**, *282*, 119126. [[CrossRef](#)] [[PubMed](#)]
287. Fung, Y.C. Bone and Cartilage. In *Biomechanics. Mechanical Properties of Living Tissues*; Springer: New York, NY, USA, 2013; pp. 500–544, ISBN 9781441931047.

288. Tanaka, E.; Van Eijden, T. Biomechanical Behavior of the Temporomandibular Joint Disc. *Crit. Rev. Oral Biol. Med.* **2003**, *14*, 138–150. [[CrossRef](#)]
289. Jiang, N.; Yang, Y.; Zhang, L.; Jiang, Y.; Wang, M.; Zhu, S. 3D-Printed Polycaprolactone Reinforced Hydrogel as an Artificial TMJ Disc. *Res. Rep. Biomater. Bioeng.* **2021**, *100*, 1–8. [[CrossRef](#)]
290. Jiang, Y.; Guan, Y.; Lan, Y.; Chen, S.; Li, T.; Zou, S.; Hu, Z.; Ye, Q. Mechanosensitive Piezo1 in Periodontal Ligament Cells Promotes Alveolar Bone Remodeling During Orthodontic Tooth Movement. *Front. Physiol.* **2021**, *12*, 767136. [[CrossRef](#)]
291. Capponi, G.; Zambito, M.; Neri, I.; Cottone, F.; Mattarelli, M.; Vassalli, M.; Caponi, S.; Florio, T. Cellular Mechanosensitivity: Validation of an Adaptable 3D-Printed Device for Microindentation. *Nanomaterials* **2022**, *12*, 2691. [[CrossRef](#)]
292. Al-Maslamani, N.A.; Khilan, A.A.; Horn, H.F. Design of a 3D printed, motorized, uniaxial cell stretcher for microscopic and biochemical analysis of mechanotransduction. *Biol. Open* **2021**, *10*, bio057778. [[CrossRef](#)]
293. Guarino, V.; Lewandowska, M.; Bil, M.; Polak, B.; Ambrosio, L. Morphology and degradation properties of PCL/HYAFF11®composite scaffolds with multi-scale degradation rate. *Compos. Sci. Technol.* **2010**, *70*, 1826–1837. [[CrossRef](#)]
294. Woodruff, M.A.; Hutmacher, D.W. The return of a forgotten polymer—Polycaprolactone in the 21st century. *Prog. Polym. Sci.* **2010**, *35*, 1217–1256. [[CrossRef](#)]
295. Chlonda, A.; Kijeńska-Gawrońska, E.; Zdunek, J.; Swieszkowski, W. Internal nanocrystalline structure and stiffness alterations of electrospun polycaprolactone-based mats after six months of in vitro degradation. An atomic force microscopy assay. *J. Mech. Behav. Biomed. Mater.* **2020**, *101*, 103437. [[CrossRef](#)]
296. Bartnikowski, M.; Abdal-hay, A.; Bartnikowski, N.J.; Kim, K.Y. A comprehensive study of acid and base treatment of 3D printed poly(ϵ -caprolactone) scaffolds to tailor surface characteristics. *Appl. Surf. Sci.* **2021**, *555*, 149602. [[CrossRef](#)]
297. Tsuji, H.; Saeki, T.; Tsukegi, T.; Daimon, H.; Fujie, K. Comparative study on hydrolytic degradation and monomer recovery of poly(l-lactic acid) in the solid and in the melt. *Polym. Degrad. Stab.* **2008**, *93*, 1956–1963. [[CrossRef](#)]
298. Lam, C.X.F.; Teoh, S.H.; Hutmacher, D.W. Comparison of the degradation of polycaprolactone and polycaprolactone-(β -tricalcium phosphate) scaffolds in alkaline medium. *Polym. Int.* **2007**, *56*, 718–728. [[CrossRef](#)]
299. Bartnikowski, M.; Dargaville, T.R.; Ivanovski, S.; Hutmacher, D.W. Degradation mechanisms of polycaprolactone in the context of chemistry, geometry and environment. *Prog. Polym. Sci.* **2019**, *96*, 1–20. [[CrossRef](#)]
300. Huang, M.H.; Li, S.; Hutmacher, D.W.; Coudane, J.; Vert, M. Degradation characteristics of poly(ϵ -caprolactone)-based copolymers and blends. *J. Appl. Polym. Sci.* **2006**, *102*, 1681–1687. [[CrossRef](#)]
301. Li, F.; Yu, D.; Lin, X.; Liu, D.; Xia, H.; Chen, S. Biodegradation of poly(ϵ -caprolactone) (PCL) by a new *Penicillium oxalicum* strain DSYD05-1. *World J. Microbiol. Biotechnol.* **2012**, *28*, 2929–2935. [[CrossRef](#)]
302. Li, S.M.; Espartero, J.L.; Foch, P.; Vert, M. Structural characterization and hydrolytic degradation of a Zn metal initiated copolymer of L-lactide and ϵ -caprolactone. *J. Biomater. Sci. Polym. Ed.* **1996**, *8*, 165–187. [[CrossRef](#)]
303. Jennings, J.A.; Beenken, K.E.; Parker, A.C.; Smith, J.K.; Courtney, H.S.; Smeltzer, M.S.; Haggard, W.O. Polymicrobial Biofilm Inhibition Effects of Acetate-Buffered Chitosan Sponge Delivery Device. *Macromol. Biosci.* **2016**, *16*, 591–598. [[CrossRef](#)]
304. Tatu, R.R.; Oria, M.; Rao, M.B.; Peiro, J.L.; Lin, C.Y. Biodegradation of poly(l-lactic acid) and poly(ϵ -caprolactone) patches by human amniotic fluid in an in-vitro simulated fetal environment. *Sci. Rep.* **2022**, *12*, 3950. [[CrossRef](#)]
305. Greene, A.F.; Vaidya, A.; Collet, C.; Wade, K.R.; Patel, M.; Gaugler, M.; West, M.; Petcu, M.; Parker, K. 3D-printed enzyme-embedded plastics. *Biomacromolecules* **2021**, *22*, 1999–2009. [[CrossRef](#)] [[PubMed](#)]
306. Von Burkersroda, F.; Schedl, L.; Göpfertich, A. Why degradable polymers undergo surface erosion or bulk erosion. *Biomaterials* **2002**, *23*, 4221–4231. [[CrossRef](#)] [[PubMed](#)]
307. Middleton, J.C.; Tipton, A.J. Synthetic biodegradable polymers as orthopedic devices. *Biomaterials* **2000**, *21*, 2335–2346. [[CrossRef](#)]
308. Grizzi, I.; Garreau, H.; Li, S.; Vert, M. Hydrolytic degradation of devices based on poly(DL-lactic acid) size-dependence. *Biomaterials* **1995**, *16*, 305–311. [[CrossRef](#)] [[PubMed](#)]
309. Lam, K.H.; Nieuwenhuis, P.; Molenaar, I.; Esselbrugge, H.; Feijen, J.; Dijkstra, P.J.; Schakenraad, J.M. Biodegradation of porous versus non-porous poly(L-lactic acid) films. *J. Mater. Sci. Mater. Med.* **1994**, *5*, 181–189. [[CrossRef](#)]
310. Lam, K.H.; Schakenraad, J.M.; Groen, H.; Esselbrugge, H.; Dijkstra, P.J.; Feijen, J.; Nieuwenhuis, P. The influence of surface morphology and wettability on the inflammatory response against poly(L-lactic acid): A semi-quantitative study with monoclonal antibodies. *J. Biomed. Mater. Res.* **1995**, *29*, 929–942. [[CrossRef](#)]
311. Cama, G.; Mogosanu, D.E.; Houben, A.; Dubruel, P. *Synthetic Biodegradable Medical Polyesters: Poly- σ -Caprolactone*; Elsevier Ltd.: Amsterdam, The Netherlands, 2017; ISBN 9780081003930.
312. Nelson, M.T.; Pattanaik, L.; Allen, M.; Gerbich, M.; Hux, K.; Allen, M.; Lannutti, J.J. Recrystallization improves the mechanical properties of sintered electrospun polycaprolactone. *J. Mech. Behav. Biomed. Mater.* **2014**, *30*, 150–158. [[CrossRef](#)]
313. Yeo, A.; Sju, E.; Rai, B.; Teoh, S.H. Customizing the degradation and load-bearing profile of 3D polycaprolactone-tricalcium phosphate scaffolds under enzymatic and hydrolytic conditions. *J. Biomed. Mater. Res. Part B Appl. Biomater.* **2008**, *87*, 562–569. [[CrossRef](#)]
314. Lam, C.X.F.; Savalani, M.M.; Teoh, S.H.; Hutmacher, D.W. Dynamics of in vitro polymer degradation of polycaprolactone-based scaffolds: Accelerated versus simulated physiological conditions. *Biomed. Mater.* **2008**, *3*, 034108. [[CrossRef](#)]
315. Meng, C.; Tang, D.; Liu, X.; Meng, J.; Wei, W.; Gong, R.H.; Li, J. Heterogeneous porous PLLA/PCL fibrous scaffold for bone tissue regeneration. *Int. J. Biol. Macromol.* **2023**, *235*, 123781. [[CrossRef](#)]

316. Ge, S.; Zhu, X.; Zhang, C.; Jia, D.; Shang, W.; Ding, C.; Yang, J. Nanosilica-Anchored Polycaprolactone/Chitosan Nanofibrous Bioscaffold to Boost Osteogenesis for Bone Tissue Engineering. *Molecules* **2022**, *27*, 8832. [[CrossRef](#)] [[PubMed](#)]
317. Yang, S.; Li, X.; Liu, P.; Zhang, M.; Wang, C.; Zhang, B. Multifunctional Chitosan/Polycaprolactone Nanofiber Scaffolds with Varied Dual-Drug Release for Wound-Healing Applications. *ACS Biomater. Sci. Eng.* **2020**, *6*, 4666–4676. [[CrossRef](#)] [[PubMed](#)]
318. Karakeçili, A.; Korpayev, S.; Orhan, K. Optimizing Chitosan/Collagen Type I/Nanoxyapatite Cross-linked Porous Scaffolds for Bone Tissue Engineering. *Appl. Biochem. Biotechnol.* **2022**, *194*, 3843–3859. [[CrossRef](#)] [[PubMed](#)]
319. Oh, S.H.; Lee, J.H. Hydrophilization of synthetic biodegradable polymer scaffolds for improved cell/tissue compatibility. *Biomed. Mater.* **2013**, *8*, 014101. [[CrossRef](#)]
320. Haglund, L.; Ahangar, P.; Rosenzweig, D.H. Advancements in 3D printed scaffolds to mimic matrix complexities for musculoskeletal repair. *Curr. Opin. Biomed. Eng.* **2019**, *10*, 142–148. [[CrossRef](#)]
321. Kim, J.W.; Shin, K.H.; Koh, Y.H.; Hah, M.J.; Moon, J.; Kim, H.E. Production of poly(ϵ -caprolactone)/hydroxyapatite composite scaffolds with a tailored macro/micro-porous structure, high mechanical properties, and excellent bioactivity. *Materials* **2017**, *10*, 1123. [[CrossRef](#)]
322. Vyas, C.; Zhang, J.; Øvrebø, Ø.; Huang, B.; Roberts, I.; Setty, M.; Allardyce, B.; Haugen, H.; Rajkhowa, R.; Bartolo, P. 3D printing of silk microparticle reinforced polycaprolactone scaffolds for tissue engineering applications. *Mater. Sci. Eng. C* **2021**, *118*, 111433. [[CrossRef](#)]
323. Vargas-Osorio, Z.; Ruther, F.; Chen, S.; Sengupta, S.; Liverani, L.; Michálek, M.; Galusek, D.; Boccaccini, A.R. Environmentally friendly fabrication of electrospun nanofibers made of polycaprolactone, chitosan and κ -carrageenan (PCL/CS/ κ -C). *Biomed. Mater.* **2022**, *17*, 045019. [[CrossRef](#)]
324. Asghari, F.; Rabiee Faradonbeh, D.; Malekshahi, Z.V.; Nekounam, H.; Ghaemi, B.; Yousefpoor, Y.; Ghanbari, H.; Faridi-Majidi, R. Hybrid PCL/chitosan-PEO nanofibrous scaffolds incorporated with A. euchroma extract for skin tissue engineering application. *Carbohydr. Polym.* **2022**, *278*, 118926. [[CrossRef](#)]
325. Amornkitbamrung, U.; In, Y.; Wang, Z.; Song, J.; Oh, S.H.; Hong, M.H.; Shin, H. C-axis-oriented platelets of crystalline hydroxyapatite in biomimetic intrafibrillar mineralization of polydopamine-functionalized collagen type I. *ACS Omega* **2022**, *7*, 4821–4831. [[CrossRef](#)]
326. Cheng, Z.; Teoh, S.H. Surface modification of ultra thin poly (ϵ -caprolactone) films using acrylic acid and collagen. *Biomaterials* **2004**, *25*, 1991–2001. [[CrossRef](#)] [[PubMed](#)]
327. Luo, Y.; Xing, J.; Lin, M. The Biocompatibility of the Scaffolds Reinforced by Fibers or Tubes for Tissue Repair. In *Tissue Repair. Reinforced Scaffolds*; Li, X., Ed.; Springer: Singapore, 2017; Volume 6, pp. 225–233, ISBN 9789811035531.
328. Jaidev, L.R.; Chatterjee, K. Surface functionalization of 3D printed polymer scaffolds to augment stem cell response. *Mater. Des.* **2019**, *161*, 44–54. [[CrossRef](#)]

Disclaimer/Publisher's Note: The statements, opinions and data contained in all publications are solely those of the individual author(s) and contributor(s) and not of MDPI and/or the editor(s). MDPI and/or the editor(s) disclaim responsibility for any injury to people or property resulting from any ideas, methods, instructions or products referred to in the content.